

2005

Impact of large scale substrate roughness on giant magnetoresistive thin films

Shannon M. Watson
College of William & Mary - Arts & Sciences

Follow this and additional works at: <https://scholarworks.wm.edu/etd>



Part of the [Condensed Matter Physics Commons](#)

Recommended Citation

Watson, Shannon M., "Impact of large scale substrate roughness on giant magnetoresistive thin films" (2005). *Dissertations, Theses, and Masters Projects*. Paper 1539623488.
<https://dx.doi.org/doi:10.21220/s2-12fg-tg10>

This Dissertation is brought to you for free and open access by the Theses, Dissertations, & Master Projects at W&M ScholarWorks. It has been accepted for inclusion in Dissertations, Theses, and Masters Projects by an authorized administrator of W&M ScholarWorks. For more information, please contact scholarworks@wm.edu.

IMPACT OF LARGE SCALE SUBSTRATE ROUGHNESS ON GIANT
MAGNETORESISTIVE THIN FILMS

A Dissertation

Presented to

The Faculty of the Department of Physics
The College of William and Mary in Virginia

In Partial Fulfillment

Of the Requirements for the Degree of

Doctor of Philosophy

by

Shannon M. Watson


2005

APPROVAL SHEET

This dissertation is submitted in partial fulfillment of

The requirements for the degree of

Doctor of Philosophy

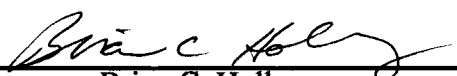


Shannon M. Watson

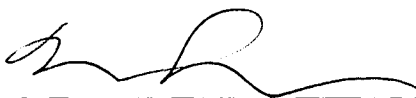
Approved, September 2005




Anne C. Reilly



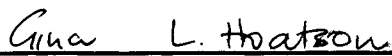
Brian C. Holloway



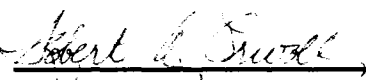
Marc Sher



William J. Kossler



Gina L. Hoatson



Robert A. Orwoll
Chemistry Department

DEDICATION

I could not have made it through my years of graduate study without the love and support of my family: My brother helped me keep my sense of humor; my mother helped me keep my sanity; my father consistently reminded me that I could overcome any obstacle, real or imagined; and my Uncle Robert and my first cousins looked after me and allowed me to be a kid on occasion. Additionally, my grandmothers reminded me of the importance of family and why we should cherish it. I am very grateful, too, for the long distance chats with my dear friend and fellow graduate student, Lisa Hilliard, who allowed me to talk about everything... and nothing.

TABLE OF CONTENTS

Acknowledgments	vii
List of Tables	viii
List of Figures	x
Abstract	xviii
Chapter 1: Introduction	2
1.1 Review of Literature	5
1.2 Outline of Thesis	8
1.3 References	11
Chapter 2: Magnetism and Giant Magnetoresistance	13
2.1 Theory of Magnetism	13
2.2 Theory of Giant Magnetoresistance	26
2.3 Magnetic Control and Coupling	37
2.4 References	44
Chapter 3: Roughness Effects on Magnetic Behavior and GMR	45
3.1 Magnetic Behavior Effects	46
3.2 Electronic Behavior Effects	48
3.3 References	52
Chapter 4: Film Fabrication	53
4.1 Sputtering	53
4.2 Magnetron Sputtering	55

4.3 Triode Sputtering	58
4.4 Boat Evaporation	59
4.5 Film Fabrication Conditions	60
4.6 References	64
Chapter 5: Characterization Techniques	65
5.1 Surface Techniques	65
5.2 Magnetic Instruments and Techniques	73
5.3 References	85
Chapter 6: GMR on Polymer Substrates	86
6.1 Polymeric Substrates	87
6.2 Roughness Studies	89
6.3 GMR Optimization on Polymerization Substrates	92
6.4 Conclusions	100
6.5 References	102
Chapter 7: Etched Substrate Study	103
7.1 PSV Study at William & Mary	104
7.2 PSV and EBSV Study at NIST	110
7.3 Conclusions	123
7.4 References	125
Chapter 8: Nanodot Controlled Roughness Study	126
8.1 Roughness from Nanodots	128
8.2 CIP and CPP Multilayers on Nanodot Patterns	130
8.3 CIP Results and Discussion	133

8.4 CPP Results and Discussion	135
8.5 Summary	140
8.6 References	142
Chapter 9: Carbon Nitride Based Thin Films	143
9.1 Preparation of Magnetic Thin Films	145
9.2 Results on a-CN _x	148
9.3 Results on FL-CN _x	153
9.4 Conclusions	157
9.5 References	159
Chapter 10: Summary	160
10.1 Summary	160
10.2 Future Work	162
10.3 References	164
Vita.....	165

ACKNOWLEDGEMENTS

The author thanks Professors Anne Reilly and Brian Holloway, under whose guidance this research was conducted, for their patient advising and constructive criticism. They have been a constant source of support and professionalism. I am honored to have had the opportunity to study under their tutelage.

The author is also indebted to Professor Marc Sher for his continued support and encouragement. The author also wishes to acknowledge Dr. Ronald Outlaw for providing access to his wealth of experience and knowledge on a variety of subjects.

The author thanks Dr. Reza Loloee, Dr. William Pratt, and Dr. Jack Bass at Michigan State University and Dr. William Egelhoff, Jr at the National Institute of Standards and Technology for allowing access to their deposition systems and providing insight into the experimental results.

LIST OF TABLES

Table	Page
6.1: Comparison of root-mean-square roughness, average roughness, and peak height for polymer and bare silicon oxide wafer substrates	91
6.2: A list of the GMR measured for the same PSV grown on various substrates	100
7.1: Table of data for average (σ_{rms}) roughness of films (measured by AFM), average peak-to-peak (λ) lengths, GMR, resistances, and coercivities for films deposited on substrates etched for different durations. (*) Clean AFM scans for this film were not obtained; large error due in part to streaks in scans.....	107
7.2: List of average roughness measurements for etched and unetched 4x12 mm glass substrates pre-deposition. An EBSV was grown on these substrates.....	113
7.3: Comparison of average root-mean-square (σ_{rms}) roughness of glass pre-deposition (measured by AFM) and average feature peak-to-peak length (λ) with GMR, film resistance and coercivity measurements of 4x12 mm PSV films.....	113
7.4: Comparison of root-mean-square (σ_{rms}) roughness (measured by AFM) and feature peak-to-peak length (λ) with resistivity measurements of 12x12 mm PSV films.....	115
7.5: Root-mean-square (σ_{ms}) roughness of films (measured by AFM) and $\Delta R/R$ for substrates etched for different durations for EBSV films.....	119
8.1: Calculated and average measured separations and sizes of nanodots deposited using polystyrene spheres. Data courtesy of Kevin Smith. All dimensions are nm. For two dot sizes, the sizes could not be resolved.....	129
8.2: Nanosphere size, P and AP resistivity and GMR percent of CIP data. No obvious direct correlation between nanosphere diameter and GMR or film resistivity. Data and analysis by Dimitar Vlassarev.....	133

8.3: EBSV films with and without Au nanodots. The coercivity, exchange field, coupling field, P and AP resistivity and GMR (%) vary without displaying any particular trend with nanodot diameter.....	137
8.4: Multilayer thin films, [Cu 50Å/Co 40Å], with and without Au nanodots. Resistances are listed for parallel and antiparallel states.....	140
9.1: AFM measured average roughness, root-mean-square roughness, and peak height for unannealed and annealed films.....	149
9.2: Comparison of surface and magnetic properties for films prior to and post-annealing. Both films were deposited at 450 °C with a substrate bias of -40V. CN1 was grown in 50-50% N ₂ /Ar. CN2 was grown in 100 N ₂	155
9.3: A comparison of roughness measurement for films deposited on four different substrates. Films on both fullerene-like CN _x substrates exhibit the largest roughness prior to annealing. Post-annealing, CN1 has the roughest surface while CN2 has the smoothest surface of all four films.....	157

LIST OF FIGURES

Figures	Page
2.1: Magnetism arises due to the orbital angular and spin momentums of electrons in atoms.....	14
2.2: An external magnetic field gives rise to paramagnetism resulting from the interaction between the applied field and the total angular momentum of electrons orbiting atoms.....	17
2.3: Spin polarized DOS of various metals. a) Fe has high density of d states available. b) Co has high density of available d states. c) Ni has low density of states available. d) Cu has no d states available at the Fermi level and no spin asymmetry. Majority and minority spin bands are indicated by arrows. Taken from Hartmann, "Magnetic Multilayers and Giant Magnetoresistance, p. 73.....	19
2.4: Domain formation to minimize magnetostatic energy of the material.....	22
2.5: Hysteresis curve of a single ferromagnetic thin film. H _c , the coercivity, is the external field required to return film magnetization to zero. Saturation magnetization, M _s , is the maximum magnetization obtained when all domains are aligned. Remanent magnetization, M _r , is the magnetization of the film when the external field is returned to zero after initial saturation of film. Boxes illustrate how domain formation and domain wall motion affect hysteresis.....	25
2.6: Domains align around defects so that the magnetostatic energy is minimized. This can lead to large coercivities for films with a high density of defects.....	26
2.7: a) A simplified diagram of the density-of-states for the s and d states for a nonferromagnetic material. b) A diagram of the density-of-states for the s and d states for a ferromagnetic material. The density of states in b) is also analogous to a nonferromagnetic material in a very high external magnetic field.....	28
2.8: Spin-dependent scattering in the CPP direction. Scattering occurs in the bulk and at the interfaces. a) Parallel alignment of F layers results in scattering of the antiparallel aligned spin. b) Antiparallel alignment of F layers results in scattering of both spin polarizations.....	29

2.9: Representative GMR curve for multilayer thin film. Peaks represent antiparallel alignment of F layers resulting in a resistance greater than the parallel alignment at saturation.....	30
2.10: Illustration of applied current direction for both current-in-plane (CIP) and current-perpendicular-to-the-plane (CPP) GMR.....	32
2.11: Representation of RKKY coupling. Exchange parameter, j , oscillates between antiferromagnetic and ferromagnetic coupling between the ferromagnetic layers as the interlayer thickness increases.....	38
2.12: Exchange bias coupling between AF/F bilayer. The F layer is pinned by the AF layer grown adjacent to it. A high field is required to flip the orientation of the pinned F layer.....	40
2.13: The exchange bias field produces a shift from zero in the hysteresis curve. This is a result of the pinning of the ferromagnetic layer by the antiferromagnetic layer. A high applied field is needed to realign the ferromagnetic moments away from the pinned axis. A low field is sufficient to realign the spins back on their preferred axis. The result is the shift from zero along the x-axis.....	41
2.14: Coupling at the interface occurs between magnetic poles of adjacent F layers. This is referred to as the “Orange Peel” Effect.....	43
3.1: Illustration of grains. Grain size and valleys between grains are an important type of roughness and influence the magnetic behavior of film. Each grain has crystalline order, indicated by the arrows (showing a preferential crystal axis).....	46
4.1: A schematic of the dc magnetron sputtering system located at W&M used to fabricate most films. Four dc magnetron guns are located ~6” from the substrate. Multilayer thin films are grown using computer-controlled shutters to expose each gun in succession to the substrates.....	56
4.2: a) Schematic of cathode source. The magnetic field lines localize electrons over the target surface. The drift is strongest where the magnetic field is parallel to the target surface. b) The drift velocity contains the electron density in an annular region.....	57
4.3: Hot cathode sputtering injects electrons into the plasma by thermionic emission increasing the ionization probability of the carrier gas.....	58

4.4: Top and side view of boat evaporator with Au charge. The boat evaporator is constructed of a refractory metal that is resistively heated to thermalize the charge material located within.....	60
4.5: The Cosine Emission Law describes the distribution of ejected atoms from a point source. The shape is dependent on energy and angle of incidence.....	60
4.6: Rotating mask for CPP structured thin films seen from substrate side. Courtesy of Michigan State. ⁵	63
4.7: Top view (left) of CPP thin film structure. Current flow is applied perpendicular through structure by attaching leads to Nb cross strips. Cross-sectional view (right) illustrates direction of current through film. Note: GMR only measured over area (A) over overlay. CIP-GMR can also be measured in this configuration. Courtesy of Michigan State.....	63
5.1: Illustration of AFM scanning film surface. A tip attached to a cantilever oscillating at a specific frequency moves across the surface. A photodiode detector records deflections of a reflected laser aligned with the back of the cantilever. Courtesy of Molecular Imaging.....	68
5.2: Schematic of SEM. The SEM provides high-resolution 3D images of sample morphology.....	73
5.3: Superconducting ring interrupted by weak link. Schematic is typical of an RF SQUID. A DC SQUID would have two weak links. The weak link represents a Josephson junction. Image taken from Gallop " <i>SQUIDS, the Josephson Effects, and Superconducting Electronics</i> ".....	75
5.4: Simple schematic of a SQUID magnetometer. The SQUID is sensitive to tiny magnetic signals and is used for hysteresis and magnetoresistance measurements.....	77
5.5: Schematic of vibrating sample magnetometer. The VSM is used to measure hysteresis of films. The sample oscillates between to electromagnetic coils inducing a voltage proportional to the sample magnetization.....	78
5.6: Schematic of MOKE experimental setup. A modulated photon beam is polarized and reflected off a thin film in an applied field. The magnetization rotates the incident beam and a detector measures the rotation due to the film magnetization.....	81

5.7: Illustration of four-point probe experimental setup. The film is situated between two electromagnetic coils and a field is applied. Current is applied through two contacts on the surface and voltage is measured through the other two contacts.....	82
6.1: A schematic diagram used to illustrate the measurement for the thickness uniformity (DOP) of the polymer over topography.....	87
6.2: Photograph of the test pattern used for planarization measurements.....	88
6.3: AFM scans of Nb 100Å on oxide substrate and polymer buffers show no significant change in feature size for films on the oxide compared to the polymers. Surface roughness measured from AFM scans was comparable for films on all three substrates. a) Oxide substrate b) Polymer 13 c) Polymer 53. AFM in Tapping Mode and scan size is 1 μm x 1 μm.....	90
6.4: Structure of PSV used for this study, with summary of purpose for each layer.....	93
6.5: GMR for PSV on polymer 13 for three different Cu thicknesses (dots). The Co and NiFe layers were each fixed at 40Å. Solid line is from Equation 6.2 in text, assuming a $\lambda \sim 32$ nm for Cu. For Cu thicknesses of 4 and 5 nm, theory and experiment do not differ significantly. For thinner Cu thicknesses, Eq 6.2 does not account for a substantial increase in ferromagnetic coupling. Strong ferromagnetic coupling prevents the film from achieving a well-defined AP state that is necessary to obtain large GMR values.....	94
6.6: GMR for PSV on polymer 13 (red, closed squares) and 53 (blue, closed circles) for different Co thicknesses. The Cu and NiFe layers were fixed at 4 nm and 4 nm respectively. The maximum GMR was obtained at a Co thickness of 4 nm for films on both polymer buffers. The decrease in GMR occurs as the increasing Co thickness results in increased ferromagnetic layer coupling. The coupling limits the films ability to achieve a well-defined AP state. Dotted lines are to guide the eye.....	96
6.7: Hysteresis curves for the optimization of a PSV on a polymer substrate. a) Increasing Co layer thickness b) Increasing NiFe thickness c) Increasing Cu thickness. For Co (a) and NiFe (b), the magnetization increases with increasing thickness. For the Cu layer (c), the thinnest layer is red and the thickest is black. Notice the two loops emerging for the thickest Cu layer.....	97

6.8: Optimized PSV chosen for MRAM project. This PSV provides adequate switching between parallel and antiparallel states, though the F layers are not completely de-coupled from each other.....	99
6.9: GMR response for a pseudo spin valve deposited on silicon oxide (closed circles) and polymer 53 (open squares). Left: Total switching behavior. Right: spin valve response.....	100
7.1: AFM scans showing film surface roughness. (a) 30s etch. Vertical scale is 50 nm. (b) 300s etch. Vertical scale is 200 nm. Lateral scale for both is 1 μm x 1 μm . Scans show an increase in roughness feature length and height with increasing etch time. Scan (a) has small granular shaped features while (b) has larger features with a sinusoidal shape. AFM was in tapping mode.....	106
7.2: MOKE intensity (top) and GMR curves for spin valves on an unetched glass substrate (0) and a substrate etched for 150 s (150). Notice the increase in GMR as well as the slight broadening of the curves.....	108
7.3: Giant magnetoresistance ($\Delta R/R$, red, open circles) and coercivity (blue, open squares) as a function of film σ_{rms} roughness. Initially, both $\Delta R/R$ and coercivity increase steeply for the first few data points followed by less steep increases in both with increasing roughness. Finally, $\Delta R/R$ decreases and the coercivity plateaus. The initial increase suggests a decrease in ferromagnetic coupling achieving a more defined AP state. The benefit to GMR is lost as the roughness becomes detrimental, probably due to intermixing at the F/N interfaces. Lines are a guide to the eye.....	109
7.4: AFM scans showing surface roughness for EBSV substrates. a) unetched. b) 150s etch. Vertical scale is 50 nm for both. Lateral scale for both is 1 μm x 1 μm . Scans show increase in surface roughness with etch time. Scan (a) shows virtually no surface features while (b) has a large number of granular features on the surface. AFM was in tapping mode.....	112
7.5: Comparison of hysteresis curves for two films; one with high GMR of 4.52% (left) and low GMR of 1.08% (right). The curve on the left has a slight plateau while the curve on the right has no apparent plateau, suggesting that the ferromagnetic layers are strongly coupled.....	115

7.6: Relationship between antiparallel and parallel resistances. The data is fit by a linear relationship with slope ~ 1 . The slope is ~ 1 suggesting that roughness is affecting the spin-independent scattering more strongly than the spin-dependent scattering.....	116
7.7: Relationship between $\Delta\rho/\rho$ and parallel state resistivity. $\Delta\rho/\rho$ shows a near inverse dependence with ρ_p . When the overall film resistivity increases, the GMR decreases. Lines are a guide to the eye.....	117
7.8: Magnetization hysteresis (top) and GMR curves (bottom) for spin valves on an unetched glass substrate (blue, circles) and a substrate etched for 150 s (red, circles). The hysteresis for the unetched glass is more square and shows better switching than the etched glass. Notice the smaller minor GMR loop for the film on the etched film as well as the rounded peaks and the broadening of the curves. The arrows on the top plot indicate the direction of the pinning axis relative to the applied field for each sample.....	118
7.9: Giant magnetoresistance ($\Delta R/R$, dark red, circles), ferromagnetic coupling (green, diamonds), and exchange bias field (blue, triangles) as a function of film σ_{rms} roughness. The GMR varies around 5.0% without significantly decreasing. This may be linked to the ratio of exchange bias field to coupling field which is much greater than 1. There appears to be a weak $1/H_{eb}$ dependence but no obvious direct correlation to roughness. Lines are a guide to the eye.....	120
7.10: Ratio of exchange bias field to coercivity (red, open circles) and GMR (blue, closed circles) as a function of σ_{rms} roughness. There is no obvious correlation between roughness and GMR. A significant increase in the ratio of H_{eb}/H_c does not result in a significant change in GMR though it does correspond to the lowest value. This could be due to the low coercivity (~ 0.9 Oe) suggesting significant coupling between the F layers. Lines are a guide to the eye.....	122
7.11: Hysteresis (top) and GMR (bottom) curves for EBSV film deposited on substrate etched for 240s. The low coercivity could be a result of significant intermixing of layers resulting in increased ferromagnetic coupling. However, the GMR is only 11% lower than the reference value.....	123
8.1: Cartoon illustrating the use of nanodots to produce roughness in the thin film multilayers.....	126
8.2: Left: SEM image of nanospheres spin-coated onto silicon. Right: Pattern of metal nanodots left behind after evaporation and removal of nanospheres. Images courtesy of Mingyao Zhu.....	128

8.3: SEM scans of nanodots. Left: Au deposited onto 190 diameter nanospheres. Right: Au deposited onto 320 diameter nanospheres. The degree of uniformity over the surface is inconsistent from film to film. Courtesy of Kevin Smith.....	130
8.4: Left: CIP-GMR (%) on nanodot patterns as dependent on parallel state resistivity. Fit shows the ρ_P^{-1} dependence expected if only spin-independent scattering were increasing. Right: Plot of Measured ρ_{AP} versus ρ_P , with a fit to a linear dependence. Data courtesy of Dimitar Vlassarev.....	134
8.5: AFM scans in Tapping Mode of SiO ₂ wafer spin-coated with 320 nm diameter polymer spheres. a) Scan size is 1 μm x 1 μm . b) Scan size is 10 μm x 10 μm . Long range order decreases above 1 μm	135
8.6: GMR curve of EBSV with no nanodots and with nanodots deposited on 99 diameter polyspheres. Outgoing and ingoing saturation loops do not overlap suggesting a low resistance state between 0° and 90°.....	136
8.7: Coercivity (red, closed circles) and exchange bias field (blue, closed squares) for CPP-EBSV as a function of nanosphere size used to produce the nanodots. “0” indicates no nanospheres. Lines are guide to eye.....	138
8.8: Left: GMR (%) for CPP-EBSV as a function of nanosphere size used to produce the nanodots. Line is guide to eye. Right: antiparallel state resistance (R_{AP}) versus parallel resistance (R_P). Line is a linear fit, with slope of 1.0.....	139
9.1: AFM scans in Tapping Mode, 2.5 μm x 2.5 μm a) AFM scan of unannealed a-CN _x /NiFe 30Å film. b) AFM scan of annealed a-CN _x /NiFe 30Å film. There are no changes in surface features.....	148
9.2: Comparison of Ta/NiFe annealed and unannealed films with a-CN _x /NiFe annealed and unannealed films. The unannealed films are represented by open circles, the annealed films by closed circles.....	150
9.3: A comparison of film magnetization with film thickness. Magnetization decreased with NiFe thickness for both annealed and unannealed films. Magnetization is negative for a Cu/NiFe 10Å and Ta/NiFe 10Å and a-CN _x /NiFe 20Å suggesting a diamagnetic film for these thicknesses. The line is a fit to $M = M_{\text{bulk}} * (t - t_{\text{dead}})$	151

9.4: TEM scan of a-CN _x /NiFe 100Å shows NiFe islands (dark spots) growing on the a-CN matrix. Electron diffraction analysis of the film showed no strong ordering peaks and suggests an amorphous structure.....	152
9.5: a) CN1 unannealed film. b) CN2 unannealed film. c) CN1 annealed film. d) CN2 annealed film. Co100 Å was deposited on CN buffers. AFM scan in Tapping Mode, 1µm x 1µm.....	154
9.6: Comparison of normalized hysteresis loops for prior to and post annealing. No significant change in saturation magnetization or coercivity is observed. Open circles represent CN1. Closed circles represent CN2.....	156

ABSTRACT

This dissertation presents an investigation on the effects of large scale roughness on the properties of giant magnetoresistive multilayers. The large scale roughness ($\sigma_{\text{rms}} > 5 \text{ nm}$) is introduced into giant magnetoresistive thin films through the substrate. Current-in-plane (CIP) and current-perpendicular-to-the-plane (CPP) thin films were deposited by dc magnetron and triode sputtering. All films were characterized for roughness, magnetic and electronic behavior.

Our research on both pseudo spin valves and exchange-biased spin valves shows that long length scale roughness does not have a significant detrimental effect on GMR thin films. For the CIP films, we find that a decrease in GMR correlates to an increase in minimum film resistivity. As the minimum resistivity increased, the maximum resistivity increased linearly with a slope ~ 1 . This suggests that the decrease in GMR may primarily be an effect of increased spin-independent scattering resulting from the increased film roughness. The CPP films showed a similar relationship between minimum and maximum resistance. Studying the effect of such large scale substrate roughness is important for applications in which GMR multilayers are deposited on non-standard substrates and buffer layers including flexible media.

IMPACT OF LARGE SCALE SUBSTRATE ROUGHNESS ON GIANT
MAGNETORESISTIVE THIN FILMS

Chapter 1 – Introduction

Magnetic multilayer thin films, which consist of multiple layers of ferromagnetic and non-magnetic materials, each on the order of 1 nm thick, are providing interesting opportunities to study the physics of magnetism and electron transport, as well as being useful for applications. The most well known discovery related to magnetic multilayer thin films is the property of giant magnetoresistance (GMR). GMR is the large change in resistance induced in multilayer thin films under the influence of an external magnetic field.¹⁻³ Researchers and private industries have explored its potential usage in magnetoelectronic devices and sensors, a field known as “spintronics”.⁴⁻⁷ Incorporation of GMR into computers began in 1997 with the first successful fully functioning chip produced by Honeywell, and in 1998, IBM introduced the first GMR hard drive read sensor. Further development have been pursued by other industries with unique applications in mind.^{8,9} Scientific interest and commercial applications led to studies of GMR on different structures¹⁰⁻¹² and with various magnetic and non-magnetic metals. As the technological interest continues to drive commercial development, researchers strive to reach a better understanding of the fundamental micromagnetic properties of magnetic multilayers.³

Fundamentally, in ferromagnetic materials, GMR arises because of differences in scattering rates, and hence resistivity, of electrons with up and down spins. The resistivity change induced in a magnetic multilayer depends on the details of the

magnetization changes in the ferromagnetic layers. The magnitude of GMR or resistivity change is a sensitive function of the morphology of the thin films, the conditions of the interfaces between ferromagnetic and non-magnetic materials, impurities present in thin films, etc. Interlayer exchange coupling between ferromagnetic (F) layers through a nonmagnetic (N) interlayer is another important player in the physics of GMR.¹³⁻¹⁵ In fact, GMR was discovered in antiferromagnetically (AF) coupled Fe/Cr superlattices by Baibich et al in 1988.¹⁶ Moreover, the interlayer exchange coupling oscillates between ferromagnetic and antiferromagnetic coupling as a function of the nonmagnetic layer thickness.¹⁷

At the Fermi level, spin anisotropy exists between the majority and minority spins within ferromagnetic metals. In other words, the scattering probability for up and down spin electrons differs in ferromagnetic metals. The most common F metals are the transition metals, such as Fe, Co, and Ni. While conductivity takes place in the s/p bands, relevant scattering occurs in the d bands.³ Ferromagnetic transition metals have occupied d bands for one or both spin-oriented density-of-states (DOS) at the Fermi energy (E_F), allowing for spin-dependent scattering. The number of states available for both spins, in part, determines the strength of electron scattering into these states for F metals and also the strength of its magnetic properties. Nonmagnetic metals have no such spin asymmetry in the d-bands at E_F . In ferromagnetic metals, it is the spin-dependence of scattering, which creates spin channeling, as electrons of one spin transmit more easily than the other spin state through the multilayer structure.

Generally, magnetic multilayer thin films are comprised of at least two ferromagnetic layers with an interspacing nonmagnetic layer, though structures with

more complexity may be used to increase the GMR. Typically, the ferromagnetic layers chosen for the multilayer film are different materials but can also be the same material with different thicknesses. In an idealized case, the ferromagnetic magnetizations can be aligned exactly parallel and antiparallel with each other. When the F layers are aligned antiparallel to each other, both spin up and spin down electrons experience significant scattering, leading to high resistance. When the magnetizations of the F layers are parallel with respect to each other, as would happen when a large external magnetic field is applied, only one spin state is strongly scattered, leading to a drop in resistance. It is this difference in resistance that is referred to as GMR.

GMR has been a heavily studied field since its discovery in 1988. Of particular interest has been the role of small-scale interfacial roughness in GMR. Such roughness can be introduced and controlled by altering the growth conditions. Very little work, however, has been done exploring the effect of large-scale roughness on GMR. Such large-scale roughness can be introduced through the substrate or underlying buffer layer, when materials other than the standard silicon wafer are used. The effects of novel substrates and buffer layers on GMR are the topic of this thesis work. This work is important because of the increased inclusion of novel materials, such as polymers and carbon thin films, in thin film technology. Industrial and scientific needs continue to push for solutions to old and new applications.^{4, 5, 9, 18, 19}

This dissertation shows, through a series of experiments, the effect of substrate roughness on single ferromagnetic thin films and GMR multilayer thin films. It is shown that the smoothness of carbon nitride (CN_x) and polymeric materials are comparable to traditional buffers, suggesting that they may be utilized in devices that require low

interface roughness. No degradation of GMR or other magnetic properties is observed in thin films deposited onto various polymer buffers, as compared to those on traditional buffers. On CN_x buffers, the degradation of magnetic properties was apparent on amorphous carbon nitride (a-CN_x) but not fullerene-like carbon nitride (FL-CN_x) buffers. On a larger scale, substrate roughness was not found to be so detrimental as to inhibit viable GMR or other magnetic properties of magnetic multilayer thin films. On the contrary, it was shown to be beneficial under certain conditions. In short, this thesis shows that large-scale substrate roughness plays an important role in the mechanisms of spin transport and can be beneficial or moderately detrimental to magnetic multilayer thin films. This scale of roughness does not necessarily hinder the development of spintronic devices on non-traditional buffers or buffers with large-scale ($\sigma_{\text{rms}} > 5 \text{ nm}$) roughness.

1.1 - Review of Literature

Baibich and Grunberg jointly discovered the magnetic field dependent resistance in antiferromagnetically coupled Fe/Cr interlayers in 1988, which Baibich coined “giant magnetoresistance”. It was recognized early on that the effect was due to spin-dependent scattering in the ferromagnetic layers and at the F/N interfaces. Accordingly, early models based on a Boltzmann transport equation were formulated to describe the effect. Such models considered spin-dependent and spin-independent scattering from sites in both the bulk of the layers and at the interfaces between the layers. Soon, researchers also realized that roughness in the film, particularly at the interface, could have a strong effect on GMR.

In their investigation of GMR in Fe/Cr multilayers, Binash, *et al.*²⁰ proposed that the increased resistivity in the anti-parallel alignment was a result of spin-flip

scattering.²⁰ Then, Barnas, *et al.* discovered large changes in resistance in ferromagnetically coupled layers.²¹ The antiparallel alignment was achieved by using Co layers of different thicknesses and therefore, different coercive fields. These discoveries fueled new interest in magneto- and spin-transport through multilayers. Parkin showed that magnetic multilayers deposited onto polymeric substrates exhibit GMR and other magnetic properties,²² opening the field to non-traditional substrates and buffers, such as polymers and carbon thin films.

It is important to understand how film roughness functions in relation to GMR and the mechanism by which roughness affects GMR. While some research has correlated growth conditions with GMR²³⁻²⁵, there remains less understanding of the mechanisms by which interfacial roughness effects GMR. Levy, *et al.* measured GMR in corrugated materials to study electron transport.²⁶ Several groups have shown that GMR ratios change when measuring materials deposited by the current-in-plane (CIP) and current-perpendicular-to-the-plane (CPP) methods.^{21, 26, 27} Their initial observations provide a link between giant magnetoresistance and interfacial roughness at layer boundaries but do not offer complete explanations.

Past studies have found that spin dependent scattering at the interface must be included in the theory of GMR.²⁸ Generally, an increase in interfacial roughness has been correlated with a decrease in GMR due to detrimental effects on the spin-dependent scattering.^{28, 29} However, previous researchers have studied the effect of roughness on magnetic thin films in the short mean free path limit, where the roughness is smaller than the electron mean free path in the material.^{30, 31} Cyrille found an increase in CPP-GMR with roughness attributed to an increase in spin-dependent scattering and an increase in

CIP-GMR due to enhanced current flow across the superlattice. Zambano, under a similar experiment found no change in CPP-GMR. More recent studies consider the long mean free path limit.³² In this regime, the roughness is comparable to the electron mean free path in the magnetic and nonmagnetic materials deposited. The wavelength of the roughness introduces a longer path length for electrons to travel thus increasing their scattering probability, which, in turn, increases the GMR of the multilayer. This thesis considers interfacial roughness, introduced through the substrate, on a long length scale and attempts to determine the overall effect on GMR and other magnetic properties. In doing so, we attempt to control the scale of roughness introduced through the substrate and model the interface roughness based on the measured substrate surface roughness.

There is no single model to predict GMR in magnetic multilayer thin films. Bruno and Chapert used a modified Ruderman-Kittel-Kasuya-Yosida (RKKY) model to predict interlayer coupling between two magnetic layers separated by a nonmagnetic layer by including the oscillatory effect dependent on interlayer thickness.¹⁷ This model assumes a smooth interface, and the effect is less dominant when the interface becomes rough. Barnas, *et al.* proposed a theory that models GMR using the Boltzmann equation with spin-dependent bulk and interfacial scattering.²¹ In the limit of long mean free path, the multilayers can be viewed as resistors in series (CPP) or parallel (CIP). The general Boltzmann equation can be tailored to model spin-polarized transport and interfacial roughness at long and short mean free path limits.³³ For CPP geometry, the Boltzmann equation reduces to the two-current series resistor (2CSR) model.³⁴ This model works best for structures where the spin diffusion length, l_{SF} , in the ferromagnetic and nonmagnetic layers is larger than the F and N layer thicknesses. It also assumes that

spin-flipping at the interfaces does not occur or is a weakly allowed approximation. For films where l_{SF} is smaller than the F and N layer thicknesses, a more complicated model, the Valet-Fert (VF), provides a more accurate description. The solutions for this model are not trivial and only reduce to a 2CSR-like model when l_{SF} is large. Modeling of CIP-MR is even more complicated because of the increased number of parameters and researchers are currently developing methods to solve these equations.³⁵ Despite this, there is still no all-encompassing model for GMR.

1.2 - Outline of Thesis

This dissertation discusses the effects of long-length scale roughness at the interfacial boundaries of giant magnetoresistive multilayer films with novel or non-traditional buffer materials. Chapter 1 introduces the purpose of this thesis and provides a review of the literature. Chapter 2 discusses the general theories of magnetism and GMR. Chapter 3 discusses the factors that can lead to thin film roughness in the bulk and at the interface and describes the effects interfacial roughness may have on magnetic thin films and GMR. Chapter 4 describes the deposition processes utilized to fabricate the magnetic thin films. Chapter 5 discusses the instruments used for characterization of the thin films and describes the theory behind their operation.

Chapter 6 presents results of single Nb layers and GMR multilayer thin films grown on polymer buffer layers. It is shown that for films deposited on polymer buffers the average root-mean-square (σ_{rms}) roughness is comparable to films deposited on silicon substrates. Further, GMR spin-valves are shown to be successfully deposited on polymer substrates with little degradation in GMR properties. We have conducted initial annealing experiments on the pseudo spin valves and have found no change in the GMR

after annealing for one-half hours at 150 °C. We have deposited GMR pseudo-spin valves, with GMR > 3%, on a polymer buffer layer and show that this is comparable to the same structure on silicon oxide.

Chapter 7 presents a controlled roughness study conducted on glass substrates etched with a hydrofluoric (HF) acid prior to deposition of GMR thin films. A series of pseudo-spin valves (PSV) and exchange bias spin valves (EBSV) (spin valves to be defined in experimental chapters) were deposited and the change in GMR and magnetic properties measured as a function of large-scale ($\sigma_{\text{rms}} > 5$ nm) substrate roughness. The PSVs were extremely sensitive to any parameter changes making a determination of the effect of substrate roughness difficult. For the EBSVs, it was found that the effects of growth conditions is somewhat overcome by the exchange bias field allowing for a better determination of effects only due to roughness. It is shown that roughness effects do not greatly influence the magnetic properties or GMR of thin films.

Chapter 8 presents a uniform roughness study conducted largely at Michigan State University (MSU) in a facility capable of depositing both current-in-plane (CIP) and current-perpendicular-to-the-plane (CPP) magnetic thin films. The roughness is produced by depositing a pattern of gold nanodots onto a silicon substrate and depositing the GMR films onto the nanodots. For the CIP films, it is shown that the decrease in GMR corresponds to an increase in minimum resistivity. The resistivity of the parallel electron spin state increases at the same rate as the antiparallel state resistivity, suggesting that the major effect of the roughness is on the spin-independent scattering rather than the spin-dependent scattering that is critical to GMR.

Chapter 9 presents a study of single-layer magnetic thin films deposited on amorphous carbon nitride ($a\text{-CN}_x$) and fullerene-like carbon nitride (FL-CN_x) to explore the possibility of incorporating these carbon-based materials into GMR multilayers. Films on both carbon based materials decrease in surface roughness with annealing although degradation of the magnetic properties in the films deposited on $a\text{-CN}_x$ also occurs, which may be linked to water permeation driven from the CN layer into the magnetic thin film. This did not occur for magnetic films on the FL-CN_x where the magnetic properties showed no obvious post-annealing change. Thus, it is possible to incorporate this type of carbon material into magnetic multilayers.

Finally, chapter 10 summarizes results for each chapter of the thesis and proposes future investigations into the effects of large-scale substrate roughness on magnetic multilayer thin films.

1.3 - References

- ¹ P. B. Allen, Solid State Communications **102**, 127 (1997).
- ² M. A. Howson, Contem. Phys. **35**, 347 (1994).
- ³ U. Hartmann, *Magnetic Multilayers and Giant Magnetoresistance: Fundamentals and Industrial Applications* (Springer Verlag, 2000).
- ⁴ J. L. Simonds, Physics Today **April**, 26 (1995).
- ⁵ G. A. Prinz, J. Magn. Magn. Mater. **200**, 57 (1999).
- ⁶ S. A. Wolf, D. D. Awschalom, R. A. Buhrman, et al., Science **294**, 1488 (2001).
- ⁷ J. De Boeck and G. Borghs, International Electron Devices Meeting, 215 (1999).
- ⁸ N. Spaldin, *Magnetic Materials: Fundamentals & Device Applications* (Cambridge University Press, New York, 2003).
- ⁹ M. Suzui, S. Tokito, and Y. Taga, Mater. Sci. Eng. B **B51**, 66 (1998).
- ¹⁰ A. Blondel, J. P. Meier, B. Doudin, et al., Appl. Phys. Lett. **65**, 3019 (1994).
- ¹¹ L. Piraux, J. M. George, J. F. Despres, et al., Appl. Phys. Lett. **65**, 2484 (1994).
- ¹² J. Velez and C. Yia-Chung, Phys. Rev. B **67**, 144425 (2003).
- ¹³ P. Grunberg, R. Schreiber, Y. Pang, et al., Phys. Rev. Lett. **57**, 2442 (1986).
- ¹⁴ H. T. Hardner, S. S. P. Parkin, M. B. Weissman, et al., J. Appl. Phys. **75**, 6531 (1994).
- ¹⁵ C. Carbone and S. F. Alvarado, Phys. Rev. B **36**, 2433 (1987).
- ¹⁶ M. N. Baibich, J. M. Broto, A. Fert, et al., Phys. Rev. Lett. **61**, 2472 (1988).
- ¹⁷ P. Bruno and C. Chappert, Phys. Rev. Lett. **67**, 1602 (1991).
- ¹⁸ J. M. Daughton, Thin Solid Films **216**, 162 (1992).

- 19 R. R. Katti and H. Kaakani, in *2000 IEEE Aerospace Conference. Proceedings*
(*Cat. No.00TH8484*), Big Sky, MT, USA, March 2000), Vol. 5, p. 371.
- 20 G. Binasch, P. Grunberg, F. Saurenbach, et al., *Phys. Rev. B* **39**, 4828 (1989).
- 21 J. Barnas, A. Fuss, R. E. Camley, et al., *Phys. Rev. B* **42**, 8110 (1990).
- 22 S. S. P. Parkin, *Appl. Phys. Lett.* **69**, 3092 (1996).
- 23 W. C. Chiang, W. P. Pratt, Jr., M. Herrold, et al., *Phys. Rev. B* **58**, 5602 (1998).
- 24 K. Kagawa, H. Kano, A. Okabe, et al., *J. Appl. Phys.* **75**, 6540 (1994).
- 25 A. Paul, T. Damm, D. E. Burgler, et al., *Appl. Phys. Lett.* **82**, 1905 (2003).
- 26 P. M. Levy, S. Zhang, T. Ono, et al., *Phys. Rev. B* **52**, 16049 (1995).
- 27 C. Vouille, A. Barthelemy, F. E. Mpondo, et al., *Phys. Rev. B* **60**, 6710 (1999).
- 28 T. C. Huang, J. P. Nozieres, V. S. Speriosu, et al., *Appl. Phys. Lett.* **62**, 1478
(1993).
- 29 B. Seongtae, J. H. Judy, P. J. Chen, et al., *Journal of Applied Physics* **91**, 8414
(2002).
- 30 A. Zambano, K. Eid, R. Loloee, et al., *J. Magn. Magn. Mater.* **253**, 51 (2002).
- 31 M. C. Cyrille, S. Kim, M. E. Gomez, et al., *Phys. Rev. B* **62**, 3361 (2000).
- 32 J. Alicea and S. Hershfield, *J. Appl. Phys.* **93**, 7930 (2003).
- 33 J. Alicea and S. Hershfield, *J. Magn. Magn. Mater.* **268**, 388 (2004).
- 34 T. Valet and A. Fert, *Phys. Rev. B* **48**, 7099 (1993).
- 35 B. Butler, Z. Xiaoguang, and D. Nicholson, Vol. 2004.

Chapter 2 — Magnetism and Giant Magnetoresistance

As this thesis discusses the effect of interfacial roughness on GMR thin films, this chapter describes some basics of the theory of magnetism and giant magnetoresistance in solids. This discussion includes a description of current-in-plane (CIP) and current-perpendicular-to-the-plane (CPP) GMR as well as a more detailed explanation of the differences between them and transport of electrons in both configurations. Since the magnetic state of the layers is critical for GMR, procedures used to control the magnetic state and the magnetic coupling are also described. Effects of roughness on magnetic behavior and spin-dependent and spin-independent scattering of electrons will be discussed in Chapter 3.

2.1 - Theory of Magnetism

Fundamentally, magnetism in materials is a quantum effect arising from the spin and orbital momentum of electrons in atoms. An electron's orbital angular momentum, \vec{L} , gives rise to a magnetic moment with an associated magnetic field. This can be described semiclassically as shown in Figure 2.1 below. The electron orbit produces a current, which in turn gives rise to a magnetic field. Consider the current produced from an electron, e , with a given velocity, v , orbiting an atom at a given radius, r :

$$I = -e \left(\frac{v}{2\pi r} \right), \quad A = \pi r^2 \quad (2.1)$$

This gives rise to a magnetic moment, μ :

$$\vec{\mu} = IA = -e \left(\frac{v}{2\pi r} \right) \pi r^2 = \frac{-evr}{2} \cdot \frac{m}{m} = \frac{-e(mvr)}{2m} = \frac{-e\vec{L}}{2m} \quad (2.2)$$

where A is the area of the orbit and the magnetic moment has units of emu, typically.

The electron spin angular momentum, \vec{S} , also has an associated magnetic moment. The interaction between the magnetic moment from the spin and the magnetic field from the orbital angular momentum is known as spin-orbit coupling and is in addition to electron orbital-orbital and spin-spin interactions.

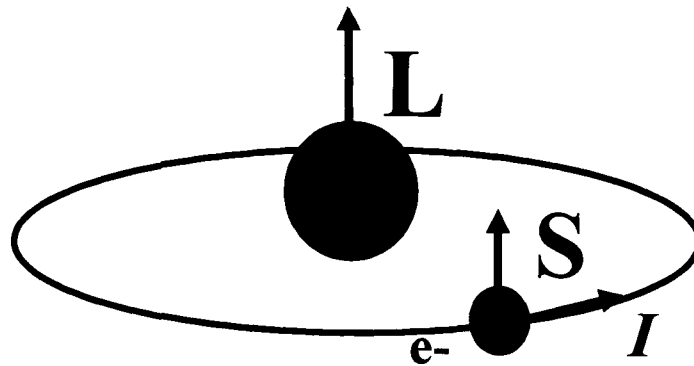


Figure 2.1: Magnetism arises due to the orbital angular and spin angular momentums of electrons in atoms.

The total magnetic moment including contributions of orbital angular momentum and spin is:

$$\vec{\mu} = \frac{-e}{2m_e} (\vec{L} + g_e \vec{S}) \quad (2.3)$$

where \vec{L} is the orbital angular momentum, \vec{S} is the spin angular momentum, and g_e is known as the Landé g-factor or the gyromagnetic ratio and describes the contribution of the magnetic moment from spin versus orbital motion. For electrons, g_e is ~ 2 . The g-factor associated with the orbital angular momentum in equation 2.3 is equal to 1 and is

not included in the equation. The nuclear charge determines the magnitude of the spin-orbit coupling by its dependence on the atomic number, Z . Because of this, for lighter atoms ($Z < 49$)¹, the spin-orbit coupling is negligible. As a result, spin-spin couplings dominate. For heavier atoms, the contribution of the spin-orbit coupling is much more significant and must be considered.

As stated above, the spin-orbit coupling interaction contributes weakly to the magnetic moment for lighter atoms. Subsequently, the total angular momentum can be calculated from the sum of the total orbital angular momentum, \vec{L} , and the total spin angular momentum, \vec{S} . These are the sums of the individual orbital angular momenta, l , and spin angular momenta, s . Using Hund's rules, the lowest energy states for the electrons are found by maximizing first the total spin angular momentum, \vec{S} , and then the total orbital angular momentum, \vec{L} . The total angular momentum, \vec{J} , is taken as the highest \vec{J} for shells more than half-full and the lowest \vec{J} for shells less than half-full. The atomic magnetic moment is dependent on the total angular momentum, \vec{J} , of the atom:

$$\vec{J} = \vec{L} + \vec{S} \quad (2.4)$$

This method does not account for a strong contribution from the spin-orbit coupling in heavier atoms. The total angular momentum must be calculated from the individual angular momenta, j , because \vec{S} and \vec{L} are not conserved but precess around \vec{J} which is conserved. Though \vec{L} and \vec{S} are not calculated explicitly, the interaction between the orbital and spin angular momenta is taken into account.

$$\vec{J} = \sum_i \vec{j}_i, \quad \vec{j}_i = \vec{l}_i + \vec{s}_i \quad (2.5)$$

In effect, Hund's rules state that electrons assume the states of maximum \vec{S} and \vec{L} , therefore minimizing contact with each other and reducing the repulsive Coulomb forces.

The magnetic response of atoms in a solid differs greatly from individual atomic moments. In a solid, individual atomic moments can align in an external magnetic field giving rise to paramagnetism or diamagnetism, or they may give rise to ferromagnetism, antiferromagnetism, or ferrimagnetism.

To describe diamagnetism and paramagnetism, we consider the basic Hamiltonian of atomic electrons in a magnetic field. The unperturbed Hamiltonian is:

$$H_0 = \frac{\vec{p}^2}{2m_e} + V_c(r) \quad (2.6)$$

where V_c is the atomic potential. In an applied field, the substitution $\vec{p} \rightarrow \vec{p} + e\vec{A}$ is made. The Hamiltonian becomes

$$H = \underbrace{\frac{\vec{p}^2}{2m_e} + V_c(r)}_{H_0} + \underbrace{\frac{e}{m_e} \vec{A} \cdot \vec{p}}_{H_1} + \underbrace{\frac{e^2}{2m_e} A^2}_{H_2} \quad (2.7)$$

The first order term, H_1 , gives rise to paramagnetism, while the second order term, H_2 , gives rise to the weaker diamagnetism affect. We consider only the first order in A which can be rewritten in a more familiar form:

$$H_1 = \frac{e}{m_e} \sum_i (\vec{H} \times \vec{r}_i \cdot \vec{p}_i) = \frac{e}{m_e} \sum_i (\vec{H} \cdot \vec{r}_i \times \vec{p}_i) = \frac{e}{m_e} (\vec{H} \cdot \vec{L}) \quad (2.8)$$

with $\vec{A} = \vec{H} \times \vec{r}$ and \vec{H} is the externally applied magnetic field. This represents the interaction of the applied field with the total orbital angular momentum for many electrons. To account for the effect of electron spin, additional terms are added to the

Hamiltonian for spin-orbit coupling and for the interaction of the applied field with the electron spin moment. This gives:

$$H_1 = \frac{e}{2m_e}(\vec{L} \cdot \vec{H}) - \frac{e}{2m_e^2 c^2 r} \frac{d\phi}{dr} \vec{L} \cdot \vec{S} + \frac{g_e e}{2m_e}(\vec{S} \cdot \vec{H}) \quad (2.9)$$

If we ignore the spin-orbit term in equation 2.9, we see that the Hamiltonian reduces to $H_1 = -\vec{\mu} \cdot \vec{H}$ with $\vec{\mu}$ defined in Equation 2.3. This term, describing paramagnetism, gives rise simply to an alignment of the atomic moments with an applied magnetic field.

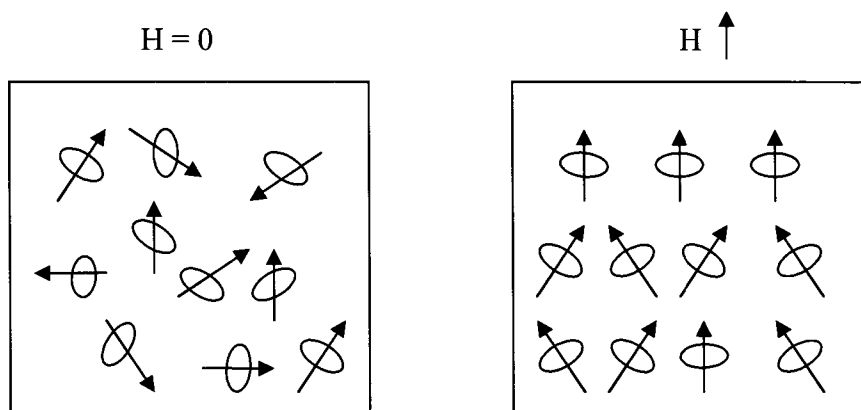


Figure 2.2: An external magnetic field gives rise to paramagnetism resulting from the interaction between the applied field and the total angular momentum of electrons orbiting atoms.

This effect, however, is much weaker than the ferromagnetic behavior which arises through another mechanism.

Ferromagnetism and Antiferromagnetism

A material with a net magnetic moment in the ground state (without an applied field) is described as ferromagnetic (F). The exchange interaction which gives rise to ferromagnetic ordering is similar to the exchange energy that dictates Hund's rules. Ferromagnetic alignment results from the interaction of neighboring atoms and their

individual spin states. We can describe ferromagnetism in solids in terms of only electron spins because the contributions due to orbital angular momentum tend to cancel out due to the crystalline structure (quenching).

The interaction Hamiltonian for a two-electron system can be written as:

$$\tilde{H}_{\text{int}} = -J\vec{s}_1 \cdot \vec{s}_2 = -J\left(\frac{\vec{s}^2}{2} + \frac{3\hbar^2}{4}\right) \quad (2.10)$$

The spin interaction parameter, J , (also known as the exchange) is calculated from the Coulomb term in the Hamiltonian and is positive for parallel alignment (ferromagnetism). The spins of the two electrons are represented by \vec{s}_1 and \vec{s}_2 . Thus, it is more energetically favorable for a ferromagnetic material to maximize its spin. In contrast, for an antiferromagnetic material, J is negative and it is favorable to have an antiparallel alignment of spins.

When considering ferromagnetism in metals, affects of bandstructure and itinerant electrons must be considered. Transferring electrons from lower bands to higher bands to minimize the Coulomb energy produces an increase in the band energy that opposes the parallel alignment of spins. As a result, this prevents simple metals from being ferromagnetic. Transition metals are able to overcome this opposition because of overlapping 3d and 4s bands. The 3d band has a higher density-of-states (DOS) and is narrower at the Fermi level than the 4s band. For the 4s band, the energy required to promote an electron to a vacant site is greater than the energy reduction produced from reversing the electron spin. The opposite is true for the 3d band especially when the Fermi level lies within the 3d shell. This generates more lower-energy electrons of the same spin and a corresponding spontaneous magnetic moment in the ground state.

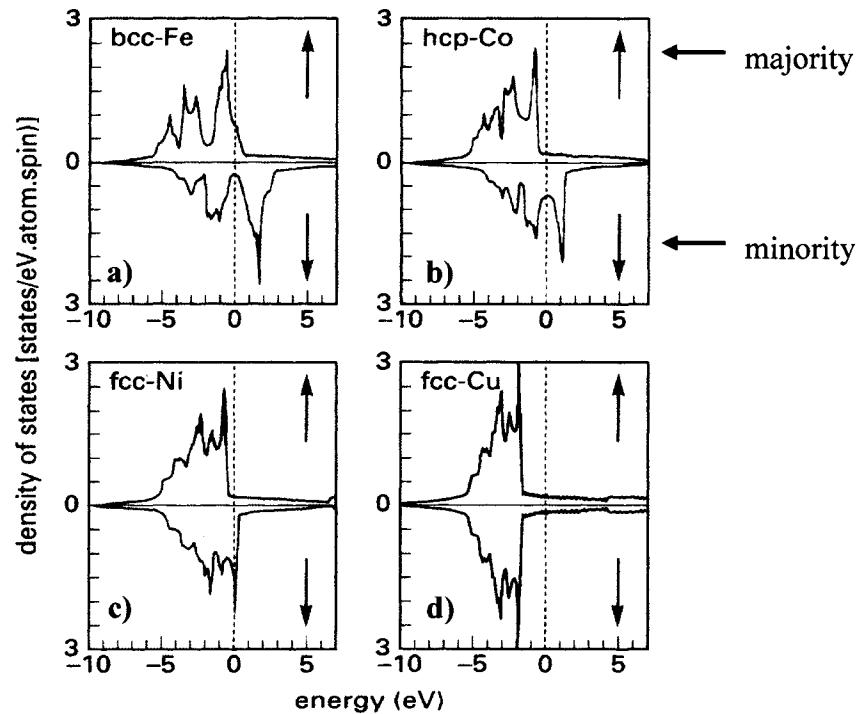


Figure 2.3: Spin polarized DOS of various metals. a) Fe has high density of d states available. b) Co has high density of available d states. c) Ni has low density of states available. d) Cu has no d states available at the Fermi level and no spin asymmetry. Majority and minority spin bands are indicated by arrows. Taken from Hartmann, "Magnetic Multilayers and Giant Magnetoresistance, p. 73.

Due to the exchange interaction, one spin state is favored over the other. Figure 2.3 displays the DOS for the spin orientations of several metals in the d-band. The ferromagnetic metals have states available above the Fermi energy for these bands. Nickel has only a small density of states available while cobalt has a higher density of d states above E_F . The difference between the DOS for up and down spins in the d-band accounts for the strength of the ferromagnetism in the transition states. In concurrence, Co is known to have a stronger ferromagnetism than Ni. In addition, copper, a nonmagnetic metal, has no states available above the Fermi energy and no difference in population between the two spin states, and thus is not ferromagnetic. In other words, metals, typically transition and rare earth metals, with a high density of open 3d or 4d

shells exhibit ferromagnetism. In addition, scattering processes occur from s/p to d states due to a high scattering probability into d states.² This model does not account for s/p/d hybridization but provides a foundation for understanding the mechanism behind spin-dependent scattering which is the source of GMR.

Ferromagnetic bulk materials have a macroscopic magnetization that may be large or small but exists without an applied external field, unlike paramagnetism where an applied field is needed to induce magnetism. The magnetization is defined as the summation of the individual electron moments,

$$\vec{M} = \sum_i \vec{\mu}_i \quad (2.11)$$

In summary, net magnetization occurs in ferromagnets because the energy for one spin state is lower than for the other and this state is either filled or nearly filled for ferromagnetic metals. This imbalance of the DOS between the two spins leads to a net spin and magnetization of ferromagnetic metals. If a high external field is applied, the localized magnetic moments will align with that field. When the field is removed, the moments realign such that the bulk material retains much of its previous magnetization.

In solids, the interaction of many electrons produces a bulk magnetization as electrons attempt to minimize their energy resulting in ferromagnetic ordering of the bulk. Thermal agitations can destroy this order especially when the interaction between moments is weak. The temperature at which the ferromagnetic interaction is overcome is known as the Curie Temperature; above this temperature no net ferromagnetic moment remains. Also, for antiferromagnets, the alignment disappears above the Néel temperature.

Domains and Hysteresis

In the absence of a magnetic field, the parallel alignment of all spins in a ferromagnetic material is actually energetically unfavorable, due to the production of a large magnetic field which in turn tends to demagnetize the material. Thus, ferromagnetic materials tend to divide up into domains of aligned magnetizations. The bulk magnetization of a ferromagnet is a function of properties that determine domain formation by which a ferromagnet minimizes its total magnetic energy.

First, the material attempts to reduce its magnetostatic energy, which is energy that allows the magnet to do work and is geometry dependent. Instead of forming one domain with a single moment, ferromagnetic materials form multiple domains each with its own moment. The progression of domain formation as the material continues to decrease its magnetostatic energy Figure 2.4 is shown. The domain pattern in figure 2.4c is favorable because it eliminates magnetic poles at the block surface.

However, this alone does not determine the domain size formation since minimizing the magnetostatic energy does not minimize the total magnetic energy of the material. Domain formation is a combination of various competing magnetoenergies: magnetostatic energy, magnetocrystalline energy, and the magnetostrictive energy. The result is the minimization of the total magnetic energy of the ferromagnetic material.

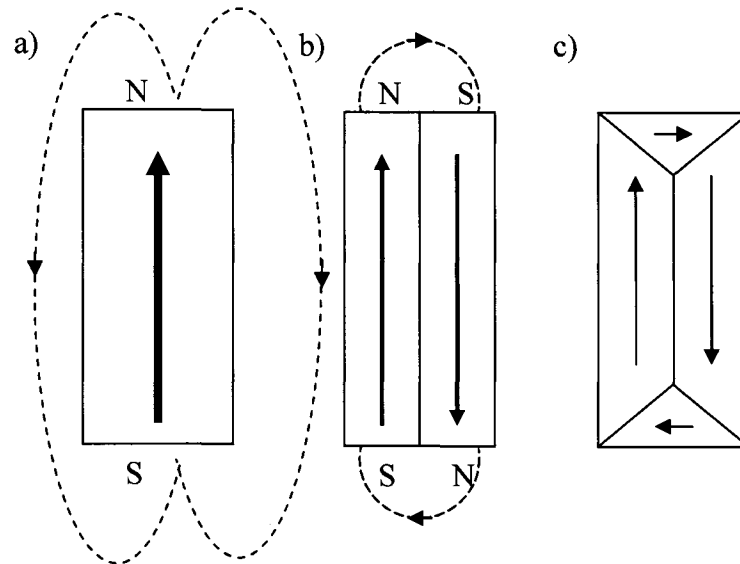


Figure 2.4: Domain formation to minimize magnetostatic energy of the material.

Crystalline ferromagnets have preferred crystallographic directions along which the spins tend to align, referred to as the ‘easy’ axes. The other axes are referred to as the ‘hard’ axes. The magnetocrystalline energy is the difference in energy between alignments along the ‘easy’ versus the ‘hard’ axes. Competition between the magnetocrystalline energy and the exchange energy determines the width of the domain walls. The magnetocrystalline energy favors sharp transitions between domains, which would require narrow domain walls. A sharp transition between one domain and the next produces high exchange energy, which would prefer a thicker domain wall allowing a gradual rotation of the spins from one orientation to the next or “twist”. This competition forces the domains to find a balance between the two. In magnetic thin films, spins rotate around an axis normal to the film surface with their poles at the domain walls. This is called a Néel Wall³ and reduces the magnetostatic energy of the material.

The magnetostrictive energy is determined by the geometry of the material. When magnetized, a ferromagnetic material will change in length as domains elongate. Materials exhibiting positive magnetostriction elongate along the direction of magnetization. Negative magnetostriction is displayed on a much smaller scale, on the order of tens of parts per million, but affect domain structure. Inevitably, an elastic strain ensues as competing domains try to elongate simultaneously adding a term to the total magnetic energy. Since the strain is dependent on the volume enclosed by individual domains, the solution should be to add more domains. However, this increases the magnetostatic and exchange energies. Subsequently, the material is forced reach a compromise between all competing energies to minimize the total magnetic energy.

Domain alignment influences the magnetizations of ferromagnetic materials. In particular, for the polycrystalline samples such as described in this thesis, it is the domain motion which determines the shape of the hysteresis loop. Hysteresis is an important property of ferromagnetic materials and is seen by measuring the magnetization (M) as a function of applied magnetic field (H). Domain motion describes the hysteresis process, as shown in Figure 2.5. In a demagnetized state, the domains are aligned so that the magnetization averages to zero. As a field is applied, the domains with spins nearest the direction of the external field rotate first. Then, the other domains begin to align with the field by domain wall motion. As the domain walls move, they encounter imperfections or defects in the material forcing the walls to align around them. These imperfections can be interstitial atoms, contaminant atoms, vacancies, or other lattice defects. In order to reduce the magnetostatic energy around defects, domains may form that are opposed to the applied field affecting the magnetic properties of the material.

Figure 2.5 is a representative hysteresis of a ferromagnetic single thin film. As a field is applied, the magnetization of the film approaches a maximum, referred to as the saturation magnetization, M_s . At this point, the domains have all aligned with the external field. The width of the curve is determined by the coercive field required to force the magnetization of the film back to zero. The coercivity, H_c , is measured at half the total width of the curve. This is influenced by the number of imperfections, dislocations, and impurities in the film as these hinder the easy alignment of the individual domains. The remanent magnetization, M_r , is a measure of the “memory” of the film. After an initial saturation, the film does not return to zero magnetization at zero-field. Instead, the film retains some of the magnetization as many of the domains remain aligned in an effort to decrease the exchange energy between domains, hence, the need to coerce the film to zero magnetization. The squareness of the hysteresis indicates whether the material is a soft or hard magnet as a hard magnetic material has a larger coercivity and a longer transition between saturations.

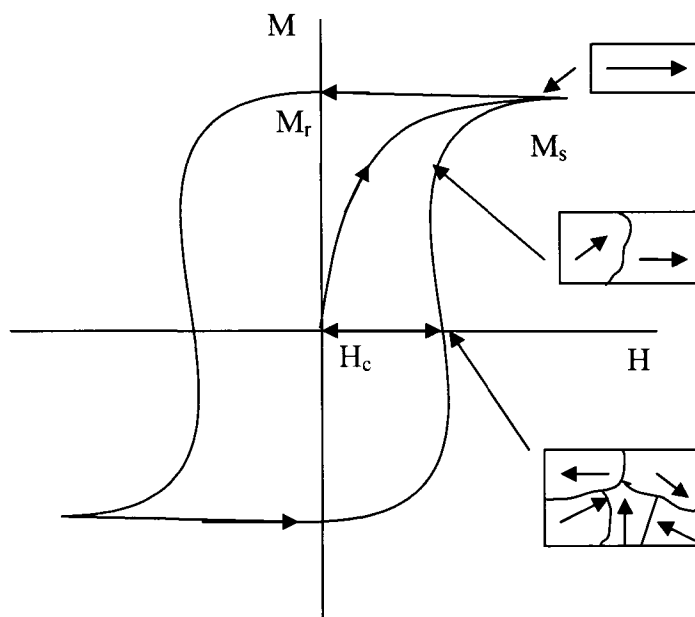


Figure 2.5: Hysteresis curve of a single ferromagnetic thin film. H_c , the coercivity, is the external field required to return film magnetization to zero. Saturation magnetization, M_s , is the maximum magnetization obtained when all domains are aligned. Remanent magnetization, M_r , is the magnetization of the film when the external field is returned to zero after initial saturation of film. Boxes illustrate how domain formation and domain wall motion affect hysteresis.

As mentioned, the hysteresis is very sensitive to the microstructure of the thin film. In particular, if there are a large amount of defects in the film, domains can form around these defects which are difficult to move. Figure 2.6 shows the evolution of domain formation around a defect. Films with large numbers of defects require stronger applied fields to force the rotation of spins around imperfections. The effect of these imperfections is evidenced, indirectly, in an increased coercivity in the hysteresis.

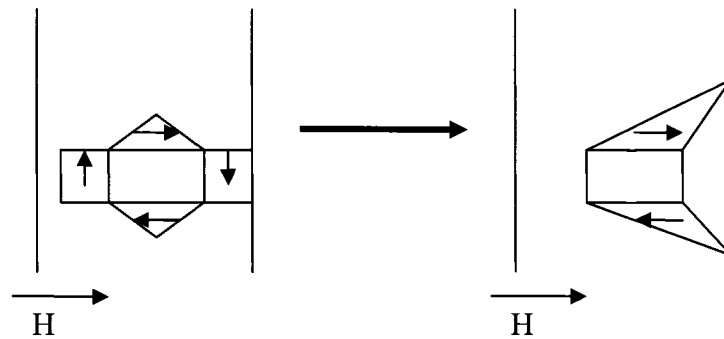


Figure 2.6: Domains align around defects so that the magnetostatic energy is minimized. This can lead to large coercivities for films with a high density of defects.

2.2 - Theory of Giant Magnetoresistance

Giant magnetoresistance is a phenomenon observed in multilayer thin films and dominates over the normal magnetoresistance seen in single layer films. GMR is described by the two-current model first proposed by N. Mott for electrical conductivity in metals. In this model, spin up and spin down electrons scatter by both spin-dependent and spin-independent processes. It is the spin-dependent scattering which gives rise to GMR. For the majority of scattering processes, electron spin quantum numbers are conserved and therefore, the spin-up and spin-down electrons do not mix over long distances. As a result, the total conductivity through the multilayer can be expressed as the sum of the spin up and spin down electron conductivities. The GMR effect is most significant when the layer-averaged electron mean-free path (CIP) or the spin diffusion length (CPP) for one spin orientation is very different than that for the other spin orientation. Electrical conductivity is carried out mainly by electrons in the s/p bands while scattering occurs from the s/p bands into open d bands.

In an applied field, electrons of one spin orientation are preferentially scattered by the ferromagnetic layers, while the nonmagnetic (N) layers show no spin-dependent scattering. This leads to a difference in resistance between the antiparallel (AP) and parallel (P) states of the multilayer, where AP and P refer to the alignment of the magnetizations between layers. The resistance change, due to the alignment of the ferromagnetic layers relative to each other, is a result of the unequal resistivities of the majority (spin up) and minority (spin down) electrons within the material. This inequality may be explained in terms of the DOS, as was discussed previously. The majority electrons always have less scattering and hence less resistivity than the minority due to less available states to scatter into at the Fermi level.

GMR arises due to spin-dependent scattering within the ferromagnetic layers as well as at the interfaces with non-ferromagnetic materials. As was discussed previously, the spin-dependent d bands are shifted and not evenly filled. Thus, as scattering occurs between the s/p and d bands, this scattering is spin-dependent for ferromagnetic materials but not for non-ferromagnetic materials, such as Cu. Figure 2.7 demonstrates the density-of-states available at the Fermi level. At the interfaces between layers, matching of the band structure determines the spin-dependent conduction. The difference in DOS for different metals produces a potential step at their interface. Transmission of electrons across the interface will be spin-dependent due to the spin-dependence of the ferromagnetic layer. Figure 2.3 illustrates this point. The DOS for Cu matches well with that for the Co majority spins resulting in good matching of the band structures. The transmission of majority electrons across the Co/Cu interface is high. In contrast, the significant difference in the DOS for Cu and the Co minority spins results in a large

mismatching of the band structure at the interface for those spins. The transmission of minority spins across the interface is low. Diffuse interfaces can have significant intermixing of atoms at the interface producing a random potential which is also strongly spin-dependent due to band matching. The result is an important contribution to the GMR effect from interfacial scattering in conjunction with bulk scattering.

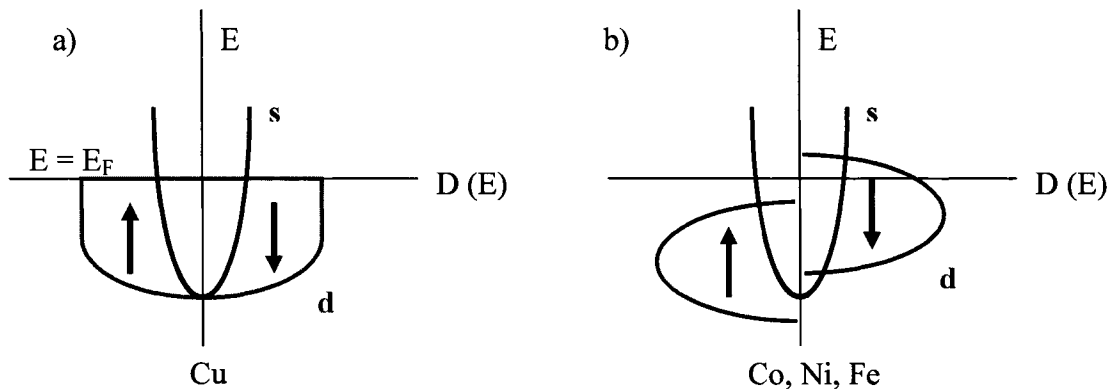


Figure 2.7: a) A simplified diagram of the density-of-states for the s and d states for a nonferromagnetic material. b) A diagram of the density-of-states for the s and d states for a ferromagnetic material. The density of states in b) is also analogous to a nonferromagnetic material in an extremely high external magnetic field.

Figure 2.8 shows the spin-dependent scattering that occurs in magnetic multilayer thin films. In the parallel state, the majority electrons conduct through the multilayer with minimal scattering and the total resistivity, which is determined by the highly conductive majority spins, is low. In the antiparallel state, spin up and spin down electrons are strongly scattered by one of the ferromagnetic layers and the total resistivity is high.

The GMR curve in Figure 2.9 is representative of a pseudo-spin valve (PSV) thin film, consisting of two different ferromagnetic layers separated by a nonferromagnetic layer. The curve peaks, corresponding to a maximum in resistivity, occur when the

ferromagnetic layers are aligned antiparallel. The peaks are centered on zero, which correlates to the crossing of the y-axis of the film's hysteresis loop. In addition, saturation for the GMR curve corresponds to saturation of the hysteresis loop. Here, the resistance is lowest for the film because of the parallel alignment of the ferromagnetic layers. The GMR of the film can be calculated from the change in resistance or resistivity between the two configurations as in equation 2.12:

$$GMR = \frac{R_{AP} - R_P}{R_P} \times 100 \quad (2.12)$$

where R_{AP} is the antiparallel resistance of the multilayer and R_P is the parallel resistance.

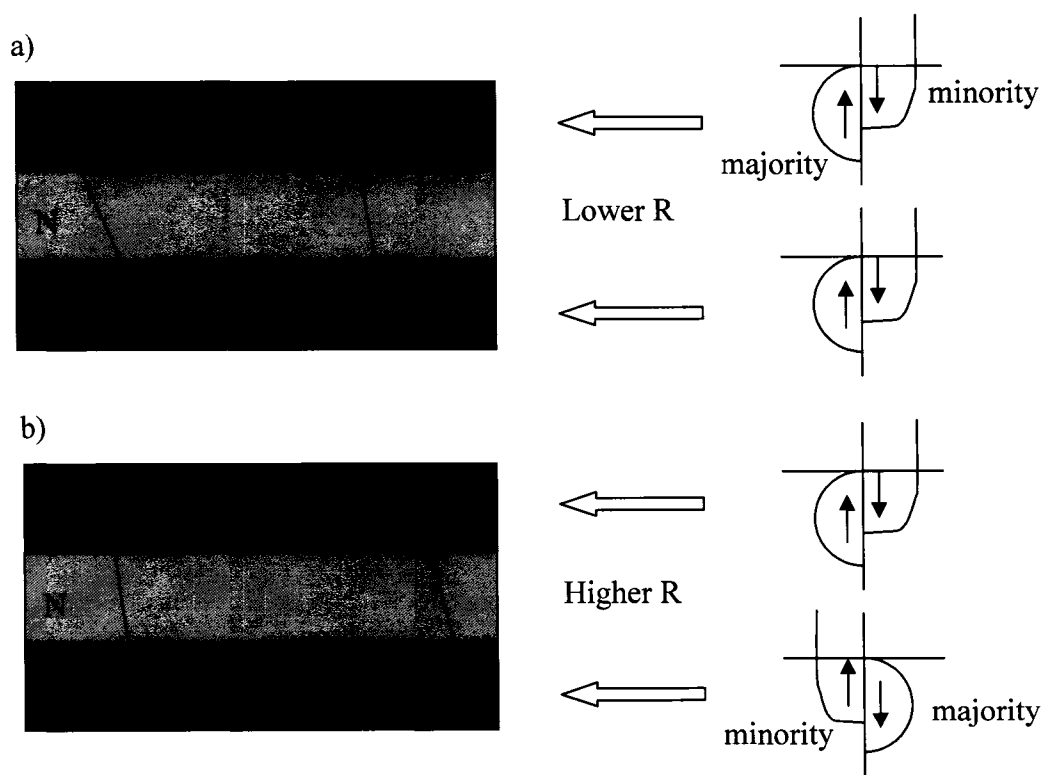


Figure 2.8: Spin-dependent scattering in the CPP direction. Scattering occurs in the bulk and at the interfaces. a) Parallel alignment of F (blue) layers results in scattering of the antiparallel aligned spin. b) Antiparallel alignment of F layers results in scattering of both spin polarizations.

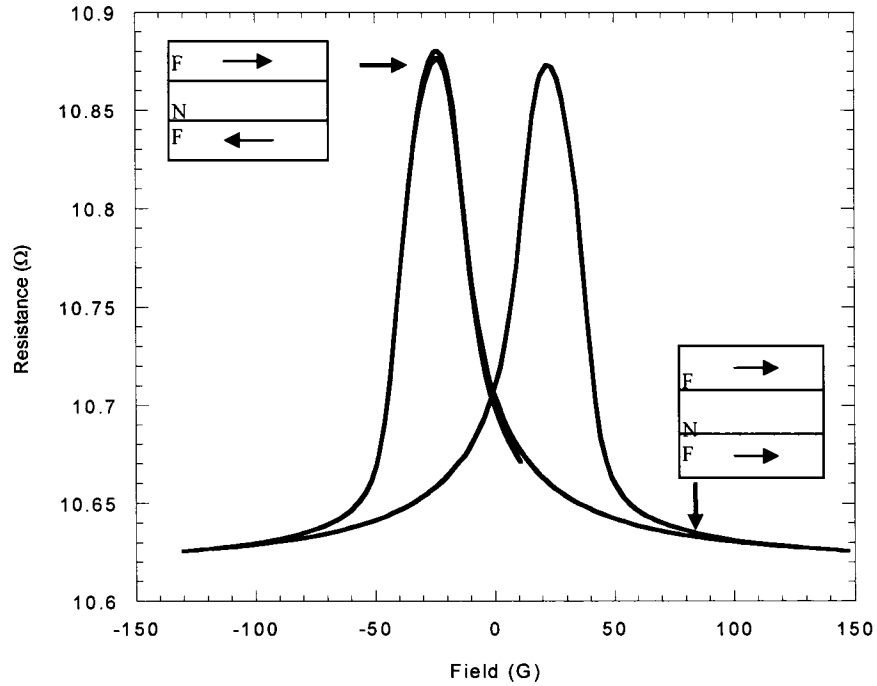


Figure 2.9: Representative GMR curve for multilayer thin film. Peaks represent antiparallel alignment of F layers resulting in a resistance greater than the parallel alignment at saturation.

A simple quantitative expression for CIP-GMR can be written for the case of a periodic F/N/F multilayer where the mean free path for electrons of both spins is much larger than the multilayer period. If R_{\uparrow} and R_{\downarrow} represent the separate resistances of up and down spins, then the resistance for parallel and anti-parallel alignment becomes:

$$R_P = \frac{1}{\left(\frac{1}{R_{\uparrow}} + \frac{1}{R_{\downarrow}}\right)}, \quad R_{AP} = \frac{R_{\uparrow} + R_{\downarrow}}{4} \quad (2.13)$$

and the GMR is

$$\frac{(R_{AP} - R_P)}{R_P} = \frac{(1 - \alpha)^2}{4\alpha} \quad (2.14)$$

with $\alpha = \frac{R_{\downarrow}}{R_{\uparrow}}$.

Thus, GMR increases as the asymmetry of resistivities (resistances) increases, or as spin-dependent scattering increases. This relationship between GMR and resistivity can be separated into three simple cases. In the case where both R_{\downarrow} and R_{\uparrow} increase at a similar rate, the change in α is negligible and the GMR remains unchanged or changes slightly. In the case of $\alpha \approx 1$, the asymmetry is negligible and the GMR approaches zero for the film. In the case where $R_{\uparrow} \gg R_{\downarrow}$, $\alpha \rightarrow 0$ and the GMR becomes very large as the asymmetry in resistances increases.

Current-in-Plane (CIP) GMR

This thesis studies two different types of GMR: current-in-plane and current-perpendicular-to-the-plane, as illustrated in Figure 2.10. The first, current-in-plane GMR is measured with the direction of current flow in the plane of the thin film and parallel to the applied magnetic field. Ohms' Law can be used to find GMR values by the four-point probe method to be described in Chapter 4. Typically, measured resistivities for thin films are on the order of 10Ω . Subsequently, there is no need for a special structure or equipment sensitive to small resistivities. CIP structures are easy to manufacture and their resistivities easy to measure. The disadvantage exists in the current sampling. If individual layers are too thick, the current may shunt through a less resistive layer, such as Cu, and not sample the entire multilayer.

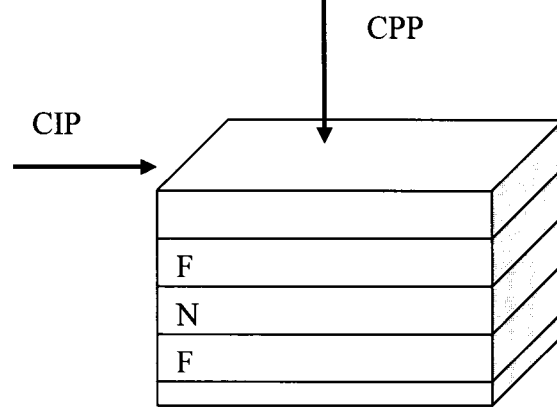


Figure 2.10: Illustration of applied current direction for both current-in-plane (CIP) and current-perpendicular-to-the-plane (CPP) GMR.

CIP-GMR theory is based on the semi-classical Boltzmann Transport equation (also called the Camley-Barnas theory). The semi-classical model assumes point-like particles and a polarized free electron gas in each layer of the film and spin-dependent scattering in the bulk, at the interfaces, and the boundaries. The semi-classical model includes contributions to the Fermi-Dirac electron distribution function, f , from electron drift, external magnetic fields, and electrons scattering:

$$\frac{\partial f}{\partial t} = \frac{\partial f}{\partial t} \Big|_{drift} + \frac{\partial f}{\partial t} \Big|_{field} + \frac{\partial f}{\partial t} \Big|_{scat} \quad (2.15)$$

This model applies quantum mechanical scattering probabilities and Fermi-Dirac statistics, hence the semi-classical label. The first term of equation 2.15 represents the change in the electron distribution with time in an applied field. After a sufficient amount of time, the distribution reaches a steady-state equilibrium and $\frac{\partial f}{\partial t} = 0$ by

definition. The right-hand side of equation 2.15 represents the electron drift and electron acceleration due to an applied field, respectively:

$$\left. \frac{\partial f}{\partial t} \right|_{drift} = -v \cdot \nabla_r f \quad (2.16)$$

$$\left. \frac{\partial f}{\partial t} \right|_{field} = -\frac{\partial f}{\partial k} \frac{\partial k}{\partial t} = eE \cdot \nabla_k f \quad (2.17)$$

where k is the electron momentum and E is the applied electric field. The scattering term is written as:

$$\left. \frac{\partial f}{\partial t} \right|_{scatt} = \sum_{k'} P_{kk'} [f(r', k', t) - f(r, k, t)] \quad (2.18)$$

where $P_{kk'}$ is the scattering probability between momentum states k and k' . This scattering includes both spin-dependent and spin-independent processes. In the relaxation time approximation, this term is simplified:

$$\left. \frac{\partial f}{\partial t} \right|_{scatt} = \frac{f - f_0}{\tau_C} \quad (2.19)$$

where f_0 is the initial Fermi distribution and τ_C is the relaxation time, or average time between scattering events. The Fermi-Dirac electron distribution is taken as the sum of the initial equilibrium distribution function when no field is applied and a deviation function:

$$\begin{aligned} f(\vec{v}, \vec{r}) &= f_0(\varepsilon) + g(\vec{v}, \vec{r}) \\ f_0(\varepsilon) &= \frac{1}{e^{(\varepsilon - \mu)/k_B T} + 1} \end{aligned} \quad (2.20)$$

where $g(\vec{v}, \vec{r})$ describes the deviation from equilibrium. Using these definitions and representing electrons by velocity v rather than momentum k , the Boltzmann transport equation can be written as:

$$\frac{\partial f}{\partial t} + \vec{v} \cdot \nabla_r f(\vec{v}, \vec{r}) - e\vec{E} \cdot \nabla_v f(\vec{v}, \vec{r}) = \frac{-(f - f_0)}{\tau_c} \quad (2.21)$$

The first left-hand term in steady-state equilibrium is zero. The second and third terms describe the change in space and velocity of the electrons, respectively. Substituting equation 2.20 for all terms to further simplify the Boltzmann transport equation, the distribution function is rewritten as

$$\vec{v} \cdot [\nabla_r f_0(\varepsilon) + \nabla_r g(\vec{v}, \vec{r})] - e\vec{E} \cdot [\nabla_v f_0(\varepsilon) + \nabla_v g(\vec{v}, \vec{r})] = \frac{-g(\vec{v}, \vec{r})}{\tau_c} \quad (2.22)$$

Looking at the left-hand side, first and second terms, respectively:

$$\begin{aligned} \vec{v} \cdot [\nabla_r f_0(\varepsilon) + \nabla_r g(\vec{v}, \vec{r})] &= \vec{v} \cdot \left[\frac{\partial f_0(\varepsilon)}{\partial r} + \frac{\partial g(\vec{v}, \vec{r})}{\partial r} \right] = \vec{v} \cdot \frac{\partial g(\vec{v}, \vec{r})}{\partial r} \\ -e\vec{E} \cdot [\nabla_v f_0(\varepsilon) + \nabla_v g(\vec{v}, \vec{r})] &= -e\vec{E} \cdot \nabla_v f_0(\varepsilon) = -e\vec{E} \cdot \vec{v} \frac{\partial f_0(\varepsilon)}{\partial \varepsilon} \end{aligned} \quad (2.23)$$

The first term simplifies because the gradient of the electron distribution with no applied field is zero. For the second term, only the lowest order term is retained since the applied field is assumed to be small. This gives a Boltzmann transport equation in the time relaxation approximation:

$$\vec{v} \cdot \frac{\partial g(\vec{v}, \vec{r})}{\partial r} - e\vec{E} \cdot \vec{v} \frac{\partial f_0(\varepsilon)}{\partial \varepsilon} = \frac{-g(\vec{v}, \vec{r})}{\tau_c} \quad (2.24)$$

where again v is the velocity of the electrons, E is the applied electric field, and τ_c is the relaxation time of electron scattering. For a two-spin conduction model, Equation 2.24 is rewritten to represent a two distribution functions are used representing each spin state.

The important parameter for CIP is τ_c which describes the time between scattering events. This determines the length scales for which approximate solutions can be found. Alternately, phenomenological or experimental models can be used to describe the dependence of GMR on the thickness of magnetic and nonmagnetic layers.

Current-Perpendicular-to-the-Plane (CPP) GMR

For CPP, the GMR is measured with the current flow perpendicular to the film plane which results in the entire area under the electrodes being sampled. Typically, the resistivity is lower than CIP-GMR measuring on the order of 10 n Ω and requires a measurement system sensitive to small resistivities. Additionally, the geometry of the film structure requires a specialized growth technique to achieve a CPP multilayer stack making the manufacture of CPP structures non-trivial. On the other hand, the GMR is typically larger than CIP-GMR. The theory of CPP-GMR is less complex than CIP-GMR because the entire layered structure is sampled and the Boltzmann equation reduces to a two-current series resistor (2CSR) model.⁴ The important length scale in this model is the spin diffusion length which is the average distance over which an electron travels before it flips spin. The 2CSR model assumes this spin-flip length is very long and thus assumes no mixing of the majority and minority spin currents. The model depends on spin anisotropy parameters β and γ , which are independent of both layer thickness and the number of layers. Instead, these parameters are material specific and dependent on the measured resistivities for spin up and spin down electrons:

$$\beta = \frac{\rho_F^\downarrow - \rho_F^\uparrow}{\rho_F^\downarrow + \rho_F^\uparrow}$$

$$\gamma = \frac{AR_{F/N}^\downarrow - AR_{F/N}^\uparrow}{AR_{F/N}^\downarrow + AR_{F/N}^\uparrow}$$
(2.25)

where ρ_{\uparrow} and ρ_{\downarrow} are the resistivities of spin up and spin down electrons in the multilayer, and $AR_{F/N}^{\uparrow}$ and $AR_{F/N}^{\downarrow}$ are the specific resistances of the spin up and spin down electrons at the ferromagnetic/nonmagnetic interface. For an EBSV structure, the 2CSR model adds the specific resistances (AR) of the bulk materials and the interfaces between layers as in a series resistor circuit⁵:

$$\begin{aligned} AR_{AP} &= AR_{S/F} + 2\rho_F^* t_F + \rho_N t_N + 2AR_{F/N}^* + AR_{AF/F} + \rho_{AF} t_{AF} + AR_{S/AF} \\ A\Delta R &= \frac{4(\beta\rho_F^* t_F + \gamma AR_{F/N}^*)^2}{AR_{AP}} \end{aligned} \quad (2.26)$$

where the subscripts AF and S represent the antiferromagnetic and superconducting layers and the other subscripts are defined above. The superscript * denotes the average value for up and down spins. For multilayers comprised of $[F/N]_N$, GMR can be calculated using:

$$\begin{aligned} AR_{AP} &= 2AR_{S/F} + N\rho_F^* t_F + 2N\rho_N t_N + 2NAR_{F/N}^* \\ A\Delta R &= \frac{N^2(\beta\rho_F^* t_F + 2\gamma AR_{F/N}^*)^2}{AR_{AP}} \end{aligned} \quad (2.27)$$

Again, the spin-dependent specific resistances of each interface as well as the bulk layers are added in series. GMR is calculated by dividing the change in specific resistance (ΔR) by the parallel specific resistance. Resistivities and specific resistances are determined from a series of films comprised of the specific ferromagnetic, nonmagnetic, and superconducting materials chosen. The parameters β and γ account for the unequal scattering of spin up and spin down electrons.

2.3 - Magnetic Control and Coupling

From the discussion of GMR theory, it can be seen that GMR depends primarily on two things: the amount of spin-dependent scattering and the ability to achieve true parallel and antiparallel alignments of the F layers. The parallel state is easily achieved by applying a large magnetic field, while the antiparallel state is more difficult to achieve. Typically, this state is produced experimentally through RKKY coupling or the use of pseudo-spin valve and exchange-biased spin valve structures.

Ruderman, Kittel, Kasuya, and Yosida (RKKY) coupling

RKKY coupling comes from an oscillatory interaction between the ferromagnetic layers dependent on the spacer layer thickness. It produces alternating ferromagnetic and antiferromagnetic alignment for increased nonmagnetic layer thickness of ~ 5 nm. By the selection of an appropriate thickness, the antiparallel alignment of alternating ferromagnetic layers is achieved in zero applied field. Figure 2.11 illustrates the periodic oscillation of the coupling as a function of interlayer thickness. RKKY coupling is used to produce the AP state in many-period multilayers. The Hamiltonian for RKKY coupling is expressed as

$$\mathbf{H}_{RKKY} = \sum_{ij} j_{ij}^{RKKY} \vec{S}_i \cdot \vec{S}_j \quad (2.28)$$

$$j_{ij}^{RKKY}(\vec{R}_{ij}) = 9\pi \left(\frac{j^2}{\varepsilon_F} \right) F(2k_F |\vec{R}_i - \vec{R}_j|) \quad (2.29)$$

where k_F is the radius of the conduction electron Fermi surface, R_i and R_j are the lattice positions for the point moments, ε_F is the Fermi energy, and

$$F(x) = \frac{x \cos x - \sin x}{x^4} \quad (2.30)$$

is the Fourier transform.

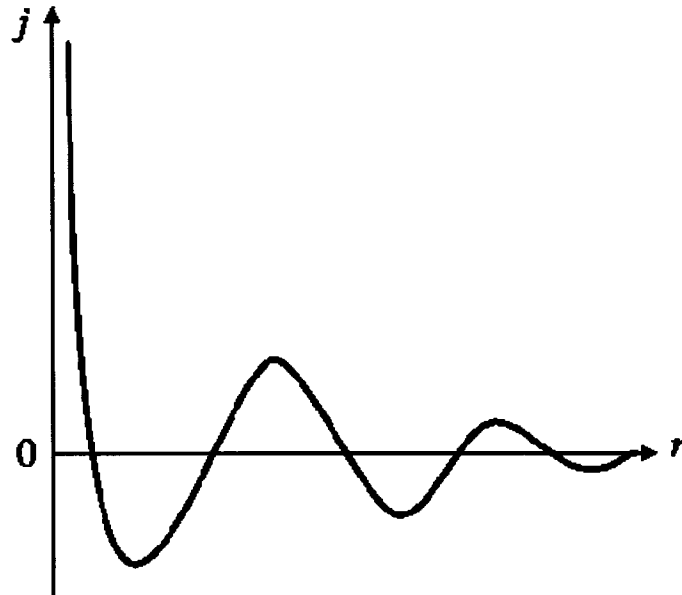


Figure 2.11: Representation of RKKY coupling. Exchange parameter, j , oscillates between antiferromagnetic and ferromagnetic coupling between the ferromagnetic layers as the interlayer thickness increases.

The coupling occurs through an indirect exchange between the moments of conduction electrons that propagates through the interlayer separating the ferromagnetic layers. As the interlayer thickness becomes large, RKKY coupling decreases to zero. The interaction dominates in films with small interfacial roughness but decreases with increasing roughness.

The coupling field is expressed as a function of the exchange energy and has a strong dependence on temperature⁶:

$$H_{EX} = \frac{E_{EX}}{\mu_0 M_{sat}^F t_F} \quad (2.31)$$

$$E_{EX} = \frac{E_0}{(k_0 t_s)^2} \sin\left(\frac{2\pi t_s}{\Lambda} + \psi\right) \frac{T/T_0}{\sinh(T/T_0)} \quad (2.32)$$

$$T_0 = \frac{\hbar v_F}{2\pi\kappa_B t_s} \quad (2.33)$$

where E_0 is the coupling energy, k_0 is a wave number, M_{sat} is the saturation magnetization, t is layer thickness, λ is the wavelength of the oscillating coupling pattern, and ψ is a phase shift. T_0 gives the characteristic temperature dependence on the Fermi velocity of electrons in the spacer layer and the spacer layer thickness. The RKKY coupling is dependent on the layer thicknesses of the nonmagnetic spacer interlayer and the free ferromagnetic layer.

Pseudo-Spin Valve

The second method involves the use of a pseudo-spin valve to achieve an AP state. The simplest spin valve has a F/N/F structure and can be multilayered with N numbers of bilayers, $[F/N]_N$. Typically, two different ferromagnetic materials having different coercivities are used to achieve the AP state. At high applied magnetic fields, both layers are saturated and are aligned parallel to the field. Due to the difference in coercivities, at low fields, one F layer begins to realign in the field sooner than the other layer. At a low enough field, the layers are aligned antiparallel. However, a completely AP state is hard to achieve experimentally because of magnetic coupling between the F layers. The dominant coupling is referred to as “orange peel” coupling and will be discussed later in the chapter. This difficulty led us to the use of exchange-biased spin valves.

Exchange-Biased Spin Valves

The third primary method used to produce an AP state is exchange biasing. A bilayer comprised of an AF/F layers displays an interaction known as exchange bias coupling. The spins along the AF/F interface align with the top moment of the

antiferromagnetic layer, referred to as the exchange interaction of the spins between the two layers. This causes the next level of spins to align in the same direction as those nearest the interface. This alignment propagates through the ferromagnetic layer until all the moments are aligned along the preferred direction. A large external field is needed to realign the spins of the ferromagnetic layer off this preferred axis or the “pinned” axis. Figure 2.12 illustrates the pinning of the ferromagnetic layer due to the exchange biasing of the antiferromagnetic layer. The pinning direction is usually set by heating and cooling the bilayer in an applied magnetic field. The exchange bias interaction leads to an effective magnetic field, H_{eb} , which was found to be inversely proportional to the pinned ferromagnetic layer thickness⁷, t_F^p :

$$H_{EB} = \frac{E_{EB}}{\mu_0 M_{sat}^p t_F^p} \quad (2.34)$$

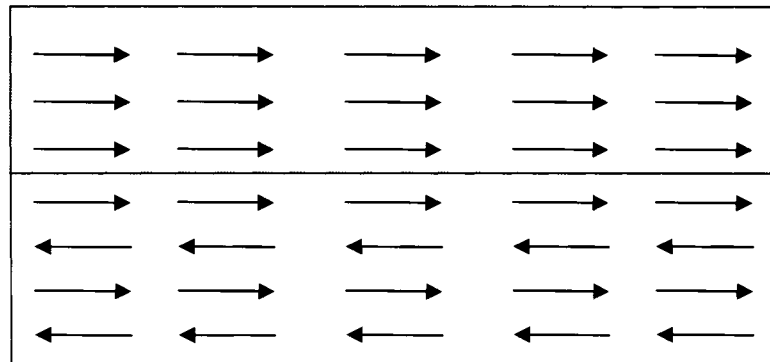


Figure 2.12: Exchange bias coupling between AF/F bilayer. The F layer is pinned by the AF layer grown on adjacent to it. A high field is required to flip the orientation of the pinned F layer.

This exchange bias field produces a shift in the magnetic hysteresis curve, as shown in Figure 2.13.

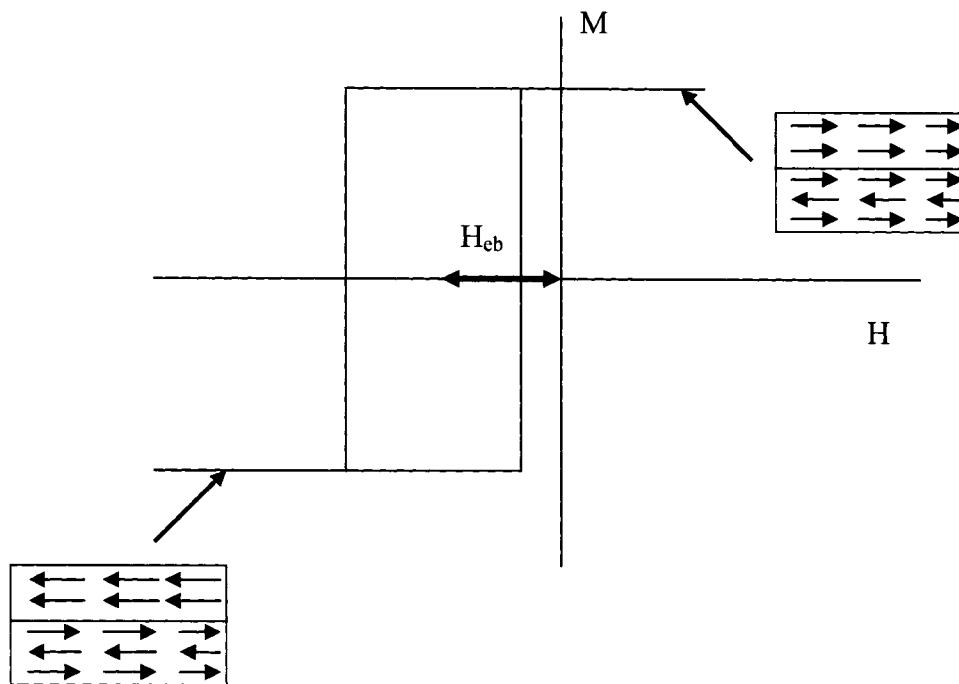


Figure 2.13: The exchange bias field produces a shift from zero in the hysteresis curve. This is a result of the pinning of the ferromagnetic layer by the antiferromagnetic layer. A high applied field is needed to realign the ferromagnetic moments away from the pinned axis. A low field is sufficient to realign the spins back on their preferred axis. The result is the shift from zero along the x-axis.

Exchange biasing can be used in GMR multilayers to provide better independent switching of the ferromagnetic layers and a definite antiparallel state. The structure usually consists of a F/N/F/AF multilayer, known as an EBSV. The antiferromagnetic layer pins one ferromagnetic layer while the other layer, referred to as the “free” layer, is allowed to rotate freely at low external fields. This means ideally that the free layer can be rotated into an antiparallel alignment with the pinned layer. Consequently, GMR values for EBSV are typically larger than those for unbiased multilayers.

Neél or “Orange Peel” Coupling

Neél or orange peel coupling⁸ is another type of coupling in magnetic multilayers which arises due to roughness in the films, particularly at the interfaces. The strength of

the scattering throughout the multilayer, in part, is determined by the interaction between the ferromagnetic layers. The orange peel effect arises due to the free magnetic poles produced at the interfaces as shown in Figure 2.14. “Orange peel” refers to the geometry of the interface. The coupling field is a function of the coupling parameter, J_{OP} :

$$J_{OP} = \frac{\pi^2 h^2}{L\sqrt{2}} \mu_0 M_{sat}^f M_{sat}^p e^{-2\pi\sqrt{2}/L} \quad (2.35)$$

with the coupling field defined as:

$$H_{OP} = \frac{J_{OP}}{\mu_0 M_{sat}^f t_F^f} \quad (2.36)$$

where M_{sat}^f and M_{sat}^p are the saturation magnetizations of the free and pinned layers, L is the peak-to-peak wavelength, t_s is the nonmagnetic interlayer thickness, t_F^f is the free ferromagnetic layer thickness and h is the peak to peak amplitude or waviness. These parameters determine the strength of the coupling between poles of adjacent ferromagnetic layers and consequently, the ability of a low applied field to align the magnetization of one ferromagnetic layer without significantly affecting the other simultaneously. From equation 2.35, it is evident that the coupling may increase or decrease with increasing peak to peak wavelength, although it always increases with increasing roughness amplitude h .

In the case of pseudo-spin valves (PSV), F/N/F, orange peel coupling can be significant. It is difficult to reverse the moments of a ferromagnetic layer completely independently from adjacent ferromagnetic layers. Even a weak coupling field produces some simultaneous realignment of moments between adjacent layers.

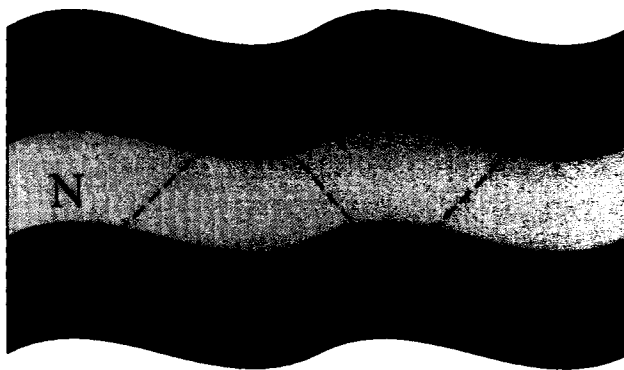


Figure 2.14: Coupling at the interface occurs between magnetic poles of adjacent F layers. This is referred to as the “Orange Peel” Effect.

In addition, it should be mentioned that direct coupling of ferromagnetic layers can occur if pinholes form in the nonmagnetic layer, forming a direct material bridge between the ferromagnetic layers. This is known as pinhole coupling and can occur for highly disordered films.

2.4 References

- ¹ P. Mohn, *Magnetism in the Solid State: An Introduction* (Springer, New York, 2003).
- ² U. Hartmann, *Magnetic Multilayers and Giant Magnetoresistance: Fundamentals and Industrial Applications* (Springer Verlag, 2000).
- ³ N. Spaldin, *Magnetic Materials: Fundamentals & Device Applications* (Cambridge University Press, New York, 2003).
- ⁴ J. Bass, W. P. Pratt, Jr., and P. A. Schroeder, Comments on Condensed Matter Physics **18**, 223 (1998).

Chapter 3 — Roughness Effects on Magnetic Behavior and GMR

As this thesis discusses the effect of interfacial roughness on GMR thin films, this chapter provides an overview of the effects of roughness on the magnetic and the electronic behavior of giant magnetoresistive thin films. Most previous experiments have varied interfacial roughness by changing film growth parameters: electron and ion energies, substrate temperature, deposition pressure, substrate bias, etc.¹⁻³ Instead of varying growth conditions, this discussion addresses interfacial roughness as applied through the substrate and describes effects on magnetic thin films as a function of roughness length scale. This is actually a complex problem as the effects may be interrelated. For example, roughness may affect coercivity and scattering, which both influence GMR. Changes in GMR may not be solely due to a change in coercivity but the underlying effect.

The films discussed in this thesis are polycrystalline in structure. Polycrystalline films consist of multiple grains, each with crystalline orientation. This produces boundaries between grains that consist of valleys of various widths and depth. Consequently, grains, grain boundaries, and their effect on magnetization and electron scattering are of great importance when discussing the behavior of GMR thin films. Substrate roughness effects can cause size variations in grains, increase intermixing at interfaces between layers, and reduce the sharpness of boundaries between grains.

Interfaces may be more sinusoidal or “wavy” which has implications for both the magnetic and electronic behaviors of thin films. The effect on PSV, EBSV, and multilayer spin valves varies. For simplicity, this discussion is categorized into magnetic and electronic effects due to interfacial roughness, though both may be affected simultaneously.

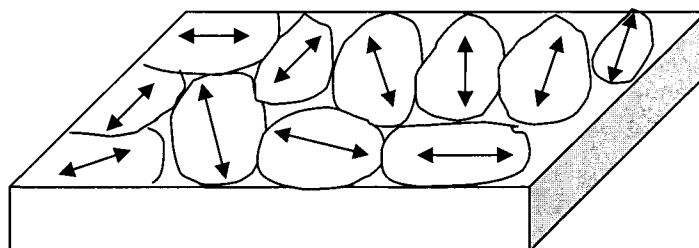


Figure 3.1: Illustration of grains. Grain size and valleys between grains are an important type of roughness and influence the magnetic behavior of film. Each grain has crystalline order, indicated by the arrows (showing a preferential crystal axis).

3.1 - Magnetic Behavior Effects

Effects on magnetic behavior are manifested in several ways. As mentioned above, polycrystalline films are comprised of grains, which contribute to roughness. In fact, the magnetostatic coupling between poles, which is geometry dependent, is produced by the transitions between grains or grain “valleys”.⁴ Increases in valley depth or decreases in individual grain diameters can increase the magnetostatic coupling strength as the dipolar poles are brought into closer contact. The result for PSV and multilayer spin valves is an increase in Néel coupling within the PSV, which is undesirable when attempting to achieve an AP state and reduces the thin film GMR.

For EBSV, there are separate mechanisms that can combine to weaken the AP state. When the coupling strength is stronger than the coercivity, the free layer can become strongly coupled with the pinned layer and the rotation of moments may be explained as a local effect occurring at grain valleys rather than domain wall motion.⁴ The free layer becomes effectively pinned as individual moments rotate coherently.⁴ Another mechanism occurs as roughness at the AF/F interface increases causing the AF layer to break into domains, greatly reducing the pinning strength of the AF layer.⁵ Also, roughness may produce pinholes that form a direct bridge between ferromagnetic layers through the interlayer, observed in PSV, EBSV, and multilayer SV.⁶ Pinhole coupling is an added detriment towards achieving an antiparallel state.

Changes in coercivity and magnetization of the individual ferromagnetic layers are also observed with increasing roughness. As discussed in chapter 2, coercivity is affected by the number of defects, such as dislocations and imperfections, present in a film.⁷ Roughness applies added strain to the crystalline structure as domains attempt to align around the defects which, in this case, are largely a result of grain growth.⁶ Typically, small grains have single domains but as grain size increases, multiple domains may form within a single large grain.⁸ An increase in coercivity could be explained by domain wall motion within the grains that determines the hysteresis shape.⁹ Growth of small grain clusters may also increase the coercivity through a reduction in the strength of the magnetic exchange coupling.¹⁰

Another consequence of increasing roughness is the decrease in RKKY coupling.¹¹ For multilayer structures ($[F/N]_N$), RKKY coupling is extremely significant as the F layers are coupled either ferromagnetically or antiferromagnetically. As film

roughness increases, RKKY coupling decreases as the long range interaction of electrons between layers is disrupted by the “waviness” of the interface and the short range magnetostatic coupling increases.⁴

The overall change in GMR varies as one or several of these effects acts to benefit or detract from the magnetic behavior of the thin film. Where the effect is favorable for the achievement of an AP state, the GMR is enhanced. Conversely, if the increase in roughness leads to an increase in magnetic coupling between layers, which hinder the AP state, GMR decreases.

3.2 - Electronic Behavior Effects

As magnetic behavior of films is affected by grain size and formation, there are also influences on electronic behavior of GMR thin films within the bulk of ferromagnetic layers and at the interfaces between layers. Grain formation and boundaries have an effect on spin-dependent, spin-independent, and spin-flip scattering. Increases in grain size, diffuse grain boundaries, and depth of valleys can produce significant intermixing of layers at the interfaces. For a structure with a Cu interlayer, as with our films, the increased intermixing can produce an increase in the resistivity of the thin film.^{4, 8} Pure Cu is highly conductive, but intermixing produces Cu alloys which can cause an increase in overall film resistivity.

Spin-independent scattering encompasses scattering processes arising from lattice mismatches, dislocations, impurities, and other microstructure effects of film growth that may enhance film disorder.^{1, 12} In addition, all of these factors influence film resistivity and are dependent on the interfacial roughness. As film roughness increases, the resistivity increase is related to the larger number of defects present in the crystalline

structure. An increase in the number of dislocations and imperfections influences the mean free paths and spin diffusion lengths of electrons within the materials used in multilayer thin films. The added stress on the structure can lead to an increase in spin-independent bulk scattering.⁶ The increase in spin-independent scattering causes an increase in both the parallel and antiparallel resistivities for both CIP and CPP-GMR and may have an effect on GMR.

The electron mean free path, spin diffusion length or spin-flip scattering, and interfacial diffusion also influence spin-dependent scattering processes.^{11, 13-15} The effects on electron scattering differ for the majority and minority electrons. For a multilayer thin film, the first two properties vary from layer to layer (assuming different layer materials) for electrons of the same polarization. Within individual layers, electron scattering differs between the majority and minority spins. Interfacial diffusion can create a new layer at the interface with properties different from either of the constituent layers. Generally, the effect on GMR is more significant because of the disparity between spin polarizations. The result, however, is ambiguous. Researchers have reported both degradation and enhancement of GMR.^{6, 15, 16} The ambiguity could suggest that one than more mechanism is at work and the combination determines the effect on GMR.

Short Mean Free Path Limit

The influence of roughness on GMR can be theoretically discussed in terms of the comparison of two length scales: the electron mean free path and the thickness of the individual layers in the multilayer structure. Solutions to the Boltzmann transport equation have been found for two limiting cases¹³. In the short mean free path limit, the

electron mean free path (~ 100 nm for Cu and 10-40 nm for Co), λ_e , is shorter than the thickness of the layers. In the CPP structure, the roughness in this limit can result in a less resistive path of travel for the electrons, reducing the GMR.¹³ In effect, a “short circuit” occurs within the multilayer as electrons are shunted through less resistive layers of the film without propagating through the more resistive layers, decreasing the spin-dependent scattering. In addition, an increase in spin-flip scattering can occur in which the polarized electron “flips” its original spin before propagating through the entire film. For the CIP direction, an increase in interfacial roughness can disrupt the path through the lower resistivity layers and force the electrons to impinge on higher resistivity layers which can increase the spin-dependent scattering, beneficial to GMR.¹³ Typically, however, the overall result is not beneficial to the GMR as the spin-independent scattering may have a greater increase than the spin-dependent scattering.

Long Mean Free Path Limit

In this limit, λ_e is longer than the layer thickness. The electron path is longer for the “wavy” interface than for a flat interface.¹³ As a result, electrons have a greater probability of being scattered while traveling the length of the film resulting in an increase in both spin-independent and more significantly, spin-dependent scattering. In this limit, spin diffusion lengths of electrons are long and they will propagate further before switching polarizations. The increase in scattering creates an increase in resistivity that affects both CIP-GMR and CPP-GMR. The different length scales just discussed have been used to explain why some experiments see an increase in GMR with roughness, while some see a decrease or no change¹³.

This thesis describes experiments designed to explore the effects of interfacial roughness on both CIP and CPP-GMR as applied through the substrate. For Chapters 7 and 8, we attempt to produce substrate roughness that is on the order of the electron mean free path in the materials chosen for these studies, although almost all of the roughness we did produce had average wavelengths much larger than electron mean free path. We discuss possible mechanisms by which the GMR could be changing due to this roughness and attempt to determine whether the primary effect is on spin-independent or spin-dependent scattering.

3.3 - References

- ¹ M. C. Cyrille, S. Kim, M. E. Gomez, et al., Phys. Rev. B **62**, 15079 (2000).
- ² W. C. Chiang, W. P. Pratt, Jr., M. Herrold, et al., Phys. Rev. B **58**, 5602 (1998).
- ³ D. T. Pierce, J. Unguris, R. J. Celotta, et al., J. Magn. Magn. Mater. **200**, 290 (1999).
- ⁴ W. F. Egelhoff, Jr., P. J. Chen, R. D. K. Misra, et al., Journal of Applied Physics **79**, 282 (1996).
- ⁵ H. De-Hua, Z. Jian-Gang, J. H. Judy, et al., J. Appl. Phys. **81**, 340 (1997).
- ⁶ M. Velez and I. K. Schuller, J. Magn. Magn. Mater. **184**, 275 (1998).
- ⁷ N. Spaldin, *Magnetic Materials: Fundamentals & Device Applications* (Cambridge University Press, New York, 2003).
- ⁸ S. Vilain, J. Ebothe, and M. Troyon, J. Magn. Magn. Mater. **157-158**, 274 (1996).
- ⁹ M. Li, Y. P. Zhao, G. C. Wang, et al., Journal of Applied Physics **83**, 6287 (1998).
- ¹⁰ B. Seongtae, N. Matsushita, S. Zurn, et al., IEEE Trans. Magn. **36**, 2850 (2000).
- ¹¹ K. Xia, P. J. Kelly, G. E. W. Bauer, et al., Phys. Rev. B **63**, 064407/1 (2001).
- ¹² R. Schad, P. Belien, G. Verbanck, et al., Phys. Rev. B **57**, 13692 (1998).
- ¹³ J. Alicea and S. Hershfield, J. Appl. Phys. **93**, 7930 (2003).
- ¹⁴ J. Barnas and Y. Bruynseraede, Phys. Rev. B **53**, 5449 (1996).
- ¹⁵ A. Zambano, K. Eid, R. Loloee, et al., J. Magn. Magn. Mater. **253**, 51 (2002).
- ¹⁶ M. C. Cyrille, S. Kim, M. E. Gomez, et al., Phys. Rev. B **62**, 3361 (2000).

Chapter 4 — Film Fabrication

This thesis involves the study of metallic thin films produced by sputtering and evaporation. This chapter discusses the basic theory behind each deposition process and describes the specific experimental configurations employed for this thesis. An overview of the film growth procedures and conditions is also provided.

4.1 - Sputtering

Sputtering is a common physical vapor deposition process for magnetic multilayer thin film fabrication. Fundamentally, sputtering involves ionized atoms, colliding elastically, which transfer energy while conserving momentum.¹ The ionized atoms impact a target surface causing removal of material, which then assumes vapor form and is deposited onto a substrate. Sputtering can have a high deposition rate, allowing for the growth of a large volume of films. The large source area and low energy of the sputtered particle yield smooth films with high film uniformity and conformality. The sputtering chambers at the College of William & Mary, the National Institute of Standards & Technology (NIST), and Michigan State University have designed systems, which can deposit on numerous substrates at the same time under the same growth conditions. The experimental setups at W&M and NIST use a dc magnetron configuration while the system at MSU is a combination of dc magnetron and triode sputtering.

Sputtering is a low-vacuum process, usually operating at 1 to 100 mtorr. In sputtering, an introduction gas is excited to a plasma by producing a potential difference

between a cathode and an anode and drawing electrons from the cathode. The energetic ions from the plasma discharge strike the target, removing atoms from the target. The plasma discharge is thus comprised of electrons, ionized gaseous species, and neutral atoms from both the introduction gas and the target. Essentially, the glow discharge is electrically neutral as the densities of the charged particles are equal. Light emission from excited atoms gives the discharge its glow. On either side of the plasma are located electrically charged regions referred to as “sheaths”. The cathode sheath has a positive charge density as ions flow through it towards the cathode. The anode sheath is primarily comprised of electrons. Since charge is conserved, the ion current density to the cathode must equal the electron current density to the anode. Ion movement through the sheath is assumed to be collisionless but some collisions may occur as ionized gas species pass through the sheath and excite any neutrals that may be present. However, ions arrive at the target with enough kinetic energy to “knock out” target atoms, typically 1-3 keV. Highly energetic atoms, typically 3-5 eV, are ejected from the target, dispersed into the gas phase and conveyed to the substrate, which acts as an anode. Target atoms impinge on the substrate surface, condensing into a thin film. Typically, thin film thicknesses range from a monolayer to several microns.

The oldest and simplest type of sputtering is dc sputtering. A parallel-plate cathode-anode configuration supplied by a high-voltage dc power source on the order of 3 kV is the most widely used arrangement. Typically, the target area is tens to several hundred square centimeters and is spaced several centimeters from the anode. Generally, parallel-plate configurations are designed such that the anode has a significantly larger area than the cathode. This increases the sputtering rate by increasing the current flow to

the cathode. Commonly, however, dc sputtering is not used in thin film deposition because of its limitations. Film deposition rates are too low and several types of materials cannot be sputtered, such as insulators. With conductive targets, an insulating layer of electrons can form on the target reducing the deposition rate further. There is also a considerable probability for secondary electrons to be lost to the chamber wall or anode without undergoing ionizing collisions with the sputtering gas. Another disadvantage is the inability of dc sputtering to sustain the plasma, as electrons are lost to the anode. The magnetron was designed to remove or limit the disadvantages present in dc sputtering. Other types of sputtering include but are not limited to radio frequency (RF) sputtering, hollow cathode sputtering, and ion beam sputtering. Information concerning these types of sputtering as well as others can be found in Mahan¹ and Bunshah.² Detailed information can also be found in Ohring³ and Smith.⁴

4.2 - DC Magnetron Sputtering

Magnetron sputtering enhances the sputtering process by localizing electrons over the cathode to increase the probability of ionization for the introduction gas. A schematic of our deposition system is shown in Figure 4.1. In this configuration, the target material serves as the cathode with a negative potential, typically 300-500 V, relative to the substrate, which has a floating potential. The grounded chamber wall acts as the anode. Secondary electrons released from the cathode ionize an introduction gas, usually Ar, through collisions with neutral atoms, where imparted energy excites the gas species. The ionized gas accelerates towards the cathode by the high negative potential, strikes the target surface with enough kinetic energy to eject predominately neutral target atoms through secondary backward scattering.

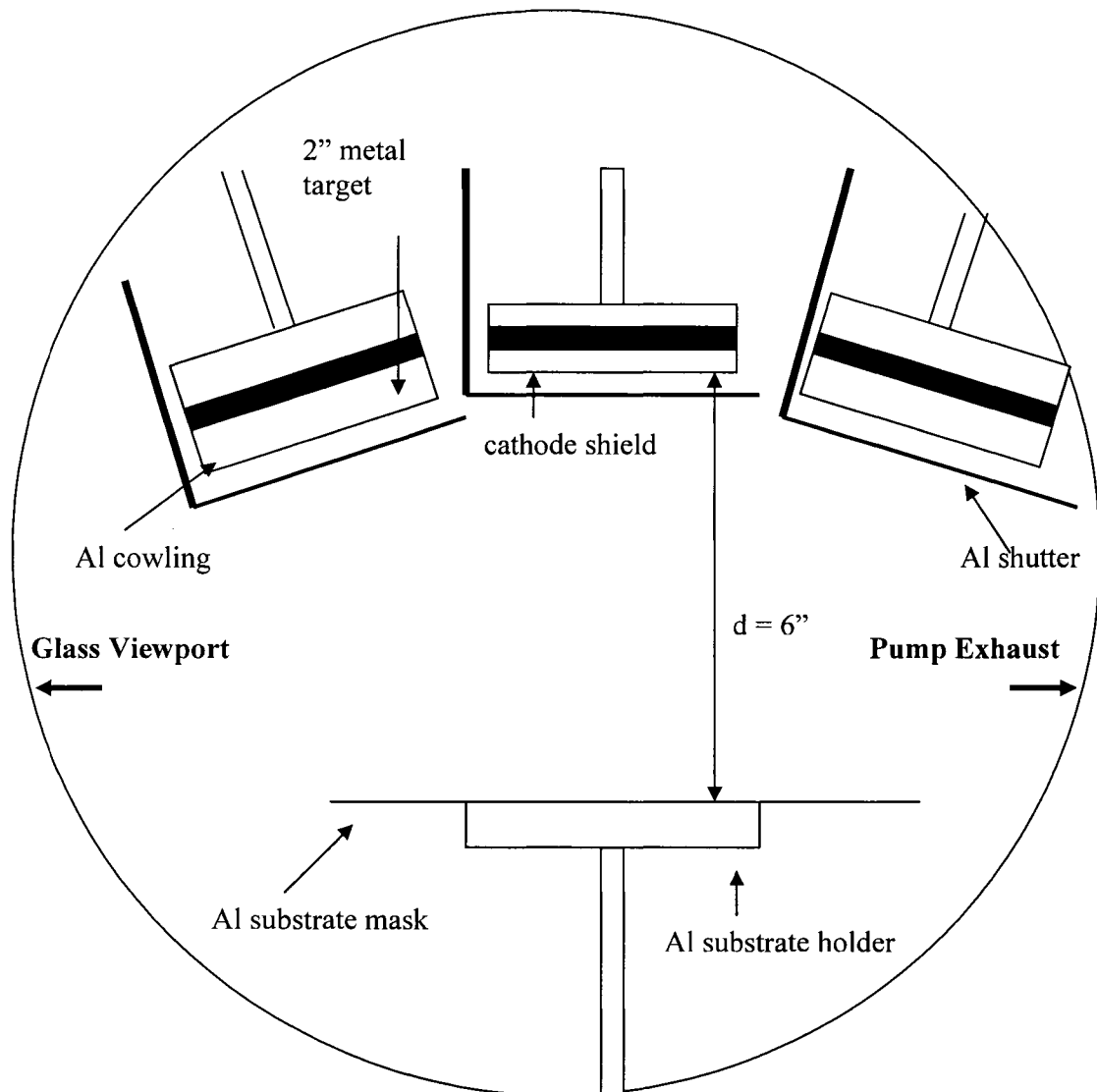


Figure 4.1: A schematic of the dc magnetron sputtering system located at W&M used to fabricate most films. Four dc magnetron guns are located $\sim 6''$ from the substrate. Multilayer thin films are grown using computer-controlled shutters to expose each gun in succession to the substrates.

Common interpretation holds that this process creates a linear cascade within the target. The plasma, localized above the target surface, is sustained by an electric field and a confining magnetic field. The flux of the magnetic field lines are shaped by two permanent magnets positioned behind the cathode: a ring magnet and a center magnet.

Initially losing some energy during the first orbit, electrons are trapped by the B-field. In a series of orbits with decreasing radii in the $-\vec{E} \times \vec{B}$ direction where E and B are the electric and magnetic field vectors, respectively¹, the electrons continue to collide with neutral atoms of the introduction gas, creating more ions. In this way, the electrons are localized over the target and continue to create ions.

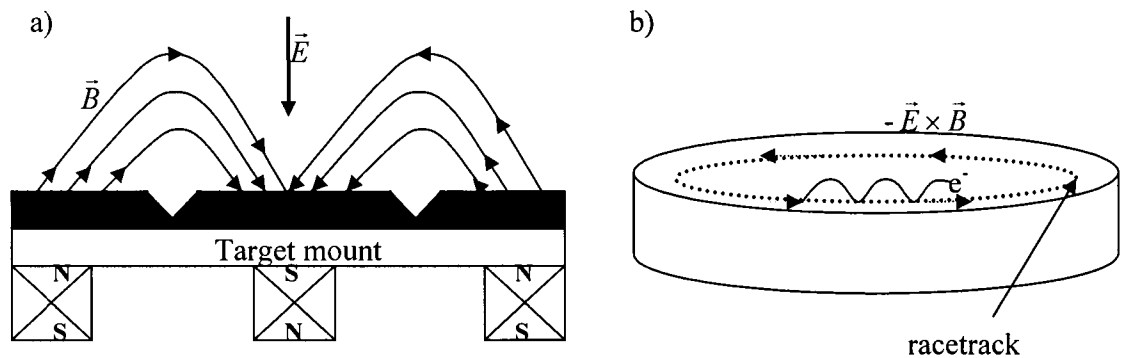


Figure 4.2: a) Schematic of cathode source. The magnetic field lines localize electrons over the target surface. The drift is strongest where the magnetic field is parallel to the target surface. b) The drift velocity contains the electron density in an annular region.

Secondary electrons gyrate around the magnetic field lines in a helical pattern in relation to the Lorentz Force. The plasma drift velocity facilitates electron trapping:

$$\vec{v}_d = \frac{\vec{E} \times \vec{B}}{B^2} \quad (4.1)$$

The helical motion of the electrons in conjunction with the drift velocity generates an annular erosion outline in the target. (Colloquially, the outline is referred to as the “racetrack”.) The speed at which the erosion deepens is determined by numerous factors, including the deposition rate, sputtering yield, and particle energies.

The W&M deposition chamber has four sputtering sources each with a computer-controlled pneumatic shutter. To prevent cross contamination during deposition, two

sources are encased in aluminum cowlings and a rectangular aluminum divider is located between the top and bottom sources.

4.3 - Triode Sputtering

Triode sputtering, while a form of dc sputtering, employs three electrodes instead of two. The hot-cathode triode is the most common configuration. The cathode and target are independent of each other. Instead, a cathode filament and an anode are positioned in close proximity to the target with the cathode-anode assembly parallel to the target. The filament is heated to a high temperature generating thermionic emission of electrons, which is enhanced with an injection of electrons increasing the gas ionization probability. A high negative target potential attracts the subsequent ions bombarding the surface and ejecting material in the gas phase. The operating pressure for this configuration, 0.5 to 1 mTorr², is lower than magnetron operating pressures. While the current is typically higher for a triode system, the potential is lower compared to dc magnetron sputtering.

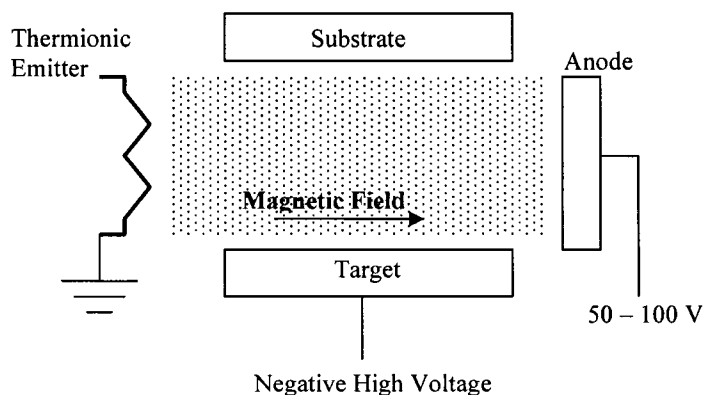


Figure 4.3: Hot cathode sputtering injects electrons into the plasma by thermionic emission increasing the ionization probability of the carrier gas.

Triode sputtering provides a higher deposition rate at a lower pressure than dc magnetron sputtering. The localization of the carrier gas over the target area in conjunction with the use of a filament cathode allows for more efficient sputtering of the target without the need for a higher partial pressure of the carrier gas. The disadvantage of triode sputtering is an uneven erosion of the target material due to nonuniform plasma coverage over the target surface.

4.4 - Boat Evaporation

Evaporation is another common physical vapor deposition process, in which atoms obtain energy through thermalization rather than momentum transfer. The kinetic energy involved is orders of magnitude smaller than in sputtering. Consequently, evaporated atoms have limited mobility over the substrate surface. Evaporation, in contrast to sputtering, is a high vacuum process (pressure less than 10^{-6} torr). It does not require a carrier gas to promote deposition. High thermal energies, which are orders of magnitude less than the energies involved in sputtering, are imparted to the material, which vaporizes or sublimates into the gas phase. The thermalized atoms are transported to the substrate and condense on the surface. Their lower kinetic energy results in most particles remaining where they condense.

A boat evaporator, located at MSU, was used to create the gold nanodots discussed in Chapter 8. In boat evaporation, a refractory metal houses the material to be evaporated, referred to as the evaporant. A high current, on the order of 100 A^1 , is applied to the boat, resistively heating it and, eventually, thermalizing the evaporant. The vapor pressure above the evaporant is less than the thermal equilibrium vapor pressure. Thus, the device achieves a non-equilibrium steady-state. In other words, there is very

little return flux to the boat. The vaporized material follows a Cosine Law of Emission (to be discussed shortly), somewhat similar to that of sputtering.

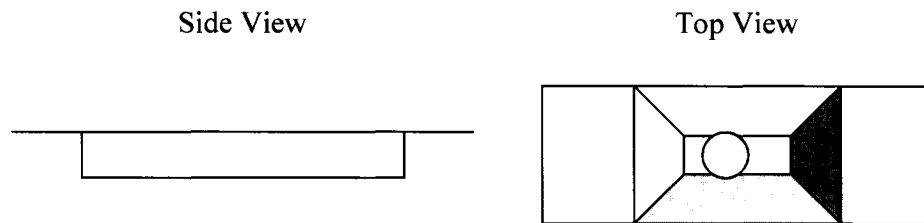


Figure 4.4: Top and side view of boat evaporator with Au charge. The boat evaporator is constructed of a refractory metal that is resistively heated to thermalize the charge material located within.

Evaporation was used to produce nanodots for the work described in Chapter 8 because sputtering was too energetic for deposition. The atoms migrated around the initial polymer nanosphere template, producing a connected honeycomb pattern rather than individual dots.

4.5 - Film Fabrication Conditions

The majority of the films were deposited by the dc magnetron sputtering system at W&M. The material is ejected from the target in the shape of a plume, determined by a function of $\cos^n \theta$, known as the Cosine Law of Emission.

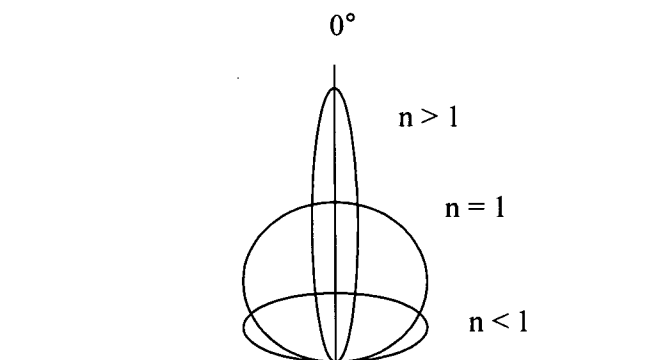


Figure 4.5: The Cosine Emission Law describes the distribution of ejected atoms from a point source. The shape is dependent on energy and angle of incidence.

The shape and depth of the plume are determined by the projectile or ion energies and angle of incidences. Typically, target or recoil atoms are emitted as neutral atoms and leave with an energy dependent on the projectile energy. The distribution of all recoil atoms can be described as having a $\cos \theta$, undercosine ($n < 1$), or overcosine ($n > 1$) shape. The cosine emission of atoms can be related to the energy of the incoming incident ions. Generally, an overcosine distribution is representative of higher energy ions ($E_{\text{ion}} > 10 \text{ keV}$) while an undercosine distribution represents energies lower than 1 keV. In the former case, incident ions arrive with enough kinetic energy to be implanted into the bulk of the target. Only target atoms within a specific radius are ejected and generally with a specific direction. In the undercosine case, not enough kinetic energy is available to allow target atoms to break atomic attractions. The energies used for sputtering and evaporation, typically produce a $\cos \theta$ distribution as this provides good coverage and uniformity.

The chamber at W&M is a high vacuum design with an introduction chamber to allow for fast loading and unloading of films. The design of the substrate holder allows for deposition onto six $\frac{1}{2}$ " x $\frac{1}{2}$ " substrates or smaller under the same growth conditions. The mask located in the main deposition chamber can be removed allowing for deposition onto one 3" wafer. A cryopump provides the main pumping of the main chamber and can achieve a base pressure in the 10^{-9} torr range. A turbo pump located on the introduction chamber can achieve a pressure in the 10^{-7} torr range minimizing the pressure differential between the two chambers. Heaters attached to the exterior chamber wall provide a baking temperature of 150 °C to help remove water from the system prior

to deposition. In effect, this system design allows for the deposition of GMR multilayer thin films and allows us the capability to grow several films in one run.

The sputtering system located at NIST is similar in design to the system at W&M with a few exceptions. It is almost entirely computer controlled and can deposit multilayer thin films onto several substrates simultaneously. It is also equipped with an introduction chamber to provide for the loading and unloading of substrates without breaking vacuum in the deposition chamber.

Michigan State's sputtering system is an ultra-high vacuum chamber and is designed to deposit both current-in-plane and current-perpendicular-to-the-plane films. The growth of CIP films is similar to the growth of films at both W&M and NIST with four triode sputtering sources in conjunction with two dc magnetron sources. For CPP films, thin films must be deposited so that current flow is perpendicular to the film surface. As discussed in chapter 2, the resistance of CPP films is on the order of $n\Omega$ and requires superconducting contacts in order to measure the resistance and resistivity of the films. To this end, the system design at MSU uses a rotating mask to deposit niobium (Nb) contacts in a cross-linking pattern, illustrated in Figure 4.6.

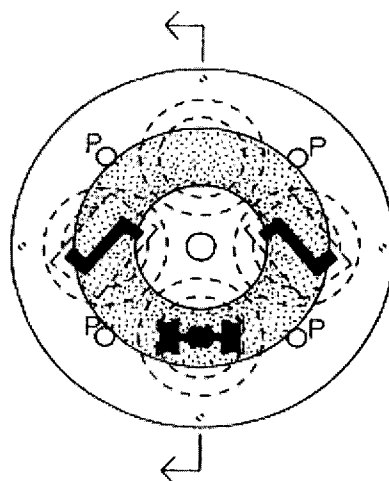


Figure 4.6: Rotating mask for CPP structured thin films seen from substrate side. Courtesy of Michigan State.⁵

The strips are deposited as a top and bottom layer so that the overlay of both Nb layers over the thin film defines an area in which the CPP-GMR is measured, illustrated in Figure 4.7. The strips are approximately $2\ \mu\text{m}$ thick and due to the superconductivity of Nb, are ideal for CPP measurements. With this configuration, both the CIP and CPP-GMR can be measured.

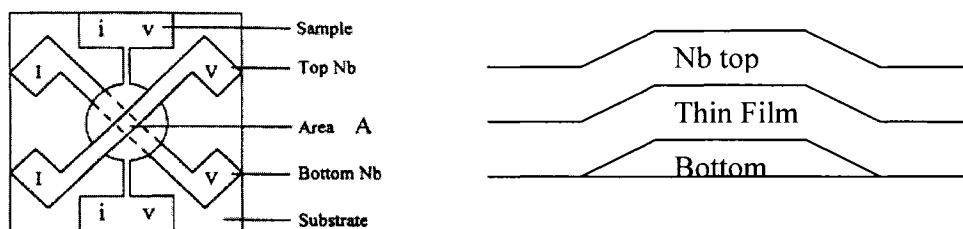


Figure 4.7: Top view (left) of CPP thin film structure. Current flow is applied perpendicular through structure by attaching leads to Nb cross strips. Cross-sectional view (right) illustrates direction of current through film. Note: GMR only measured over area (A) over overlay. CIP-GMR can also be measured in this configuration. Courtesy of Michigan State.

4.6 - References

- ¹ J. E. Mahan, *Physical Vapor Deposition of Thin Films* (John Wiley & Sons, Inc, New York, 2000).
- ² R. F. Bunshah, *Handbook of Deposition Technologies for Films and Coatings* (Noyes Publications, Westwood, 1994).
- ³ M. Ohring, *Materials Science of Thin Films: Deposition & Structure* (Academic Press, New York, 2002).
- ⁴ D. L. Smith, *Thin-Film Deposition: Principles & Practice* (McGraw-Hill, Inc, New York, 1995).
- ⁵ S. F. Lee, Q. Yang, P. Holody, et al., *Physical Review B-Condensed Matter* **52**, 15426 (1995).

Chapter 5 — Characterization Techniques

As this thesis focuses on the effect roughness has on thin films, we selected characterization instruments that would provide information on the scale of roughness and the resulting magnetic properties of thin films chosen for our various studies. This chapter discusses the primary tools used for this research. The atomic force microscope was the primary characterization tool used to quantify surface roughness and topography of our single layer and GMR thin films. Surface morphology was characterized by a scanning electron microscope. Magnetic properties of our thin films were measured with several different tools: a vibrating sample magnetometer, a superconducting quantum interference device, and magneto optic Kerr effect. Giant magnetoresistance was measured with the four-point probe method. These instruments are the traditionally accepted characterization tools for thin films research and technology.

5.1 – Surface Techniques

Atomic Force Microscopy

Atomic Force Microscopy (AFM), a type of scanning probe microscope (SPM), is a high-resolution imaging technique that operates by sensing the force between a probe tip and a sample surface. It is commonly used by researchers to observe molecular and atomic level features in real-space without requiring a vacuum. It can be used to image a variety of samples because it does not rely on sample conductivity and can be operated in gaseous or liquid environments. Under good conditions (sharp probe tips, a stiff

cantilever, and ultrahigh vacuum), it can resolve surface features as small as an atomic lattice in real space.¹ The tip, held at the end of a cantilever that acts as a spring, is brought into close proximity with the surface to be imaged. The resulting applied force to the surface can be calculated from Hooke's Law²:

$$F = -kx \quad (5.1)$$

where k is the spring constant of the cantilever and x is the deflection of the cantilever. Interactions arising between the tip and surface include van der Waals', capillary, and electrostatic repulsive forces. These forces are applied to the tip, bending the cantilever upwards. Theoretically, this force between the film surface and the tip occurs via a single atom, shown in Figure 5.1. The degree of tip deflection is measured by a diode laser reflected off the back of the cantilever on to a split or sectioned photodiode. As the cantilever is deflected, a photocurrent imbalance between the top and bottom diodes produces a signal proportional to the degree of cantilever deflection. As the spring constant of the cantilever is known, the force can be calculated using the amount of deflection detected by the photodiode. By keeping the force constant during scanning, the vertical movement of the tip follows the surface profile and is recorded as the surface topography by the AFM. A scanner constructed of piezo electrodes, attached to the back of the cantilever, manipulates the motion of the tip over the surface. As the tip moves across the film surface, a dual trace pseudo-color image of the scanned area is produced. In effect, the tip traces a line along the surface and then retraces the same line. The dual trace sweep aids in the alignment of the tip with the surface and shows the drift of the tip from the original trace line.

Most atomic force microscopes use cantilevers and tips which are microfabricated from Si_3N_4 , SiO_2 , or Si and are pyramidal in shape.^{2, 3} Tip diameter is important as features smaller than the tip diameter cannot be accurately imaged. Additionally, variations in tips can lead to interactions between several atoms (instead of a single atom-atom interaction between the probe tip and the sample surface) and can produce variations in measurements. Ideally, the same tip or same type of tip should be used for all measurements. The lifetime of the tip is partially determined by the way, in which the sample surface is scanned. There are three primary modes for imaging a surface using the AFM: contact, non-contact, and tapping mode.

Contact mode brings the tip and the sample surface into physical contact as the tip is dragged over the surface, generally with forces in the 10^{-6} to 10^{-8} N range. The close proximity of the tip with the surface causes an overlapping of electron clouds. As a result, the tip is pushed away physically from the surface by electrostatic repulsive forces.¹ This mode provides a high resolution of the sample surface but can be damaging to soft surfaces.

In non-contact mode, the tip-sample distances are typically tens to hundreds of angstroms apart.¹ The attraction between the tip and sample are the weaker van der Waals' forces and forces are generally on the order of 10^{-12} N.¹ Typically, the cantilever oscillates at a frequency between 100 and 400 kHz to detect the small forces involved. Changes in surface topography result in changes in the vibrational amplitude of the tip. As described above, changes in amplitude are detected by the photodiode and converted to tip-sample spacings allowing the surface to be imaged. Due to the lack of physical

contact, soft surfaces can be imaged with minimal surface contamination and tip degradation.

The final mode, tapping mode, is a combination of contact and non-contact mode. In tapping mode, the cantilever oscillates at or near its resonance frequency, ~ 300 kHz for the tips used to image our films. At the bottom of its swing, the tip contacts the surface lightly tapping it. Constant oscillation amplitude, maintained by a feedback loop, sustains a continuous tip-sample interaction during imaging. Generally, the tip contacts the surface with a spring constant between 20 and 100 N/m. Tapping mode is designed to lessen damage to the film surface by using smaller forces for soft films and minimizing lateral forces eliminating scraping of the film surface. While tapping mode is less capable of obtaining atomic resolution images, it has a higher lateral resolution than contact and non-contact mode.

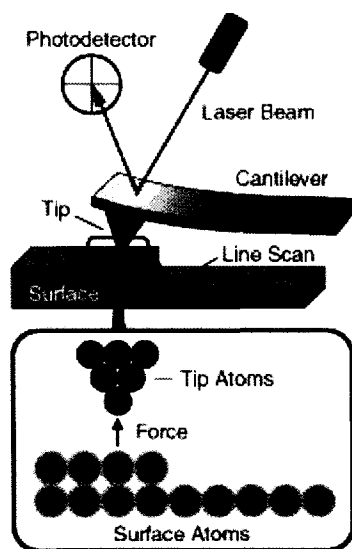


Figure 5.1: Illustration of AFM scanning film surface. A tip attached to a cantilever oscillating at a specific frequency moves across the surface. A photodiode detector records deflections of a reflected laser aligned with the back of the cantilever. Courtesy of Molecular Imaging.

For this thesis, a Digital Instruments Nanoscope was used in tapping mode to obtain the roughness measurements. Analysis of image scans provided information concerning surface roughness and the measurements were used to quantify roughness. Various feature properties were obtained from the image scans, including feature and grain sizes, heights, and peak-to-peak lengths. Roughness measurements from AFM scans were compared with various magnetic properties in an attempt to find a correlation. The AFM used for this thesis has a vertical resolution of 1\AA and noise levels present in the image scan of 1\AA . The lower limit of the roughness scale for this thesis is on the order of nanometers.

The main disadvantage of the AFM is the image size, which can only show a maximum height on the order of microns and a maximum area of around $100 \times 100 \mu\text{m}$. For our purposes, the measurement of heights greater than one μm is not necessary. However, measurable area is limiting considering the size of the film, $12 \times 12 \text{ mm}$ or $4 \times 12 \text{ mm}$, and the deviation in roughness measurements (discussed in Chapters 6-9). Typically, three scans were taken on each sample at a rate of $\sim 0.5 \text{ Hz}$, a rate that provided a good dual trace sweep over the film surface. Each scan is comprised of a 256×256 -line sweep giving a 65536 -point resolution. Additionally, each scan represents a different location on the same sample providing a survey of the roughness uniformity. This arrangement, while situated on an air stabilization table, is still sensitive to extraneous vibrations, which can cause streaks to appear in the scan that are assumed to be part of the film by the software. In addition, as the tips began to degrade after $\sim 8 \text{ hr}$, the same type of tip was used for all measurements, but not the exact same tip.

In tapping mode, the procedure to obtain a scan is as follows. A sample is placed onto the sample stage and held in place by a low vacuum. The stage is electronically manipulated to position the sample under the tip stage. Then, an optical camera is used to locate the tip, focus the sample surface and position the tip over the sample edge. The tip stage is slowly lowered, so as not to bump the surface and damage the tip, until the sample edge comes into sharp focus, usually only a few millimeters from the sample surface. When properly aligned, the tip sum is less than 2 and the vertical deflection is ~ 0 . A red dot, representing the location of the laser with respect to the tip, is centered on a grid on the computer monitor. After alignment, the tip is tuned to insure that resonance occurs at ~ 300 Hz, an indication of good tip performance. When the AFM is within these parameters, the tip is lowered into contact with the surface using the Nanoscope software. As the surface is scanned, the dual trace can be adjusted to insure overlap of the trace-retrace lines, eliminating drift by the tip.

Analysis of AFM scans was made without flattening the image scan, which the software would have included in the roughness measurements. In order to obtain accurate measurements, specific criteria for film analysis were followed. First, films without streaks or apparent surface contaminants were analyzed for roughness. For films with streaking, only the areas without streaking were analyzed for roughness. Scans with significant streaking were not used.

Data from the 256 x 256 point scans was digitized and the scans stored on the computer. An analysis program provided by Digital Instruments analyzed the digitized data and provided numbers such as peak height (Z), average roughness (R_a), and root

mean square (σ_{rms}) values for roughness. The root mean square roughness was calculated according to this formula:

$$\sigma_{rms} = \sqrt{\frac{\sum_i^N (Z_i - \bar{Z})^2}{N}} \quad (5.2)$$

The average roughness was calculated according to this formula:

$$R_a = \frac{\sum_i^N |Z_i - Z_{CP}|}{N} \quad (5.3)$$

where Z_i represents individual peak heights, \bar{Z} represents the average peak height for a given scan area, and Z_{CP} represents the peak height of the center plane of the scan area. Roughness data was taken from unaltered scans using the Nanoscope software. Feature height and depth were represented by variations in color. For sloped scans, flattening, performed through the software, was used to level the scan image for roughness analysis. The error reported for the AFM roughness data was calculated as the standard deviation from the mean of multiple scans. Error in the measurement of roughness can be due to dust or impurities on the surface, a worn tip or significant vibrations through the floor.

Scanning Electron Microscopy

Scanning Electron Microscopy (SEM) is also a high-resolution 2-dimensional imaging device that uses low and medium-energy electrons to image the surface morphology. It is also able to provide information of the material composition just below the surface. Unlike the AFM, the SEM is dependent on the sample conductivity and is unable to image nonconductive samples effectively without first coating the sample with a conductive material. It is also necessary to operate an SEM in an ultrahigh vacuum

system. However, sample surfaces can be imaged over a larger scan area with an SEM compared to the scan size of an AFM. An electron microscope is capable of scanning at near real-time (although at relatively low quality) allowing for faster imaging of the sample surface. Unlike the AFM, which allows a true three-dimensional surface profile, the electron microscope provides a two-dimensional projection or a two-dimensional image of a sample unable to resolve atomic sizes.

For this research, SEM images were obtained using the Hitachi S-4700 cold field emission FE-SEM, located at W&M, which incorporates dual high-resolution secondary electron detectors with low-voltage backscattered electron imaging providing information about the film surface and the bulk of the sample. The electron source is provided by field emission from a cathode wire made of tungsten. The high field ($>10^7$ V/cm) at the tip decreases the size of the potential barrier the electron must overcome for emission eliminating the need for any thermal energy to overcome the electron work function. The electrons are accelerated through an anode plate, typically with voltages between 1 and 30 kV.⁴ After leaving the anode, the electrons are focused into a fine beam by condensing lenses. The condensing lenses control the beam spot size on the sample surface controlling the resolution of the image. Scanning coils are used to direct the electron beam across the sample surface. The spot beam scanning the sample surface is synchronized with the spot display of a cathode ray tube (CRT). One set of detectors analyze secondary electrons scattered from the film surface. Image contrasts are a result of intensity changes in the secondary electron emission scattered from the surface. A second detector analyzes the number of backscattered electrons, which is linked to atomic number, to determine the film composition of the sample. As stated above, the electrons

are scattered from the beneath the surface and the depth to which the penetration occurs is dependent on the beam energy. Figure 5.2 illustrates the basic components of an SEM.

The SEM was used to measure nanodot size and spacings for the films discussed in chapter 9 where it was necessary to gain a better observation of overall film uniformity but not quantify root-mean-square roughness.

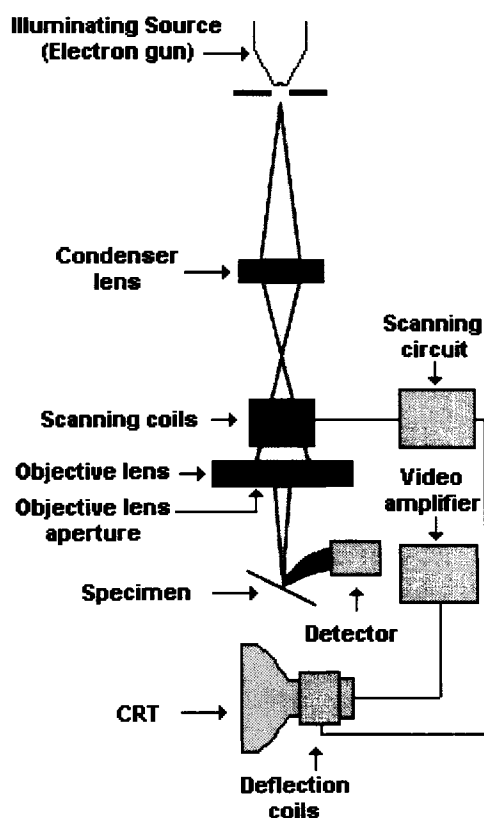


Figure 5.2: Schematic of SEM. The SEM provides high-resolution 3D images of sample morphology

5.2 – Magnetic Instruments and Techniques

Superconducting Quantum Interference Device

The superconducting quantum interference device (SQUID) measures change in magnetic fluxes and has a high sensitivity to small magnetic signals. While it is

commonly used to measure hysteresis and magnetoresistance of thin films, it is used in a wide variety of applications, ranging from the biological to the geophysical.⁵ It is the most sensitive of the magnetometers, able to detect signals as small as 10^{-11} emu using sensitive current-to-voltage converters. There are two types of SQUIDs: the resonant frequency (RF) SQUID and direct current (DC) SQUID. Both types of SQUIDs are in use today. In most systems in use today, the SQUID sensor is located inside a small cylindrical, superconducting magnet which sits inside a liquid ^3He dewar, achieving temperatures as low as 4.2K. The SQUID sensor is comprised of a superconducting ring with one (RF) or two (DC) regions or 'weak links' called Josephson junctions. The junction length is on the order of the penetration depth of the superconducting material and weakens the superconductivity. Typically, the Josephson junction is constructed of an insulating barrier in which the superconductivity is weakened. Below a critical temperature (T_c), a supercurrent exists within the superconducting ring as the electrical resistivity is eliminated. In a closed loop, the supercurrent, in theory, experiences no loss of direct current. This creates what is referred to as a persistent current.

If a bias current is applied, the initial voltage drop across the junction is zero but a phase-shifted current is introduced across the junction between the two superconductors. When the bias current reaches a critical limit, the phase difference becomes time-dependent and a voltage will appear. The voltage is now measured as a function of the current. Figure 5.3 shows the superconducting ring with a single Josephson junction.

For this thesis, a DC SQUID located at North Carolina A&T University was used to measure the hysteresis of the films discussed in Chapter 6. Generally, the DC SQUID has a slightly more complicated design due to the necessity to have two identical

Josephson junctions within the superconducting ring.⁵ This is offset by the simpler electronics needed for a DC SQUID compared with the RF SQUID.⁵

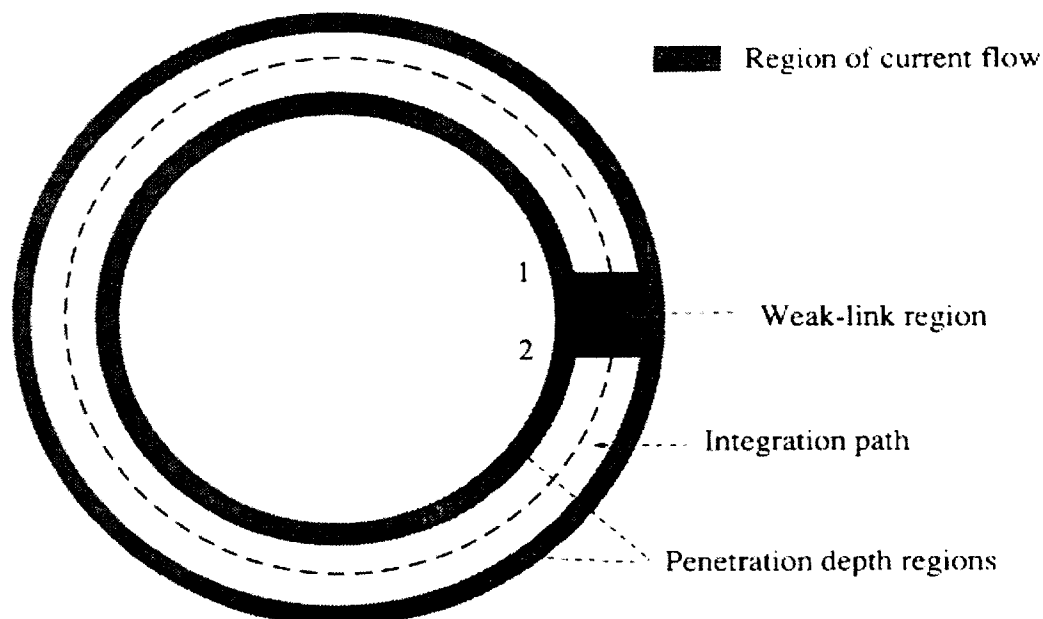


Figure 5.3: Superconducting ring interrupted by weak link. Schematic is typical of an RF SQUID. A DC SQUID would have two weak links. The weak link represents a Josephson junction. Image taken from Gallop "*SQUIDS, the Josephson Effects, and Superconducting Electronics*".

The device at NC A&T is a DC SQUID able to produce a field of ± 5 Tesla,⁶ fields as high as 7 Tesla can be produced.⁶ In standard DC transport, the sample probe is centered by stepping the sample through the pickup coils to insure the entire length of the film is situated within the scan region (8 cm).⁶ The sample is slowly stepped up through a set of superconducting pickup coils connected in series and referred to as the primary and secondary coils. The secondary coil is indirectly coupled to the SQUID sensor via superconducting wires. Helium gas drawn from the liquid helium surrounding the assembly flows around the sample tube uniformly cooling the sample. As a field is applied, one of the coils, typically called the primary coil, detects the small magnetic signals from the sample. The flux in the primary-secondary combination changes due to

the sample magnetic moment. The effect is a change in the persistent current within the superconducting ring connected to the primary coil. The SQUID sensor outputs voltages due to the variations in the persistent current proportional to the magnetic moment of the sample. Most SQUIDs in use today employ a gradiometer design instead of the basic flux transformer circuit described above.⁵ The primary coil is comprised of two or more identical coils in series each with n turns. In the case of two coils, they are wound opposite with respect to each other. A uniform external magnetic field will produce equal but opposite flux change in the two coils. For spatially uniform background fields, the persistent current will not be affected. However, a local magnetic field will produce different fluxes in the two primary coils and net change will be detected. This enables the SQUID to operate in noisy magnetic environments.

A SQUID's primary limitation is in the size of the sample it can measure. The width of the sample can be no greater than 5 mm. The SQUID's sensitivity to tiny magnetic signals and its ability to make superconductive measurements give it an advantage over other magnetic measurement techniques. A simple SQUID design is shown in Figure 5.4.

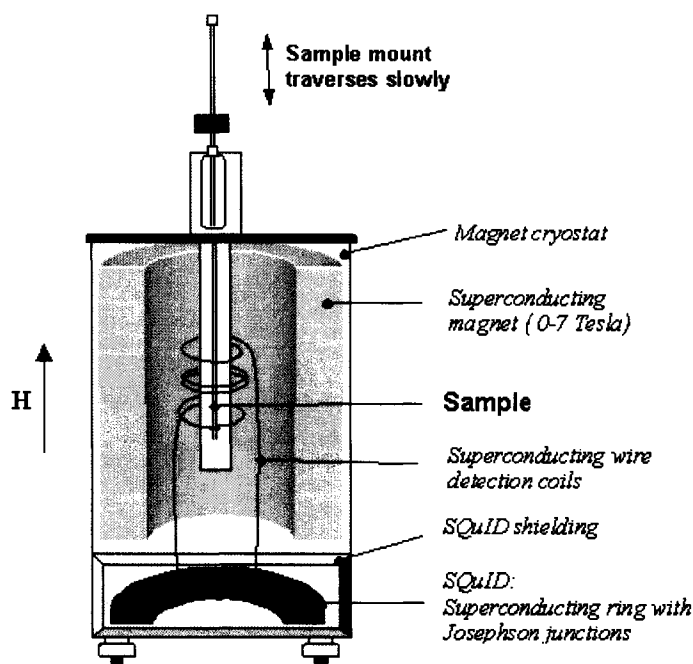


Figure 5.4: Simple schematic of a SQUID magnetometer. The SQUID is sensitive to tiny magnetic signals and is used for hysteresis and magnetoresistance measurements.

Vibrating Sample Magnetometer

The vibrating sample magnetometer, similar to the SQUID, measures magnetic signals. It has a flexible design that allows for easy mounting and exchange of samples. It is sensitive to magnetic moments as small as 10^{-5} emu and can be used to measure bulk as well as thin films. The VSM was used to measure the hysteresis of FL-CN_x thin films discussed in chapter 9.

The VSM is comprised of two electromagnetic coils, capable of a combined 2-3 Tesla, spaced some distance apart. This distance between the coils is adjustable allowing for samples of various widths to be characterized. The position that provides the strongest signal strength, referred to as the saddle point, is determined by aligning the sample drive between a set of pick-up coils with to an electromechanical transducer. The VSM is calibrated with a standard of known field before replacing the calibrated sample

with the film to be measured. A uniform field is applied, and the sample oscillates along the z-axis at a fixed frequency between the pick-up coils. This motion produces a flux change in the magnetic sample inducing a voltage across the terminals of the pick-up coils, which is proportional to the sample magnetization:

$$V(t) = C \frac{d\Phi}{dt} \quad (5.4)$$

where $\Phi(t)$ represents the (changing) flux in the pick-up coils caused by the moving magnetic sample. The signal from the coils is extremely small, on the order of a few nanoVolts, making the VSM sensitive to external noises.

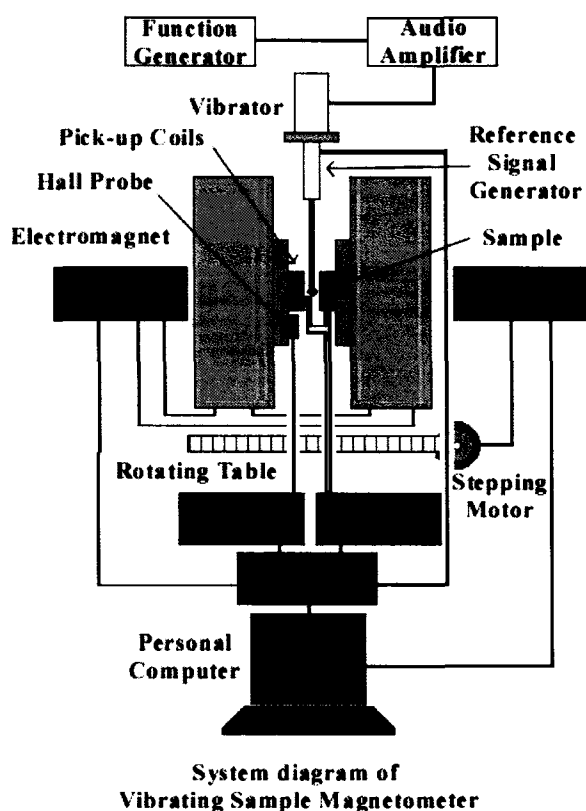


Figure 5.5: Schematic of vibrating sample magnetometer. The VSM is used to measure hysteresis of films. The sample oscillates between two electromagnetic coils inducing a voltage proportional to the sample magnetization.

Magneto Optic Kerr Effect

Magneto Optic Kerr Effect (MOKE) is a common technique used to measure the hysteresis of magnetic thin films through the rotation of reflected linearly polarized light off a sample. It is advantageous in that MOKE operates in ambient conditions and can be easily designed in a research lab. MOKE is thickness dependent with an effective penetration depth of approximately 20 nm and does not distinguish between individual layers.

The light is initially polarized in the transverse direction by the first linear polarizer. The polarized light is incident on the sample surface and can be represented by components of electric field in the plane of incidence (p) of the light and perpendicular (s) to this plane:

$$E_i = E_0 \cos \theta_{p1} \hat{p} + E_0 \sin \theta_{p1} \hat{s} \quad (5.5)$$

Here θ_{p1} is the angle of the first polarizer and E_0 is the incident electric field. The incident light is reflected off the sample and the reflected light is related to the incident light by:

$$E_r = SE_i \quad (5.6)$$

where S is a the sum of the longitudinal and transverse matrices written to represent changes in electric field upon reflection:

$$S = m_t^2 S^t + m_l^2 S^l \quad (5.7)$$

S^t and S^l are separate matrices for the transverse and longitudinal polarizations, respectively. They are given in Equation 5.7, where m_t and m_l are the transverse, M_t ,

and longitudinal, M_l , magnetizations divided by the saturation magnetization, M_s . The S matrices are written in terms of the Fresnel reflection coefficients (r):

$$S^{trans} = \begin{pmatrix} r_{pp}^t & r_{ps}^t \\ r_{sp}^t & r_{ss}^t \end{pmatrix} \quad S^{long} = \begin{pmatrix} r_{pp}^l & r_{ps}^l \\ r_{sp}^l & r_{ss}^l \end{pmatrix} \quad (5.8)$$

The off-diagonal components are proportional to magnetization and give rise to the light rotation. This rotation, known as the Kerr rotation, is proportional to the sample magnetization. The rotation is detected by use of a polarizer. Upon reflection, the light passes through a second polarizer. This second polarizer, having a longitudinal polarization, cancels the original and only the rotation due to the film magnetization remains.

The sample is situated between two electromagnetic coils and an applied external magnetic field cycles between negative and positive field. A diode detects the signal and data measurement software graphs the change in rotation as a function of applied field. From the measured hysteresis, film magnetization and coercivity are measured as discussed in Chapter 2. The magnetic field strength at the sample location was calibrated with a gaussmeter and was assumed to have remained constant for future measurements.

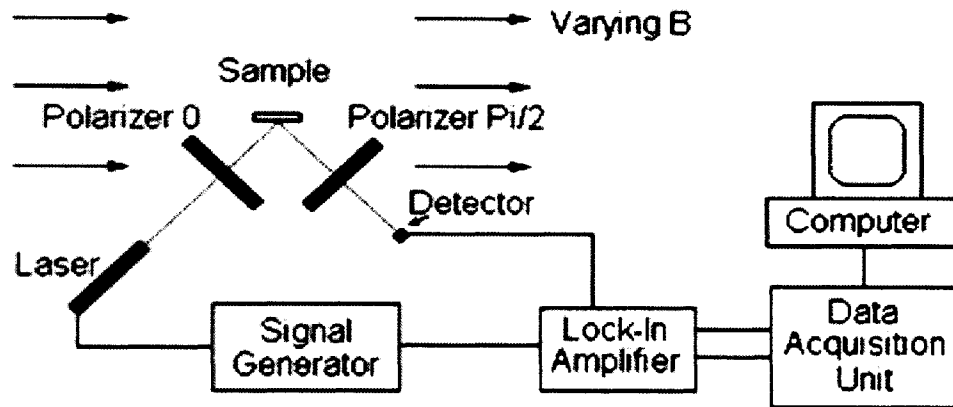


Figure 5.6: Schematic of MOKE experimental setup. A modulated photon beam is polarized and reflected off a thin film in an applied field. The magnetization rotates the incident beam and a detector measures the rotation due to the film magnetization.

The external field was applied by two electromagnets (GMW 3470 Electromagnet), driven by a Kepco BOP 50-4D bipolar power supply. A SRS DS345 signal generator modulated the laser and synchronized the signal to a SRS 810 DSP lock-in amplifier. This was the measurement system for the CIP films discussed in chapter 8.

Four-point Probe Method

Giant magnetoresistance is measured by the four-point probe method. A magnetic thin film is placed in applied external field. Four contacts are attached to the film surface. A low direct current, $I \leq 0.01\text{A}$, is applied to the film and the voltage is measured as the magnetic field cycles from negative to positive. The current must be minimized to reduce heating of the sample. The linear relationship between the applied current and measured voltage means that Ohm's Law applies:

$$R = \frac{V}{I} \quad (5.9)$$

The basic experimental design used a Keithley 2400 Sourcemeter to apply current (10 mA) through the sample via two of the four contacts. The voltage drop was measured by

a HP34401A multimeter through the remaining two contacts. The customized four-point contact was designed by Dimitar Vlassarev using POGO-25B-6 gold spring contacts.

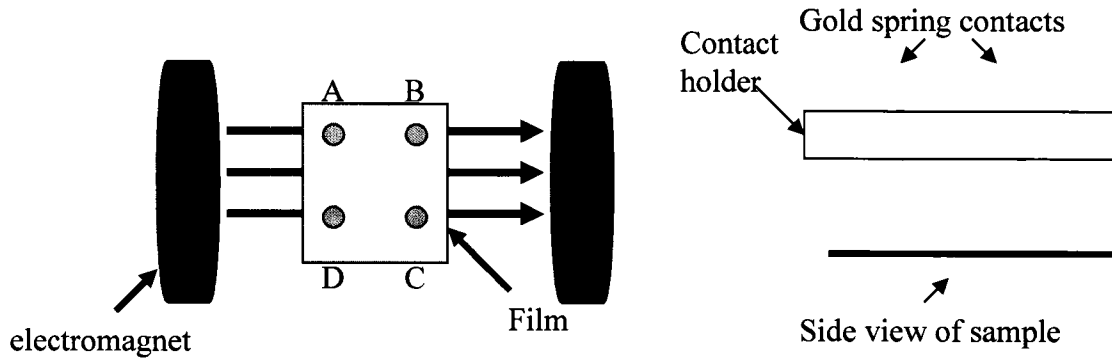


Figure 5.7: Illustration of four-point probe experimental setup. The film is situated between two electromagnetic coils and a field is applied. Current is applied through two contacts on the surface and voltage is measured through the other two contacts.

The resistance calculated represents the film resistance and resistance from the contacts attached to film surface. For the square CIP films, prepared at MSU and NIST, two measurements were made for each sample to calculate the resistivity using Labview program designed by Dimitar Vlassarev based on the van der Pauw method.⁷ In order to apply van der Pauw effectively, symmetrically shaped samples were used with small contacts. A homogeneous film thickness is assumed. Under these conditions, the resistivity is then given by:

$$\rho = \frac{\pi d}{\ln 2} \frac{(R_{AB,CD} + R_{BC,DA})}{2} f\left(\frac{R_{AB,CD}}{R_{BC,DA}}\right) \quad (5.10)$$

where the function ρ is the resistivity, d is the film thickness, $R_{AB,CD}$ is the resistance measured with the voltage drop along AB and the current flow along CD, and $R_{CD,AB}$ is

the resistance measured with the voltage drop along CD and the current flow along AB.

The function, f , is defined by:

$$\frac{(R_{AB,CD} - R_{BC,DA})}{(R_{AB,CD} + R_{BC,DA})} = f \operatorname{ar\,cosh} \theta \left(\frac{e^{\ln 2/f}}{2} \right) \quad (5.11)$$

In the case where $R_{AB,CD}$ and $R_{CD,AB}$ are nearly equal, a power series expansion of Equation 5.11 for f provides a good approximation for the van der Pauw measurements:

$$f \approx 1 - \left(\frac{R_{AB,CD} - R_{BC,DA}}{R_{AB,CD} + R_{BC,DA}} \right)^2 \frac{\ln 2}{2} - \left(\frac{R_{AB,CD} - R_{BC,DA}}{R_{AB,CD} + R_{BC,DA}} \right)^4 \left\{ \frac{(\ln 2)^2}{4} - \frac{(\ln 2)^3}{12} \right\} \quad (5.12)$$

This method measures just the resistivity of the film excluding contact resistance from the data.

In an attempt to minimize contact and lead resistance, gold contacts, which do not oxidize, and thin copper wires were used to construct the four-point probe. To insure accurate measurements, a firm contact between the film and the contacts was necessary. Typically, this was achieved by checking for drift during a measurement and adjusting the contacts until the drift was eliminated. It was determined by repeat measurements of GMR on an individual multilayer that the run-to-run error was less than 1%.

BH Looper

The BH Looper measures both changes in magnetic flux and magnetoresistance by monitoring the response of a sample to an applied alternating current (AC) magnetizing field. A hysteresis loop (B-H curve) is produced showing the response of the sample relative to the applied field. Current flowing through a drive coil(s) creates the AC field. A set of pickup coils are part of an assembly, called the pickup assembly, in which the sample under test is placed. Since the B field from the sample is much

smaller than the magnetizing field, the pickup assembly is designed to detect the field from the sample only. Typically, a single balance coil is situated along the axial centerline of the drive coils. The balance coil detects the magnetizing field from the drive coils but is not affected by the field from the sample. The signal from the balance coil is subtracted from the sample signal detected by the pickup coils. The correction is only first-order as the balance coil and pickup coils are not identical and positioned in different locations relative to the drive coil.

Initially, the thin films deposited in Chapter 7 were characterized using the BH Looper (SHB Instruments) located at the National Institute of Standards and Technology (NIST). The hysteresis and giant magnetoresistive curves are provided in real-time. When a film was measured more than once, it was apparent that a change in the location of the contacts on the film could produce a change in the measured GMR value of ~3%. This is due to an intrinsic difference within the film, such as roughness, which differs from location to location.

5.3 - References

- ¹ M. Ohring, *Materials Science of Thin Films: Deposition & Structure* (Academic Press, New York, 2002).
- ² A. T. Hubbard, *The Handbook of Surface Imaging and Visualization* (CRC Press, New York, 1995).
- ³ D. Rugar and P. Hansma, *Physics Today* **43**, 23 (1990).
- ⁴ D. Chescoe and P. J. Goodhew, *The Operation of Transmission and Scanning Electron Microscopes* (Oxford University Press, New York, 1990).
- ⁵ J. C. Gallop, *SQUIDS, the Josephson Effects, and Superconducting Electronics* (IOP Publishing Ltd, Philadelphia, 1991).
- ⁶ J. Woods, in *Electrical Engineering* (NC A&T, Greensboro, 2003), p. 49.
- ⁷ L. J. van der Pauw, *Philips Research Reports* **13**, 1 (1958).

Chapter 6 — GMR on Polymer Substrates

Traditionally, magnetic multilayers are deposited on semiconductor materials, such as silicon and GaAs.¹ These materials are engineered for high uniformity, smoothness, and conformality. As industrial and scientific needs change¹, deposition of GMR thin films on non-traditional substrates and buffers, such as polymers, may be required. The effect of these new materials on magnetic and electronic properties must be considered. Through a series of investigations, Parkin determined that magnetic multilayers could be deposited on non-traditional substrates, specifically polymeric substrates, without significant loss of GMR or other magnetic properties.² Subsequently, interest in polymeric substrates has grown as researchers explore the viability of GMR devices constructed with polymer components.²⁻⁴

The investigations described in this chapter examined single films and GMR thin films deposited onto polymer buffer layers for the purpose of inclusion into magnetic random access memory (MRAM) chips. A comparison was made between the interfacial roughnesses of the single films deposited on polymers as opposed to those grown on silicon oxide. Subsequently, a process was implemented to determine a PSV structure that yielded an optimum GMR value on a polymer. Finally, GMR thin films were deposited onto various polymer buffer layers and a comparison was made of the GMR values. It was determined that thin films deposited on polymer buffer layers had

roughness comparable to bare silicon wafers and that no loss of GMR occurs when the polymer buffer layer is used.

6.1 - Polymeric Substrates

Polymer buffer layers on silicon were supplied by the International Technology Center (ITC) located in North Carolina. The polymers had a form similar to polyimide, but the exact nature is proprietary information and cannot be reported in this thesis. They are identified only by reference numbers (e.g., “polymer 13” and “polymer 53”). Each polymer was spin-coated over 4” silicon oxide wafers with the intention to create as close to a 2-D surface as possible. It was found that depositing polymers with the spin-coater running at higher rotational speeds (rpm) produced thinner, more planar surfaces. However, since the material must also flow over small surface features present in the silicon wafer, there is a challenge to achieve as close to a 2-D surface as possible. This challenge of achieving "uniformity over topography" is an important step for device manufacturing. Therefore, ITC designed a procedure to characterize polymer planarization. The thickness uniformity over surface topography is measured by the degree of planarization (DOP) of the spin-on dielectric. The DOP was measured as shown in the following Figure 6.1.

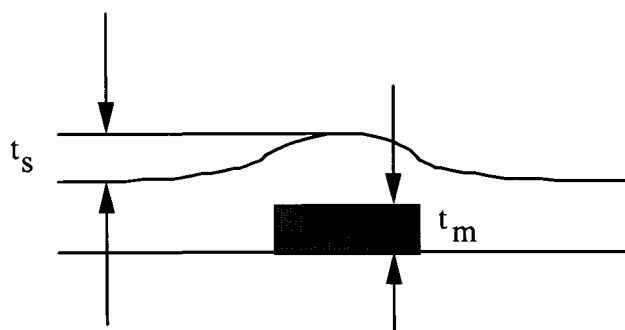


Figure 6.1: A schematic diagram used to illustrate the measurement for the thickness uniformity (DOP) of the polymer over topography.

As shown in Figure 6.1, the thickness of the topography is t_m and resultant change in thickness over the topography is t_s . The DOP is then given as a percentage from the following relation:

$$DOP = \left[1 - \frac{t_s}{t_m} \right] \times 100\%. \quad (6.1)$$

Planarization measurements were made using a test reticle that has various sized Al lines on the surface with intervening spacing ranging from 0.2 to 150 μm . The thicknesses were measured from cross-sectional SEM micrographs obtained using a Hitachi field emission SEM and by profilometry using a Tencor Alpha-Step. The stylus on the Alpha-Step had a 1.5 μm tip radius. One of the test wafers is shown in Figure 6.2. This test pattern was used for the polymer materials, which planarized very well. This pattern is a series of lines the length of the wafer surface. The line spacing is coarser and has intervening spacing of more than 500 μm on some features. ITC was able to determine which polymers planarized well over features by using tests patterns such as the one in Figure 6.2.

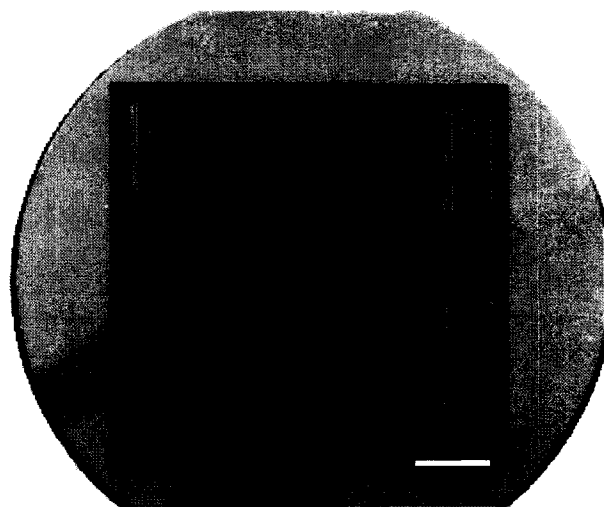


Figure 6.2: Photograph of the test pattern used for planarization measurements.

After testing the planarization of each material, ITC separately deposited two bare silicon 4" wafers with polymers 13 and 53, one of which was spin-coated at 3000 and the other at 5000 rpm. The wafers were then shipped to us pre-diced into ½" x ½" pieces. Each wafer was labeled according to polymeric material and rpm coating speed. For example, polymer 13 designates a specific polymer grown spin-coated at 3000 rpm onto a silicon oxide wafer. The polymers varied in thickness depending on coating speed and materials coated but were between 0.5 and 10 μm thick. The measure of planarization is proprietary information and the data is internal to ITC. For this thesis work, however, we were most concerned about the effect of the average surface roughness of the polymer, which we characterized independently.

6.2 - Roughness Studies

Initially, roughness measurements of niobium deposited on polymer substrates were compared with roughness values of niobium on oxide substrates by depositing single films onto each 12 x 12 mm substrate. The <100> silicon oxide wafers were provided by Silicon Quest. Single niobium (Nb) layers of thicknesses 10, 50, 100, and 150 Å were deposited onto substrates from two different polymers. Only the thickest and thinnest layers of Nb were deposited onto the oxide substrates for comparison. Topographical measurements from AFM scans allowed for comparison of root-mean-square (σ_{rms}) roughness, average roughness (Ra), and peak height (Z) for the polymer and silicon oxide substrates. Films were deposited at a rate of 0.6 Å/s in 4.0 mtorr of pure (99.999%) Ar. A base pressure of 6×10^{-9} torr was achieved after baking the main chamber. The main deposition chamber is capable of depositing onto six substrates under the same growth conditions at one time. Due to the number of samples, it was necessary

to deposit the films in several batches. An introduction chamber permitted the loading and unloading of films without breaking vacuum. To obtain the best vacuum possible, a turbo pump backed by a mechanical roughing pump was used to achieve a high vacuum within the introduction chamber. This was done to minimize the exposure of the main deposition chamber to contaminants from the introduction chamber. The main deposition chamber was evacuated post deposition and isolated from the introduction chamber before samples were unloaded and new samples loaded. Therefore, only the introduction chamber was directly exposed to ambient conditions. By this method, we were able to compare the effects of substrate on the Nb film roughness. AFM scans of the films deposited on the oxide substrate and polymer 13 showed smooth, flat surfaces. Most of the scans taken of films on polymer 15 were also smooth and flat but small granular features were observed on the surface of the 50 nm Nb film. Figure 6.3 shows AFM scans of the 10 nm Nb film grown on each substrate. Small grains are observed on the Figure 6.3c, causing the increase in roughness. However, the surface did not exhibit the larger features present on the 50 nm Nb film and can still be characterized as flat.

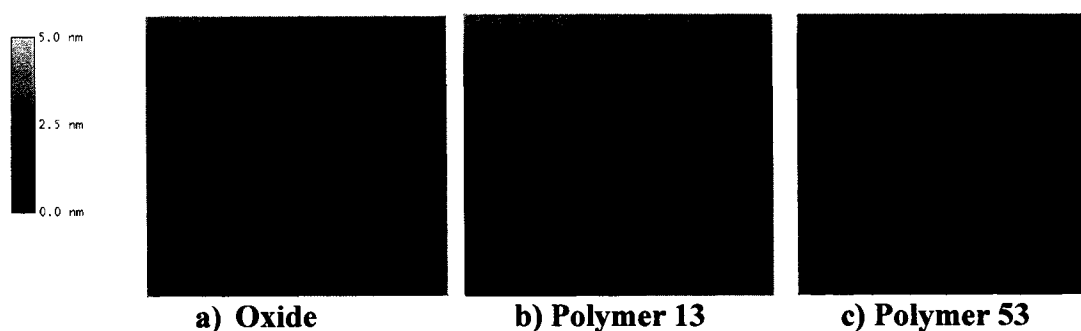


Figure 6.3: AFM scans of Nb 100Å on oxide substrate and polymer buffers show no significant change in feature size for films on the oxide compared to the polymers. Surface roughness measured from AFM scans was comparable for films on all three substrates. a) Oxide substrate b) Polymer 13 c) Polymer 53. AFM in Tapping Mode and scan size is 1 μm x 1 μm .

Table 6.1 compares the σ_{rms} , Ra, and Z for the single Nb films deposited on both polymers and oxide substrates. When comparing all three roughness parameters for films of the same thickness on different substrates, films grown on the polymers yielded lower σ_{rms} , Ra, and Z than films on the oxide substrate. The general trend for all three substrates was an increase in σ_{rms} , Ra, and Z with increased film thickness. This supports previous research in which Nb buffers cause an increase in film roughness⁵ suggesting an inherent roughness for a Nb layer that may increase with thickness. Significantly, the polymer roughness continued to be less than the oxide substrates. As the polymers tend to be hydrophilic, greater surface roughness, attributed to water contamination and diffusion of oxygen, might be expected as none of the polymers was baked prior to deposition. The data suggest that any contamination by water and oxygen had a negligible effect on surface roughness for the polymers.

Substrate	t_{Nb} (nm)	σ_{rms} (nm)	Ra (nm)	Z (nm)
Polymer 13	1	1.34 ± 0.58	1.06 ± 0.44	10.12 ± 3.2
	5	2.23 ± 0.82	1.80 ± 0.71	20.6 ± 11
	10	1.47 ± 1.0	1.18 ± 0.84	11.1 ± 5.4
	15	1.83 ± 0.77	1.47 ± 0.67	12.0 ± 4.0
Polymer 53	1	1.48 ± 0.43	1.20 ± 0.36	11.8 ± 2.8
	5	1.92 ± 0.60	1.47 ± 0.43	15.4 ± 4.1
	10	2.25 ± 1.8	1.65 ± 1.4	14.6 ± 6.8
	15	2.42 ± 1.9	2.07 ± 1.7	19.1 ± 3.8
Bare Oxide	1	2.56 ± 2.0	2.07 ± 1.7	23.1 ± 7.6
	15	3.09 ± 2.6	2.82 ± 1.7	20.0 ± 13

Table 6.1: Comparison of root-mean-square roughness, average roughness, and peak height for polymer and bare silicon oxide wafer substrates.

In general, this roughness study indicates that the roughness of the polymer buffer layers is comparable to the bare silicon wafer and we would not expect any detrimental effect to the GMR due to roughness of the polymer surfaces.

6.3 - GMR Optimization on Polymer Substrates

Our next goal was to produce optimized GMR multilayers on the polymer surfaces. We desired a maximum GMR response, but also wanted to select a multilayer that was relatively simple and would be able to withstand the processing steps (such as heating) necessary for the production of an MRAM device. We selected a pseudo-spin valve for this purpose, since it requires only two or three ferromagnetic layers and avoids the use of an antiferromagnetic layer and the exchange bias effect (which is sensitive to heating). The PSV had the form of Nb 30Å/Cu 50Å/NiFe X/Co 10Å/Cu 40Å/Co 40Å/Cu 20Å/Nb 20Å or Nb 30Å/Cu 50Å/NiFe 40Å /Co 10Å/Cu 40Å/Co X/Cu 20Å/Nb 20Å, where the thickness X was varied to optimize the GMR response. Samples were produced with NiFe and Co layers with X = 20, 30, 40, 50, 100, and 200 Å. Figure 6.4 shows the various layers of the PSV and summarizes the role of each layer in the optimization of the GMR. First, 30 Å of Nb and 50 Å of Cu were grown on the polymer to provide a good polycrystalline structure for the ferromagnetic layers to grow on. The ferromagnetic layers used are NiFe and Co, both with different coercivities. The Cu layer separates the two ferromagnetic layers to allow their magnetizations to switch independently. A thin layer (10 Å) of Co is inserted between the NiFe and Cu layer to prevent Cu atoms from diffusing into the NiFe and reducing the NiFe magnetization. Finally, top layers of Cu and Nb cap off the structure and prevent degradation by oxidation.

GMR multilayers were grown on different polymer surfaces as well as bare silicon oxide for comparison. Prior to loading, the silicon substrates were sonically cleaned with acetone followed by 2-propanol and dried with compressed (99.999%) N_2 . With the exception of one polymer, each polymer substrate was loaded as-prepared (without cleaning). One polymer substrate required an acetone bath for removal of a resist coating. A base pressure of 5×10^{-8} Torr was attained after a 12-hr bake of the main deposition chamber. During the deposition, each layer was deposited at a rate of 1.0 \AA/s in 2.4 mTorr of pure (99.999%) Ar, except for Nb, which was deposited at 0.8 \AA/s .

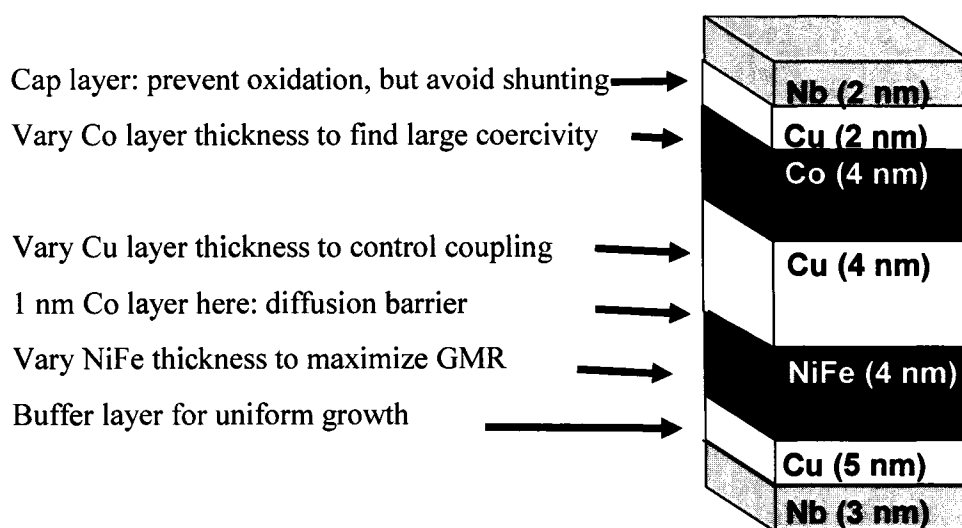


Figure 6.4: Structure of PSV used for this study, with summary of purpose for each layer.

The GMR effect is a very sensitive function of the thicknesses of the various layers and the mechanism of the thickness dependence is fairly well known.⁶ For example, for small Cu thicknesses, the two ferromagnetic layers become strongly magnetically coupled by the RKKY interaction and pinhole coupling. For the PSV, it is

desired that the two ferromagnetic layers be uncoupled and have very different coercivities. Therefore, a thick Cu layer is needed. However, as the Cu thickness increases, the GMR will decrease because the current will be shunted through mainly the low resistivity Cu layer rather than through the higher resistivity ferromagnetic layers. This shunting effect is phenomenologically described by the following equation:

$$\frac{\Delta R}{R} = \left(\frac{\Delta R}{R} \right)_0 \frac{e^{-t_{NM}/l_{NM}}}{1 + t_{NM}/t_0} \quad (6.2)$$

where t_{NM} is the Cu layer thickness and l_{NM} is related to the mean free path in the Cu (it is estimated that $l_{NM} \sim 1/2\lambda$, where λ is the mean free path). Figure 6.5 shows data for three Cu thicknesses used as well as a plot of Equation 6.2.

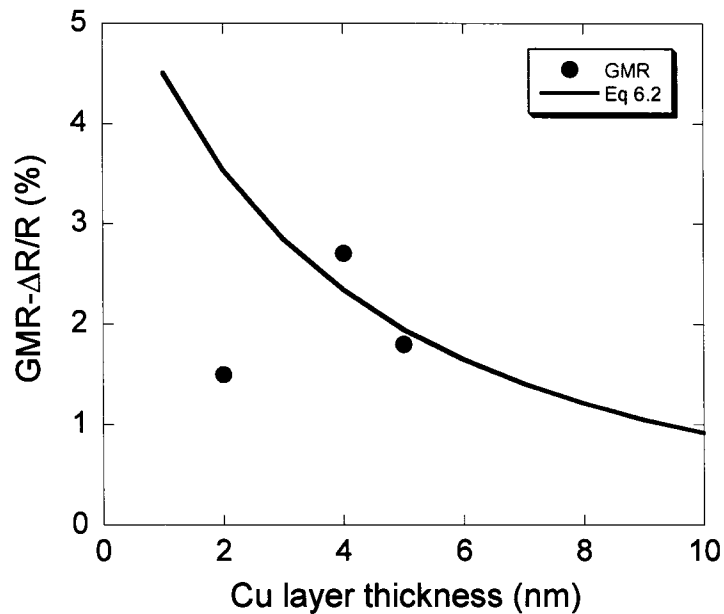


Figure 6.5: GMR for PSV on polymer 13 for three different Cu thicknesses (dots). The Co and NiFe layers were each fixed at 40Å. Solid line is from Equation 6.2 in text, assuming a $\lambda \sim 32$ nm for Cu. For Cu thicknesses of 4 and 5 nm, theory and experiment do not differ significantly. For thinner Cu thicknesses, Eq 6.2 does not account for a substantial increase in ferromagnetic coupling. Strong ferromagnetic coupling prevents the film from achieving a well-defined AP state that is necessary to obtain large GMR values.

Similarly, the GMR will have an optimal value for a particular ferromagnetic layer thickness. The ferromagnetic layer thickness determines the amount of spin-dependent scattering as well as controls the coercivity (for the Co) and magnetic coupling between layers. A phenomenological equation similar to Equation 6.2 has also been used by others to describe the dependence of GMR on ferromagnetic layer thickness⁶:

$$\frac{\Delta R}{R} = \left(\frac{\Delta R}{R} \right)_0 \frac{1 - e^{-t_F/l_F}}{1 + t_F/t_0} \quad (6.3)$$

From Equation 6.3, we see that very thin ferromagnetic layer thicknesses, GMR is correspondingly small due to a decrease in spin-dependent scattering. However, for very thick ferromagnetic layers, again the GMR is small because of current shunting.

Figure 6.6 shows the GMR values as a function of Co layer thickness. In this figure, it can be seen that the GMR does not continue to increase with increasing Co thickness. One of the reasons why is, as mentioned above, the shunting effect. Another reason is that the thicker Co layers exert significantly stronger coupling to the NiFe layers due to the stronger magnetization of the thicker Co layers.

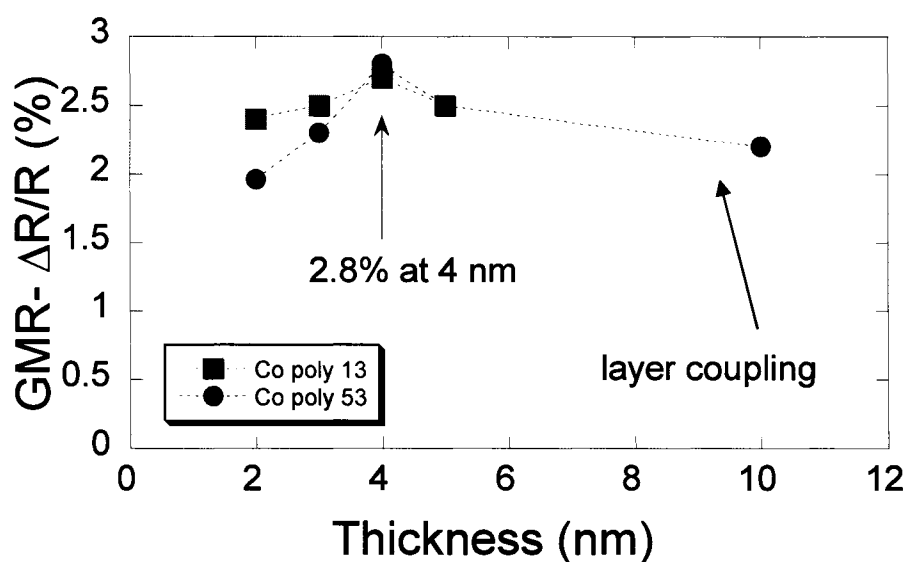


Figure 6.6: GMR for PSV on polymer 13 (red, closed squares) and 53 (blue, closed circles) for different Co thicknesses. The Cu and NiFe layers were fixed at 4 nm and 4 nm respectively. The maximum GMR was obtained at a Co thickness of 4 nm for films on both polymer buffers. The decrease in GMR occurs as the increasing Co thickness results in increased ferromagnetic layer coupling. The coupling limits the films ability to achieve a well-defined AP state. Dotted lines are to guide the eye.

The effect of magnetic coupling between the two ferromagnetic layers can be seen in the hysteresis loops of the PSV, shown in Figure 6.7 for varying Co, NiFe and Cu thicknesses. The data were taken using SQUID magnetometry by Jamil Woods at North Carolina A&T University. Again, in an ideal PSV, the two ferromagnetic layers should switch their magnetizations separately in a changing applied magnetic field. The NiFe should have a small coercivity and switch first and the Co should have a larger coercivity and switch later. Evidence of independent switching is the appearance of two loops and a “shelf” in the hysteresis. The “shelf” indicates the achievement of an antiparallel state.

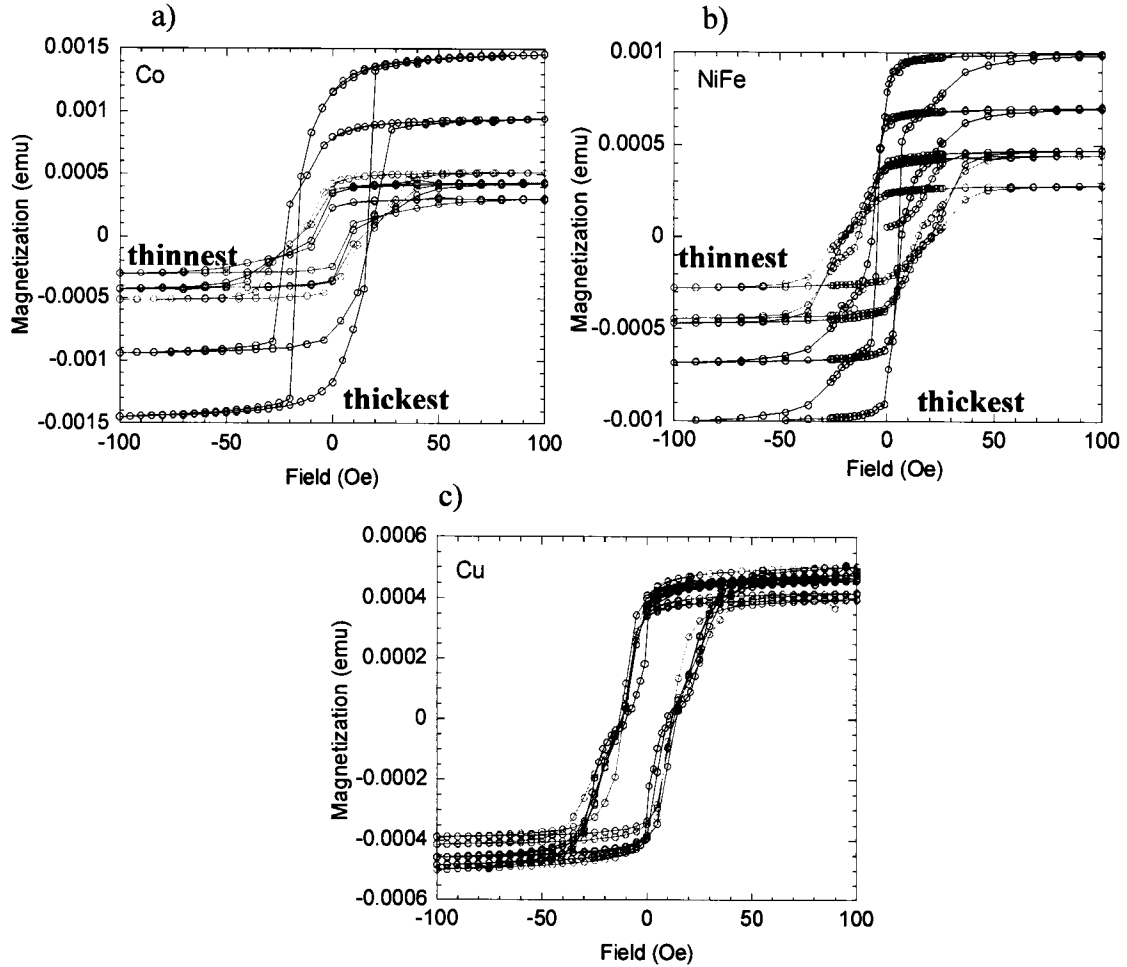


Figure 6.7: Hysteresis curves for the optimization of a PSV on a polymer substrate. a) Increasing Co layer thickness b) Increasing NiFe thickness c) Increasing Cu thickness. For Co (a) and NiFe (b), the magnetization increases with increasing thickness. For the Cu layer (c), the thinnest layer is red and the thickest is black. Notice the two loops emerging for the thickest Cu layer.

First, in Figure 6.7a), the dependence on Co thickness is shown. For small Co thicknesses, the two independent loops and shelves are seen, but for thicker Co, only one loop of decreased width is observed. The width of the loops, an indication of the Co coercivity, increases with Co thickness except for the 200 Å film, where it decreases. This indicates that the Co and NiFe layers are becoming coupled and switching together for higher Co thicknesses. This correlates with the decrease seen in GMR.

Figure 6.7b shows the hysteresis curves for films with various NiFe thicknesses. In contrast to Figure 6.7a, the width of the curves decreases with increasing NiFe thickness but the height increases similar to the films with varying Co thicknesses. However, the magnetization for the varying NiFe films is smaller than those for the Co films. As the NiFe becomes the dominant film in the structure, the independent loops in the hysteresis loops become clear. Although some de-coupling is evident, layer switching occurs at a much lower field than when the Co film dominates the structure. Lastly, Figure 6.4c displays hysteresis curves for films with varying interspacer thicknesses. When the interspacer layer is thin, no independent switching of one layer from the other is evident. As the layer thickness increases, the F layers begin to de-couple as observed in the hysteresis curves. One F layer clearly switches at a lower field followed by the other at a higher field. Notice, for the films with no de-coupling, the coercivity lies between the switching fields for the de-coupled films further indicating simultaneous switching in films with a thin interspacer layer.

Combining the results from the above discussion, it was determined that the optimum thicknesses were NiFe 40Å/Cu 40Å/Co 40Å or NiFe 50Å/Cu 40Å/Co 50Å. The optimized structure chosen for the MRAM project was a Nb 30Å/Cu 30Å/NiFe 40Å/Co 10Å/Cu 40Å/Co 40Å/Cu 20Å/Nb 20Å pseudo-spin valve. The hysteresis for this PSV is shown in Figure 6.8. Although the F layers are not completely de-coupled, there was sufficient switching between the parallel and antiparallel states for the initial experimentation of this project.

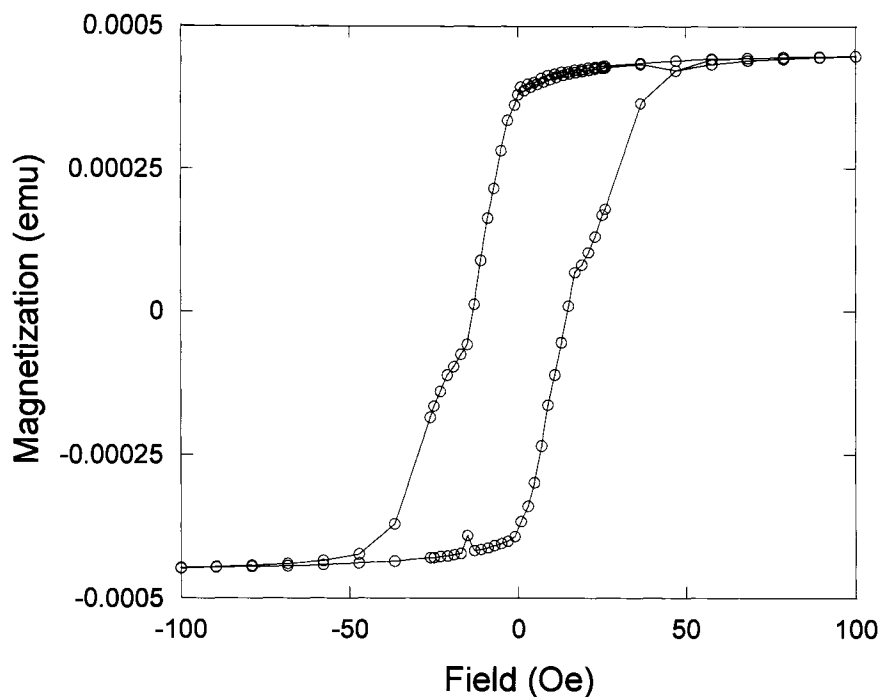


Figure 6.8: Optimized PSV chosen for MRAM project. This PSV provides adequate switching between parallel and antiparallel states, though the F layers are not completely de-coupled from each other.

After optimization, GMR values up to 3.2 % were measured on the various polymer substrates and found to be comparable to the same PSV on an oxide substrate. Magnetizations were unchanged whether the multilayers were deposited on silicon oxide or polymer substrates suggesting that any of these substrates are adequate for this application. The GMR responses for the PSV on an oxide and a polymer substrate are shown in Figure 6.9. Both GMR curves are similar in shape and size displaying no significant difference due to the substrate material. Further, the response of the PSV occurs within 20 Gauss indicating a fast switching rate between a parallel and antiparallel state.

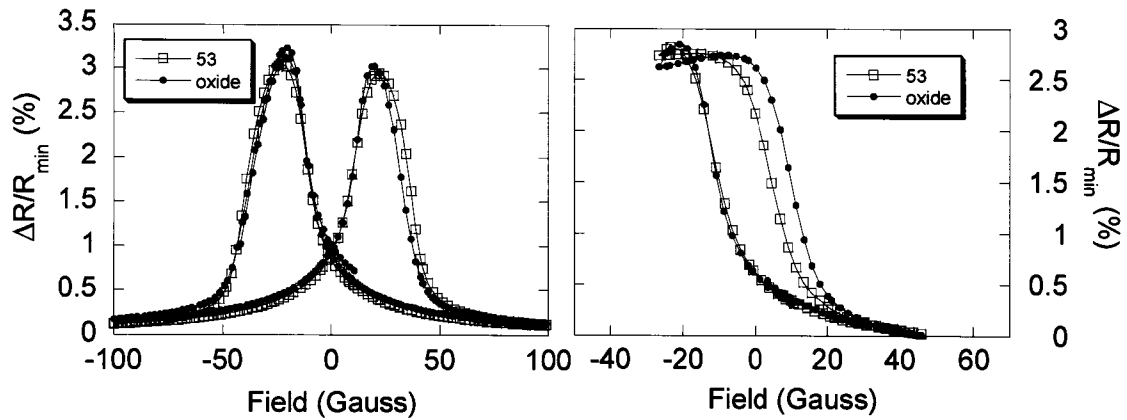


Figure 6.9 GMR response for a pseudo spin valve deposited on silicon oxide (closed circles) and polymer 53 (open squares). Left: Total switching behavior. Right: spin valve response.

In fact, both the GMR and magnetic response were similar on a variety of polymer substrates, listed in Table 6.2, displaying flexibility in the buffer layer chosen for this project. This can be explained by the small σ_{rms} roughness of the films on the polymer substrates, which was typically < 2.5 nm and comparative to the film roughness on an oxide substrate. Initial annealing experiments on the pseudo spin valves have found that the GMR does not decrease under annealing for one-half hour at 150°C

Substrate	GMR (%)
Polymer 53	2.9
Polymer BCB	3.1
Polymer 23	3.1
Polymer 43	3.2
Oxide	3.1

Table 6.2: A list of the GMR measured for the same PSV grown on various substrates.

6.4 - Conclusion

In this investigation, a series of films were deposited to optimize a specific PSV maximizing GMR. The optimal ferromagnetic and nonmagnetic layer thicknesses were

determined and a series of GMR pseudo-spin valves were deposited onto polymer buffer layers and as a reference, an oxide buffer. Effects of buffer layer material on both the GMR and magnetic behavior of the thin films were studied. No significant difference between the films on the polymers when compared to the film on the oxide was found. The response and GMR of films on several different polymers were consistent with the response and GMR on the oxide. The implications are important for future work on these types of polymers. The deposition of GMR structures on polymeric materials is a viable alternative to traditional materials for further development of MRAM technology.

6.5 - References

- ¹ J. De Boeck, W. Van Roy, J. Das, et al., *Semicond. Sci. Technol.* **17**, 342 (2002).
- ² S. S. P. Parkin, *Appl. Phys. Lett.* **69**, 3092 (1996).
- ³ M. Wohlgenannt, T. L. Francis, O. Mermer, et al., in *INTERMAG Asia 2005: Digest of the IEEE International Magnetism Conference*, New Jersey, 2005), p. 1257.
- ⁴ Z. G. Yu, M. A. Berding, and S. Krishnamurthy, *Phys. Rev. B* **71**, 60408 (2005).
- ⁵ M. C. Cyrille, S. Kim, M. E. Gomez, et al., *Phys. Rev. B* **62**, 3361 (2000).
- ⁶ U. Hartmann, *Magnetic Multilayers and Giant Magnetoresistance: Fundamentals and Industrial Applications* (Springer Verlag, 2000).

Chapter 7 — Etched Substrate Study

Past studies have shown that interfacial roughness affects the electronic transport and magnetic properties of multilayer thin films. In the current-in-plane geometry, increasing interfacial roughness can either lead to an increase in giant magnetoresistance (GMR) through enhanced interfacial and spin-dependent scattering¹, or to a decrease in GMR due to increased magnetic coupling². Recent work has explored the effects of long length scale roughness on GMR³, and modeling has shown that such roughness may cause the GMR to increase⁴, decrease, or have no effect. These changes depend on several parameters including the roughness amplitude, period and the electron mean free path⁵. Most of the studies carried out have used a change in growth parameters (such as sputtering pressure) or annealing to change the roughness¹, with root-mean-square (σ_{rms}) roughness values below 5 nm. There has been little work, however, exploring the effect of large scale roughness, such as introduced through a substrate, on GMR. There are important implications for applications in which GMR multilayers are deposited on non-standard substrates and buffer layers such as flexible media.⁶ In this chapter, two separate but connected studies are described, followed by a discussion of the results for both studies.

This chapter presents two controlled roughness studies conducted on etched glass substrates. The first study was conducted by the College of William & Mary. Results from this study led to a second more detailed investigation carried out at the National

Institute of Standards and Technology (NIST) with the collaboration of on-site researchers. Both studies explored the effects of very large-scale roughness ($\sigma_{\text{rms}} > 5 \text{ nm}$) on the properties of giant magnetoresistive multilayers in which a somewhat controllable but non-uniform amount of roughness was introduced through the substrate. For the initial study, a pseudo-spin valve (PSV) was chosen for its simple structure and its optimal GMR value determined in a previous experiment. In the second study, more PSV samples were grown, as well as exchange-biased spin valves (EBSV) which were used in an attempt to separate the effects of magnetic coupling.

7.1 - PSV study at William & Mary

The first study used 12 mm square glass slides comprised of amorphous boroaluminosilicate (Corning 1737f) with a 1.1 mm thickness, provided by Precision Glass & Optics. Roughness was produced by chemically etching the glass using a paste consisting of ammonium, sodium bifluoride, and <1% hydrofluoric acid. The etchant was applied to one side of the slide and left on for a specific time. After etching, each slide was then rinsed with water to remove the etchant, and then blown dry. Four etchant times were selected: 30s, 60s, 150s, and 300s. The glass substrates were chemically etched for different lengths of time to produce a range of lateral and vertical roughness, and then GMR multilayers were deposited on them by dc magnetron sputtering. Immediately following the etching process, the slides were loaded into the introduction chamber, which was pumped down to $\sim 1 \times 10^{-5}$ torr, with a base pressure of 1×10^{-8} torr in the main deposition chamber. The introduction chamber was opened to the deposition chamber and the pressure pumped down to $\sim 4 \times 10^{-8}$ torr before introducing ultra high purity (99.999%) argon to the system to achieve a pressure of 2.8 mTorr. The Cu, Co,

and $\text{Ni}_{81}\text{Fe}_{19}$ targets had 99.95% purity while the Cu target was 99.99% pure. The GMR multilayer studied was a pseudo spin valve of the form 30\AA Nb/ 50\AA Cu/ 40\AA $\text{Ni}_{81}\text{Fe}_{19}$ / 10\AA Co/ 40\AA Cu/ 40\AA Co/ 20\AA Cu/ 20\AA Nb. Each layer was deposited at a rate of 1.0 \AA/s . As a reference sample, the same GMR spin valve was deposited onto an unetched glass slide of the same type as the etched slides. All five samples, including the unetched slide, were produced in the same deposition run to insure the same vacuum conditions. AFM measurements, post deposition, confirmed that roughnesses with lateral wavelengths up to $\sim 500\text{ nm}$ and σ_{rms} amplitudes of up to $\sim 25\text{ nm}$ were produced.

The Magneto-Optical Kerr Effect (MOKE) was used to measure the magnetization of the films and record hysteresis curves. The GMR was measured by the four-point probe method, with a constant current source and voltage measurements provided by a multimeter. The MOKE curves and GMR were measured simultaneously with the samples mounted between the poles of an electromagnet. Film roughness was characterized by atomic force microscopy (AFM - Digital Instruments Nanoscope IV).

AFM measurements show an increase in σ_{rms} roughness of the films with increased etching time. Figure 7.1 shows AFM scans for two of the etched substrates. The general trend is that with increasing etch time, the substrates and films obtain larger peak roughness, larger σ_{rms} roughness, and larger lateral dimensions for the roughness. The AFM scan on the left has smaller peaks with an average peak height of 4 nm . The scan on the right has fewer individual peaks and instead has several large peaks with an average peak height of 36 nm . Comparing all of the films, we observe a general increase in peak height. The anomaly is the etch time with the film deposited onto the substrate etched for 30s which has the lowest value and is discussed below. The wavelength of the

roughness, estimated from the AFM scans, also shows a general increase from ~ 76 nm to ~ 271 nm.

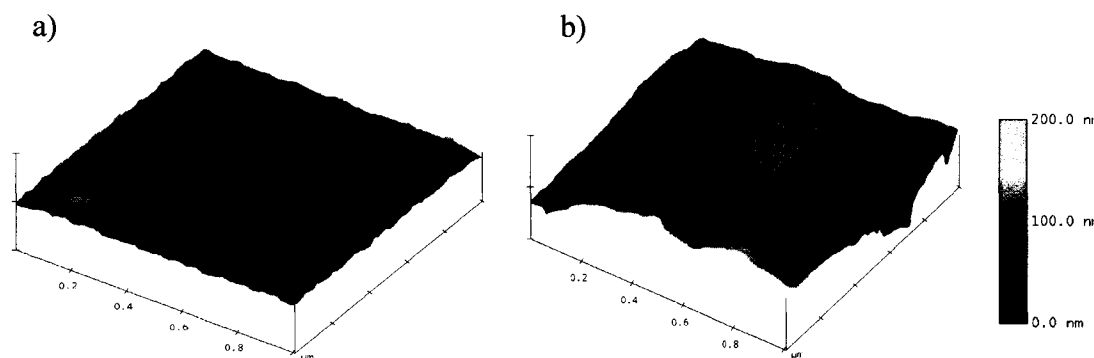


Figure 7.1: AFM scans showing film surface roughness. (a) 30s etch. Vertical scale is 50 nm. (b) 300s etch. Vertical scale is 200 nm. Lateral scale for both is $1 \mu\text{m} \times 1 \mu\text{m}$. Scans show an increase in roughness feature length and height with increasing etch time. Scan (a) has small granular shaped features while (b) has larger features with a sinusoidal shape. AFM was in tapping mode.

Table 7.1 shows the etch times for the glass substrates, the σ_{rms} roughness of the deposited films, the resistance and GMR ($\Delta R/R$) values as well as the width of the hysteresis curves (coercivity) taken from MOKE. As can be seen in the table, there is an initial decrease in the σ_{rms} roughness and GMR for the glass slide etched for 30s. The initial etch resulted in a slight smoothing of the glass surface that may be attributed the etching away of existing surface roughness. This is followed by an increase in the GMR with each of the next three increases in etching time. The slide etched for the longest amount of time shows a decrease in the giant magnetoresistance value below the unetched sample. The GMR somewhat parallels the change in peak-to-peak lengths increasing as the peak-to-peak increases. For the last sample, the GMR decreases as λ continues to increase.

Etch time (s)	σ_{rms} (nm)	λ (nm)	$\Delta R/R$ (%)	R(Ω)	H _c (Oe)
0	8.15 ± 2.6	124 ± 44	3.28	6.45	26.17
30	4.26 ± 0.7	76 ± 18	2.90	5.78	22.05
60	11.45 ± 11.4	139 ± 71	3.36	6.15	30.08
150*	17.3 ± 22	165 ± 99	3.39	5.06	30.33
300	36.2 ± 5.8	271 ± 92	3.16	6.05	30.88

Table 7.1: Table of data for average (σ_{rms}) roughness of films (measured by AFM), average peak-to-peak (λ) lengths, GMR, resistances, and coercivities for films deposited on substrates etched for different durations. (*) Clean AFM scans for this film were not obtained; large error due in part to streaks in scans.

Figure 7.2 shows the GMR ($\Delta R/R$) curves of samples; one on unetched glass, and one etched for 150s. For the 150s sample, the GMR is seen to slightly increase and the curve is seen to also slightly broaden. This broadening is also seen in the magnetization curves taken by MOKE, also shown in Figure 7.2. For the sample etched for 30s, however, the GMR curve and coercivity both decrease compared to the unetched sample (curves not shown).

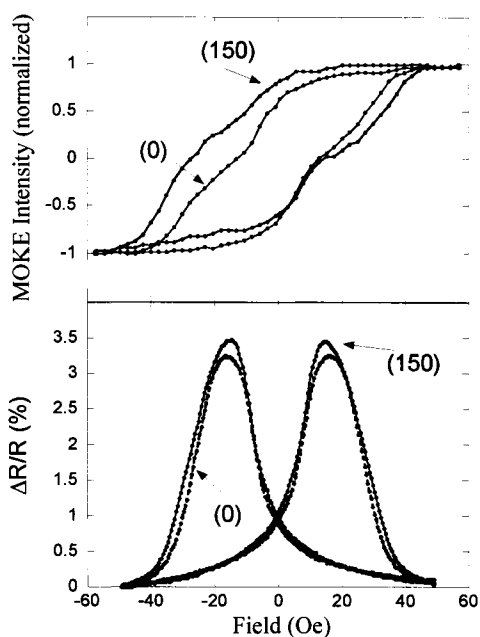


Figure 7.2: MOKE intensity (top) and GMR curves for spin valves on an unetched glass substrate (0) and a substrate etched for 150 s (150). Notice the increase in GMR as well as the slight broadening of the curves.

Both the coercivity of the C_0 (which determines the width of MOKE and GMR hysteresis loops) and the GMR change slightly as a function of substrate etch time and roughness. Figure 7.3 shows the dependence of the coercivity and GMR on the amplitude of the roughness. As the σ_{rms} roughness increases, we observe an increase in GMR, which reaches a maximum value and then decreases. A similar trend in coercivity is also seen, although the coercivity levels off with higher roughness.

Figure 7.3 may indicate a relationship between increasing coercivity and GMR. This increase in coercivity could indicate a decreased coupling between the magnetic layers in the spin valve, leading to greater GMR, since the coupling of the layers hinders the achievement of the anti-parallel magnetic alignment. The increase in coercivity can also be related to the increased roughness since large amounts of lateral roughness can

hinder domain realignment since the walls are forced to shift around these areas. Eventually, the roughness becomes detrimental to the GMR, probably as intermixing at the interfaces between nonmagnetic and ferromagnetic layers becomes too great.

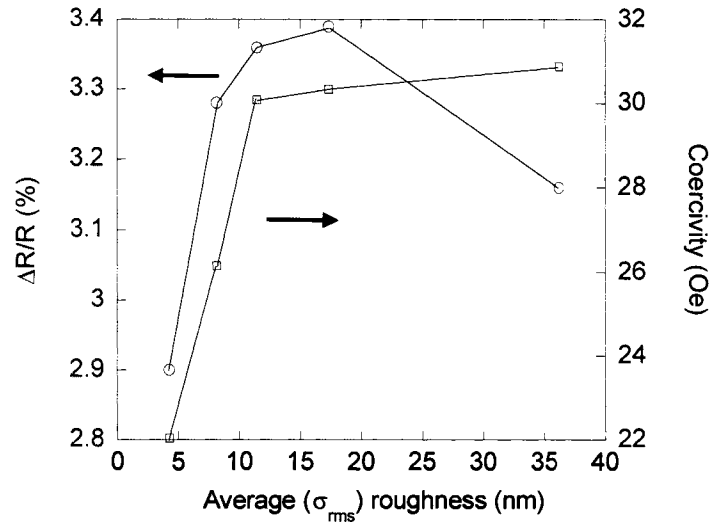


Figure 7.3: Giant magnetoresistance ($\Delta R/R$, red, open circles) and coercivity (blue, open squares) as a function of film σ_{rms} roughness. Initially, both $\Delta R/R$ and coercivity increase steeply for the first few data points followed by less steep increases in both with increasing roughness. Finally, $\Delta R/R$ decreases and the coercivity plateaus. The initial increase suggests a decrease in ferromagnetic coupling achieving a more defined AP state. The benefit to GMR is lost as the roughness becomes detrimental, probably due to intermixing at the F/N interfaces. Lines are a guide to the eye.

Initially, it is surprising that such large roughness does not have more of a detrimental effect on the GMR. The maximum decrease in GMR, compared to an unetched substrate, was 11% and occurred for the sample etched only for 30s. The samples etched for more than 60s had a roughness easily visible to the eye, and yet the GMR curve was only slightly modified from that of the unetched substrate. The effect of the substrate, and hence interfacial roughness, on the GMR of the spin valves can be due to several mechanisms. Past studies of fine-scale roughness^{5,7} ($\sigma_{rms} < 5$ nm) have shown that increased interfacial roughness can increase GMR due to increased interface scattering (for the case of CIP) and increased spin-dependent scattering (for the case of

CPP). In our case, the roughness could be increasing the GMR through an increase in interface scattering, with the effect lessened for the longer wavelength roughness. The increase in coercivity also seems to be playing a role. This could indicate a decrease in interlayer coupling, which is detrimental to the GMR. Unfortunately, the magnetic coupling is difficult to control in PSV. This led to a more comprehensive study at the National Institute of Standards and Technology (NIST), with the inclusion of exchange-biased spin valves to lessen the effects of magnetic coupling.

7.2 - PSV and EBSV Study at NIST

The second study expanded on the initial W&M study by increasing the sample number and depositing one set of EBSV. Twenty-seven substrates were prepared: eighteen diced 4 x 12 mm and nine, 12 x 12 mm. Each was sonically cleaned with acetone followed by 2-propanol and blown dry with ultra high purity (99.999%) N₂. Three substrates were left unetched. Each of the remaining twenty-four slides was etched with the same paste described above. The substrates were divided into three groups: 12 x 12 mm and two groups of nine 4 x 12 mm. The above pseudo-spin valve was deposited on one group of 4 x 12 mm and the 12 x 12 mm substrates at an argon pressure of 3×10^{-5} torr after reaching a base pressure of 5×10^{-10} torr. An exchange-biased spin valve (EBSV) was deposited onto the second group of 4 x 12 mm substrates. The EBSV chosen, 30Å Nb/50Å Cu/40Å Ni₈₁Fe₁₉/10Å Co/40Å Cu/40Å Co/100Å Ir₅₀Mn₅₀/20Å Nb, used IrMn due to its strong pinning properties. The substrates were loaded, nine per run, into an introduction chamber. After evacuating the introduction chamber, the substrates were introduced into the deposition chamber. Each substrate was sputter cleaned with argon at 100eV for 10 seconds to remove hydrocarbons without significantly changing

the roughness. The metals were deposited with the following parameters: Nb at 0.86 Å/s, Cu at 0.66 Å/s, NiFe at 0.25 Å/s, Co at 0.27 Å/s, and IrMn at 0.66 Å/s.

A BH looper (ShbWin) was used to measure GMR, saturation magnetization, and coercivity. Film roughness was characterized by atomic force microscopy (AFM - Digital Instruments Nanoscope IV). Comparison to an unetched 12 x 12 mm substrate could not be made since the substrate fell off during deposition and was lost inside the deposition chamber.

It was found that the PSV were highly susceptible to minor changes in substrate parameters and the magnetic data varied in what appeared to be a highly random pattern with GMR and coercivity values varying significantly from film to film. It was difficult to discern if a correlation to roughness existed from these films. The EBSV films exhibited more consistency as well as larger GMR values attributed to the exchange-biasing of one ferromagnetic layer resulting in smaller dependence on interlayer magnetic coupling. This allowed for a better determination of substrate roughness effects on the electronic mechanisms of GMR.

For all twenty-seven samples, AFM measurements show an increase in σ_{rms} roughness of the films with increased etching time with values among the three data sets ranging from ~2 to 94 nm but comparable from group to group. Figure 7.4 shows AFM scans for two of the etched substrates. The general trend is that the substrates and films obtain larger peak roughness, larger σ_{rms} roughness, and larger lateral dimensions for the roughness. Figure 7.4a has small features with an average peak height of 43.3 nm. Figure 7.4b has an increased number of individual granular features as well as larger feature sizes with an average peak height of 314.6 nm.

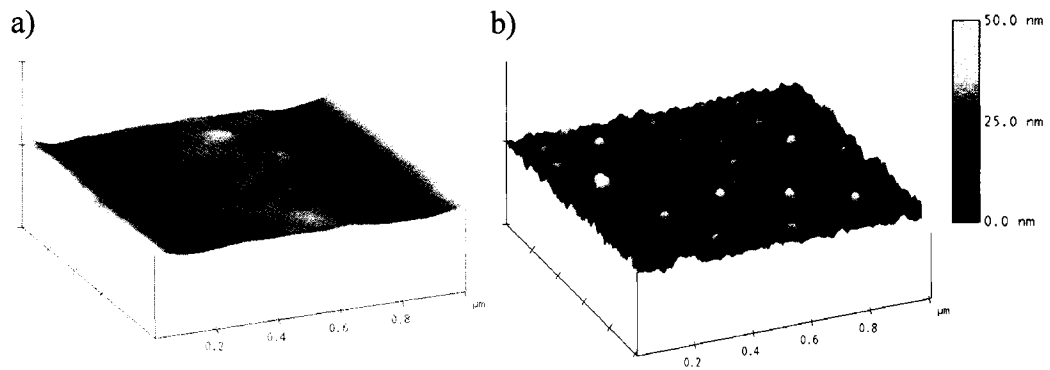


Figure 7.4: AFM scans showing surface roughness for EBSV substrates. a) unetched. b) 150s etch. Vertical scale is 50 nm for both. Lateral scale for both is $1\ \mu\text{m} \times 1\ \mu\text{m}$. Scans show increase in surface roughness with etch time. Scan (a) shows virtually no surface features while (b) has a large number of granular features on the surface. AFM was in tapping mode.

Comparing all of the films, we observe a general increase in average peak height and average roughness with etch time. σ_{rms} roughness ranged from ~ 2 to 87 nm for the substrates post-etching and pre-deposition, shown in Table 7.2. The roughness parameters given are averages of at least 3 different scans taken on each sample, with a total of ~ 100 scans. The error is the standard deviation of these measurements, which for some samples can be quite large. The large standard deviations may be due to two roughness scales. There appeared to be both large and small grains on the glass surface. As etch time increased, the large features increased in size and number over the substrate surface. Several of the substrates show a decrease in roughness when compared to the glass substrate immediately preceding. Generally, the trend is an increase in root-mean-square roughness, average roughness, and peak height with continued etching.

Etch Time (s)	σ_{rms} (nm)	Ra (nm)	Z (nm)	λ (nm)
0	2.3 ± 1.1	1.5 ± 0.5	43.3 ± 24.7	0
30	9.4 ± 6.4	5.1 ± 2.0	173.7 ± 149.5	1758 ± 497
60	15.8 ± 10.3	7.7 ± 4.8	286.8 ± 149.5	5166 ± 1909
90	9.9 ± 6.2	4.0 ± 2.1	200.1 ± 162.1	3242 ± 444
120	17.0 ± 10.6	10.7 ± 5.8	251.3 ± 25.1	1473 ± 279
150	22.7 ± 9.1	10.2 ± 3.6	314.6 ± 97.4	2565 ± 1864
210	86.9 ± 47.9	35.6 ± 28.1	1160 ± 581.5	1934 ± 660
240	74.3 ± 32.3	26.3 ± 18.4	1222 ± 252.7	4687 ± 1964

Table 7.2: List of average roughness measurements for etched and unetched 4x12 mm glass substrates pre-deposition. An EBSV was grown on these substrates.

The data for the PSV study is summarized in Table 7.3. There is a similar increase in σ_{rms} with etch time. It was found that the GMR values varied widely from sample to sample, as well as the coercivity. This is believed to be due to a high degree of sensitivity of the magnetic coupling on growth conditions. We note that in Table 7.3, the highest GMR occurs for samples with highest coercivity (H_c). Figure 7.5 shows hysteresis loops for two PSVs and the effect of magnetic coupling.

Etch time (s)	σ_{rms} (nm)	λ (nm)	$\Delta R/R$ (%)	H_c (Oe)
0	6.8 ± 3.6	0	1.86	15.99
30	14.4 ± 5.1	2988 ± 2088	0.74	13.83
60	8.9 ± 6.7	1042 ± 671	4.49	68.54
90	16.4 ± 12.4	1311 ± 678	1.08	16.50
120	17.8 ± 7.1	1604 ± 945	0.66	13.13
150	34.6 ± 11.9	1358 ± 537	1.11	21.04
180	48.3 ± 27.9	2861 ± 1968	0.73	21.41
210	56.9 ± 20.9	3951 ± 1202	0.75	12.82
240	61.1 ± 49.4	1572 ± 1542	4.52	75.33

Table 7.3: Comparison of average root-mean-square (σ_{rms}) roughness of glass pre-deposition (measured by AFM) and average feature peak-to-peak length (λ) with GMR, film resistance and coercivity measurements of 4x12 mm PSV films.

The amount of giant magnetoresistance is very sensitive on the degree of the antiparallel alignment, which in turn is a very sensitive function of roughness and also grain properties affected by growth conditions. As discussed in Chapter 3, the changes in deposition parameters affect the growth of grains and grain boundaries. These changes affect the magnetic and electronic properties of the deposited thin film. The data taken from the PSV represent changes in crystallinity due to interfacial roughness and variances in growth conditions that occur as a result of the normal deposition process. The number of samples was greater than the capacity of the deposition chamber. As discussed in Chapter 6, the necessity of loading samples into the system in batches introduces variances in growth conditions (water, oxygen, pressure changes) which can produce films of slightly different properties. For example, changes in the partial pressure of oxygen present in the chamber will have a significant effect on thin film properties.^{2, 8} Small changes in sputtering pressure, vacuum impurities, and contaminants adsorbed onto the chamber wall can all play a role in film impurity and as a result, film magnetic and electronic properties.

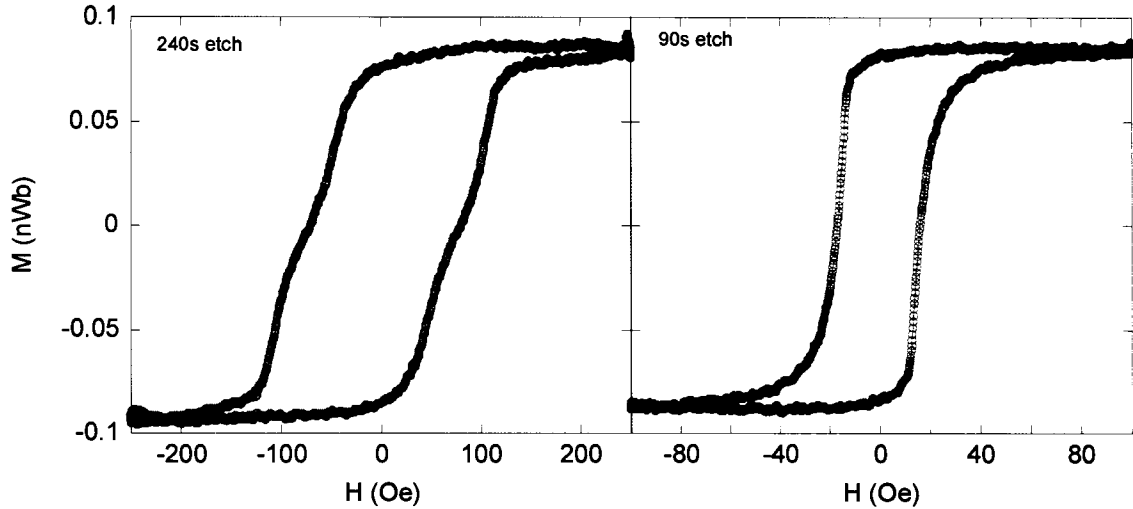


Figure 7.5: Comparison of hysteresis curves for two films; one with high GMR of 4.52% (left) and low GMR of 1.08% (right). The curve on the left has a slight plateau while the curve on the right has no apparent plateau, suggesting that the ferromagnetic layers are strongly coupled.

To further characterize the PSV films, van der Pauw 4-point probe measurements were made on the 12x12 mm films (the 4x12 mm films were asymmetric and we were not able to use the van der Pauw method with these films) to determine the actual change in resistivity. (Data taken by Kevin Smith) The data is summarized in Table 7.4.

Etch time (s)	σ_{rms} (nm)	λ (nm)	ρ_{AP} ($10^{-5} \Omega \cdot \text{cm}$)	ρ_{P}	$\Delta\rho/\rho$ (%) (van der Pauw)	$\Delta R/R_{\text{P}}$ (meas)
90	31.8 ± 2.5	2197 ± 613	1.88	1.85	1.6	1.26
120	27.8 ± 13.2	2490 ± 766	1.28	1.25	2.4	2.39
150	46.8 ± 9.4	2771 ± 1186	1.46	1.43	2.1	1.83
210	51.5 ± 17.1	2879 ± 1388	1.17	1.14	2.6	2.99
240	94.2 ± 80.2	4951 ± 1886	1.23	1.20	2.5	2.28

Table 7.4: Comparison of root-mean-square (σ_{rms}) roughness (measured by AFM) and feature peak-to-peak length (λ) with resistivity measurements of 12x12 mm PSV films.

From Table 7.4, we observe that the van der Pauw resistivity measurements are comparable to the resistance measurements.

A graph of the antiparallel resistance versus the parallel resistance produces a linear relationship with a slope of ~ 1 . This suggests that the increase in resistivity is due to spin-independent scattering since both the antiparallel and parallel states are affected. By using Equations 2.13 and 2.14, we can determine that an increase in scattering in both spin polarizations, indicating an increase in spin-independent scattering, would produce the relationship illustrated in Figures 7.6 and 7.7.

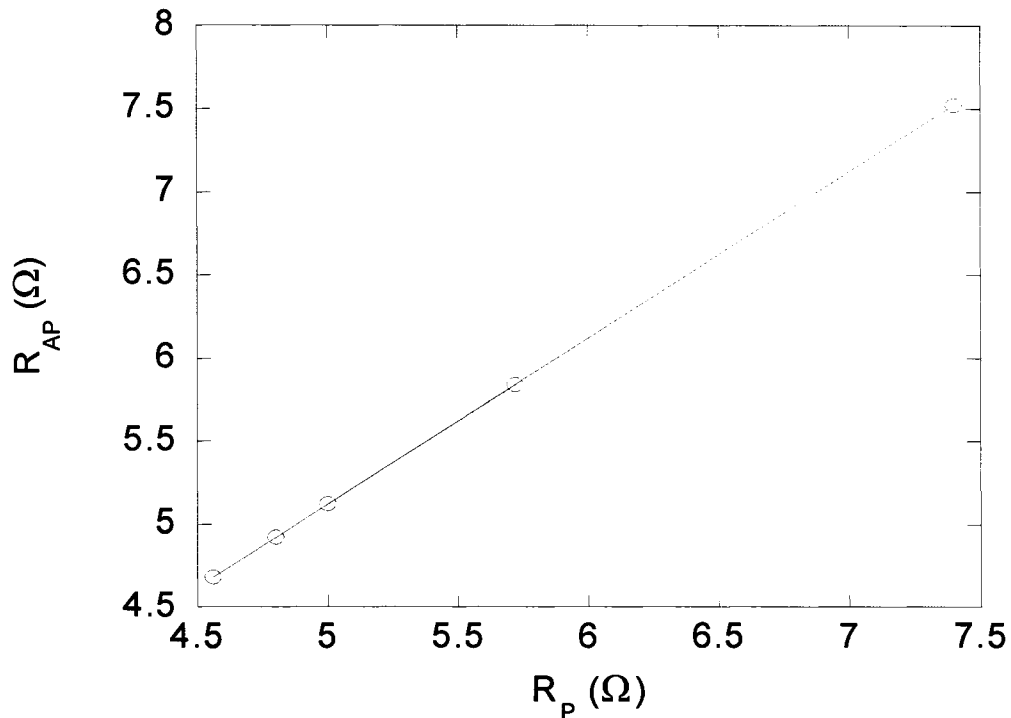


Figure 7.6: Relationship between antiparallel and parallel resistances. The data is fit by a linear relationship with slope of ~ 1 . The slope is ~ 1 suggesting that roughness is affecting the spin-independent scattering more strongly than the spin-dependent scattering.

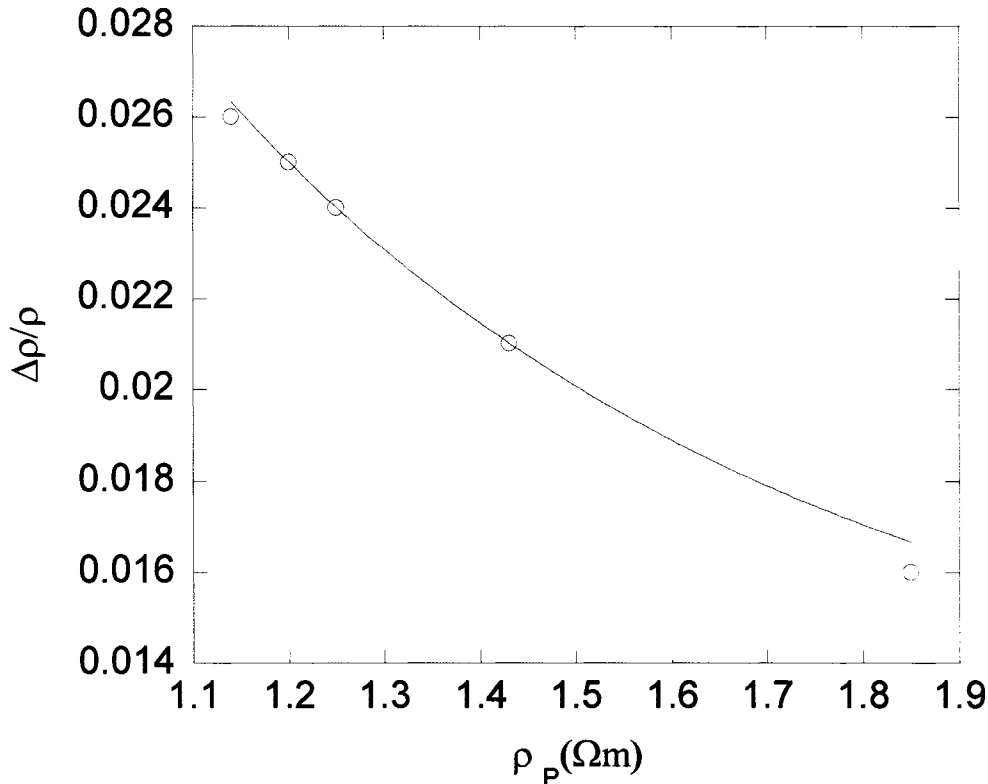


Figure 7.7: Relationship between $\Delta\rho/\rho$ and parallel state resistivity. $\Delta\rho/\rho$ shows a near inverse dependence with ρ_p . When the overall film resistivity increases, the GMR decreases. Lines are a guide to the eye.

Random increases in GMR corresponded to increases in coupling (single magnetization loops). For the 240s etched sample (the second roughest), where coupling is less significant, large GMR is seen. Unfortunately, we could not find any correlation between coupling and roughness. This coupling must be coming from some growth conditions at NIST, the source of which we do not yet know. What this data do show, however, is again, significant GMR can be obtained on a rough substrate. We turned to EBSV for better control over the magnetic state.

Figure 7.8 shows the GMR ($\Delta R/R$) curves of two EBSV samples, one on unetched glass and the other on glass etched for 150s. The GMR is seen to increase slightly and the curve is seen to also slightly broaden. This broadening is also present in the

magnetization curves, shown in Figure 7.8. The magnetization hysteresis curve for the unetched glass is squarer than for the etched substrate. The free layer loop is also not centered at zero for the etched substrate, indicating that roughness is affecting the magnetic coupling in the films.

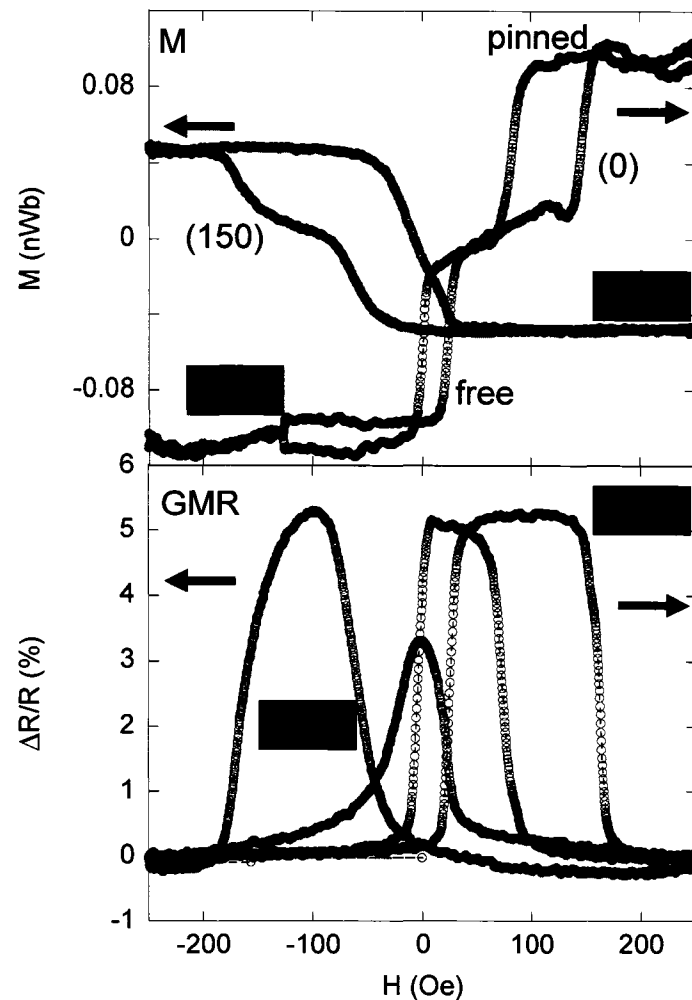


Figure 7.8: Magnetization hysteresis (top) and GMR curves (bottom) for spin valves on an unetched glass substrate (blue, circles) and a substrate etched for 150 s (red, circles). The hysteresis for the unetched glass is squarer and shows better switching than the etched glass. Notice the smaller minor GMR loop for the film on the etched film as well as the rounded peaks and the broadening of the curves. The arrows on the top plot indicate the direction of the pinning axis relative to the applied field for each sample.

Table 7.5 shows the etch times for the glass substrates, the σ_{rms} roughness (standard deviation of peak height) of the deposited films and the GMR values for the EBSV films. The GMR in general decreases with etching compared to the unetched substrate, but there is no smooth dependence. Rather, the GMR oscillates around 5.0%, approximately a 5.3% decrease in the GMR from the film deposited on the unetched substrate. The maximum decrease is about 22% for the sample etched for 210s.

Etch Time (s)	σ_{rms} (nm)	$\Delta R/R$ (%)	H_{eb} (Oe)	H_{coupl} (Oe)	H_c (Oe)
0	2.3 ± 1.1	5.28	115	12.22	10.00
30	9.4 ± 6.4	4.84	135	15.83	32.22
60	15.8 ± 10.3	5.00	103	25.00	18.61
90	9.9 ± 6.2	5.22	140	13.33	12.22
120	17.0 ± 10.6	4.67	127	11.67	10.42
150	22.7 ± 9.1	5.30	98	26.67	27.22
210	86.9 ± 47.9	4.14	112	18.33	9.72
240	74.3 ± 32.3	4.70	142	17.78	0.875

Table 7.5: Root-mean-square (σ_{rms}) roughness of films (measured by AFM) and $\Delta R/R$ for substrates etched for different durations for EBSV films.

Figure 7.9 is a graph of GMR, H_{coupl} and H_{eb} versus σ_{rms} roughness. H_{coupl} is the strength of the coupling between the ferromagnetic layers and is measured as the offset of the free layer curve from zero. This is a function of the saturation magnetization for the free layer and the roughness parameters: peak height and lateral length. The exchange bias field, H_{eb} , is measured from the shift of the center of the hysteresis curve for the pinned layer from zero. As the σ_{rms} roughness increases, the GMR fluctuates but shows no significant degradation with the exception of one film. Rather, the GMR appears to fluctuate with the H_{eb} , exhibiting a weak $1/H_{eb}$ dependence. The exchange bias and coupling fields also appear to be weakly correlated, where the increase in exchange bias

field corresponds to a decrease in coupling field, though not significantly large. The exchange bias field remains noticeably larger than the coupling field suggesting weak ferromagnetic coupling. This can be caused by a decrease in the strength of the magnetostatic coupling between the ferromagnetic layers; an effect which benefits the achievement of the antiparallel magnetic alignment and thus the GMR ratio.

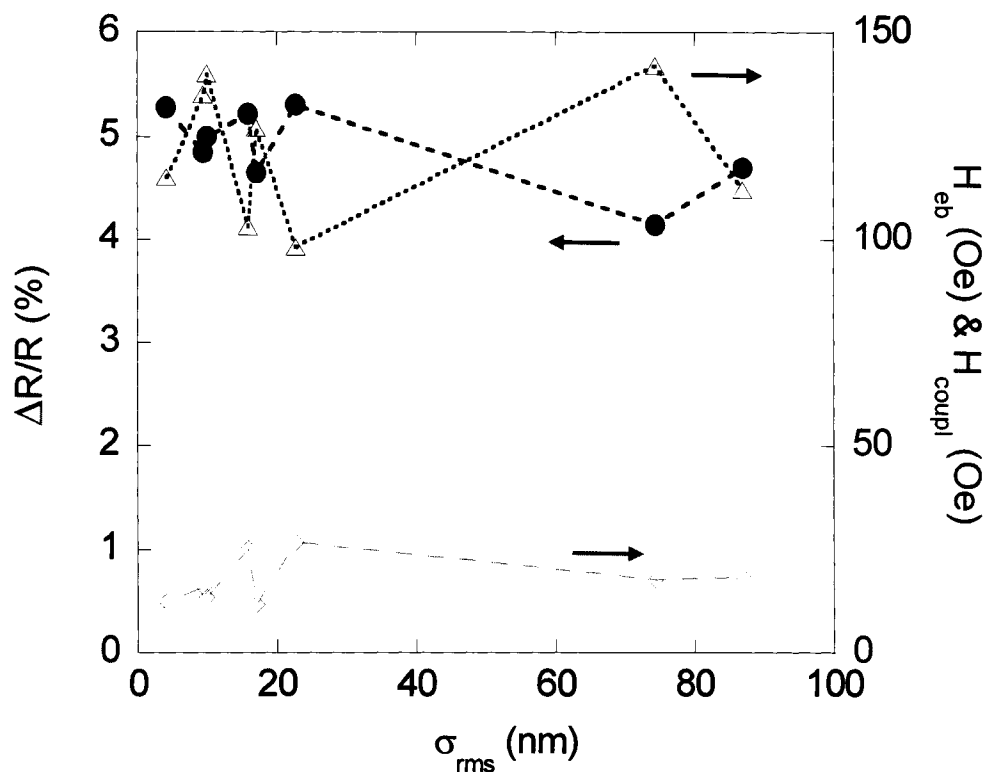


Figure 7.9: Giant magnetoresistance ($\Delta R/R$, dark red, circles), ferromagnetic coupling (green, diamonds), and exchange bias field (blue, triangles) as a function of film σ_{rms} roughness. The GMR varies around 5.0% without significantly decreasing. This may be linked to the ratio of exchange bias field to coupling field which is much greater than 1. There appears to be a weak $1/H_{eb}$ dependence but no obvious direct correlation to roughness. Lines are a guide to the eye.

Previous research has shown that large coupling indicates that the ferromagnetic layers do not switch independently of each other.⁹ The increase in the exchange biasing is noteworthy, since large amounts of lateral roughness can hinder the growth of the

antiferromagnetic layer, which is sensitive to roughness. Roughness at the AF/F interface can cause the AF layer to break into domains.¹⁰ With increasing roughness, the domain formation should increase. This would prevent the effective pinning of the top ferromagnetic layer. Yet, the decrease in GMR is not significantly large, especially considering the size of the roughness and its nonuniformity over the entire substrate. The oscillation in the GMR could indicate that the grain size oscillates between large and small as the roughness increases, affecting coherent rotation of magnetization.

Figure 7.10 compares H_{eb}/H_c and GMR with σ_{rms} roughness. The ratio of exchange bias field to coercivity, with the exception of the second-to-last point, fluctuates between 2 and 13 Oe. Correspondingly, the GMR for those points oscillates around 5.0%. The second-to-last point has a value of ~ 162 Oe but also the lowest GMR. Ideally, the H_{eb}/H_c should be large, indicating a strong exchange interaction. However, this point is misleading. The large ratio stems from the extremely low coercivity (~ 0.9 Oe) which suggests strong coupling between the ferromagnetic layers that may override a weaker exchange interaction due to the interface roughness. Fluctuations in the coercivity could also be a reflection of the changing domain size and their effect on the ease of alignment of spins.

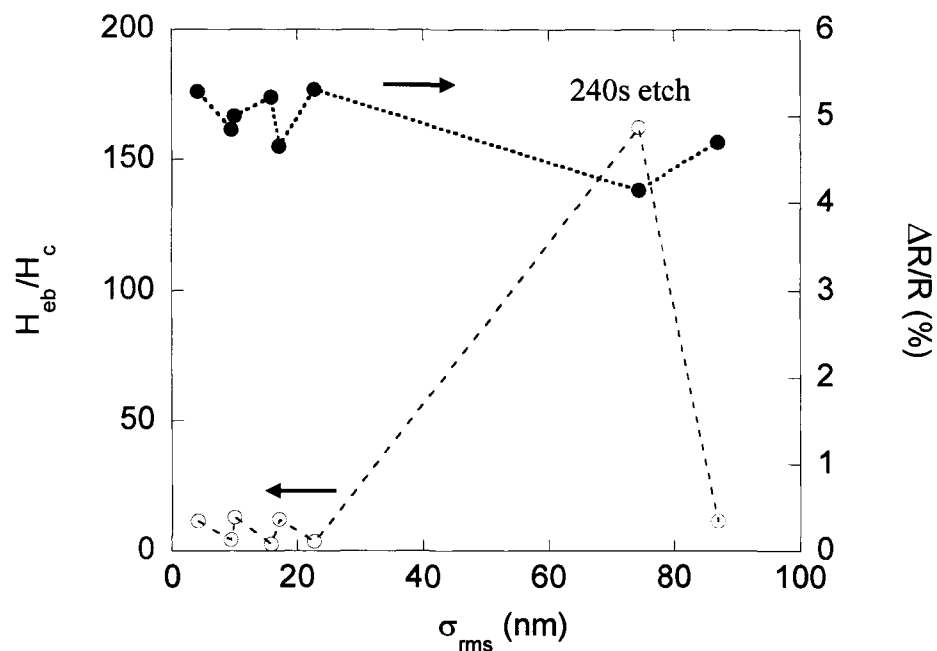


Figure 7.10: Ratio of exchange bias field to coercivity (red, open circles) and GMR (blue, closed circles) as a function of σ_{rms} roughness. There is no obvious correlation between roughness and GMR. A significant increase in the ratio of H_{eb}/H_c does not result in a significant change in GMR though it does correspond to the lowest value. This could be due to the low coercivity (~ 0.9 Oe) suggesting significant coupling between the F layers. Lines are a guide to the eye.

Hysteresis and GMR curves are shown for the film deposited on the substrate etched for 240s in Figure 7.11. The free layer coercivity for this film is extremely small as evidenced by the small width of the free layer loop. Correspondingly, the free layer loop in the GMR curve has no apparent width with the free layer transitioning from saturation to an antiparallel state easily. Also, the plateau present in the hysteresis loop would indicate that a definite antiparallel state is achieved. However, the narrowing of the free layer hysteresis loop could indicate that the magnetization of the sample is changing with the cycling applied magnetic field (training). This could be the result of the roughness or induced stress in the film.

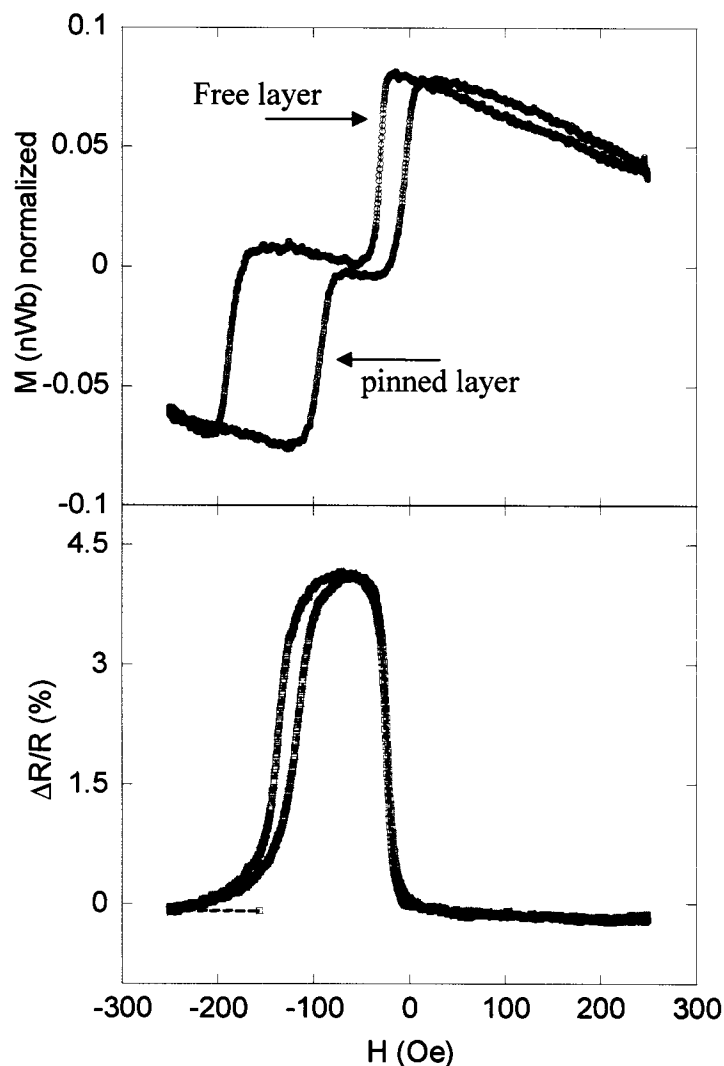


Figure 7.11: Hysteresis (top) and GMR (bottom) curves for EBSV film deposited on substrate etched for 240s. The low coercivity could be a result of significant intermixing of layers resulting in increased ferromagnetic coupling. However, the GMR is only 11% lower than the reference value.

7.3 - Conclusions

Initially, it is surprising that such large roughness does not have more of a detrimental effect on the GMR. All samples etched for more than 60s had a roughness easily visible to the eye, and yet the GMR curve was only slightly modified from that of the unetched substrate. The effect of the substrate, and hence interfacial roughness, on the GMR of the spin valves can be due to several mechanisms. Past studies of fine-scale

roughness ($\sigma_{\text{rms}} < 5$ nm) have shown that increased interfacial roughness can increase GMR due to increased interface scattering (for the case of CIP)⁵ and increased spin-dependent scattering (for the case of CPP).⁷ For our EBSV films, roughness could be decreasing the GMR through a decrease in the effective pinning of the top ferromagnetic layer by the antiferromagnetic layer. An increase in interface roughness may prevent domains in the antiferromagnet from aligning properly. The decrease in coercivity also seems to be playing a role. This could indicate an increase in interlayer coupling, which is detrimental to the GMR. The roles of each of these mechanisms needs to be further explored.

In summary, the results show that very large-scale macroscopic roughness does not have to have a large detrimental effect on GMR. Our first results even showed a slight increase in GMR. These results indicate that GMR multilayers may be successfully deposited on a variety of non-traditional buffer layers and substrates even if their roughness is not comparable to silicon wafers. To further the understanding of the effects of roughness, we desire to study a system with much more control over roughened features than provided by chemical etching. For this, we turn to the use of nanodots, which will be described in the following chapter. By varying the length scale of the roughness, laterally and vertically, in a uniform manner, perhaps a more detailed understanding of the relationship between GMR and roughness can be found.

7.4 - References

- ¹ M. C. Cyrille, S. Kim, M. E. Gomez, et al., *Phys. Rev. B* **62**, 3361 (2000).
- ² W. F. Egelhoff, Jr., P. J. Chen, C. J. Powell, et al., *J. Appl. Phys.* **82**, 6142 (1997).
- ³ R. Schad, P. Belien, G. Verbanck, et al., *Europhys. Lett.* **44**, 379 (1998).
- ⁴ E. E. Fullerton, D. M. Kelly, J. Guimpel, et al., *Phys. Rev. Lett.* **68**, 859 (1992).
- ⁵ J. Alicea and S. Hershfield, *J. Appl. Phys.* **93**, 7930 (2003).
- ⁶ R. Paniago, H. Homma, P. C. Chow, et al., *Phys. B* **221**, 10 (1996).
- ⁷ M. C. Cyrille, S. Kim, M. E. Gomez, et al., *Phys. Rev. B* **62**, 15079 (2000).
- ⁸ S. Miura, M. Tsunoda, and M. Takahashi, *J. Appl. Phys.* **89**, 6308 (2001).
- ⁹ T. Rijks, R. Coehoorn, J. T. F. Daemen, et al., *Journal of Applied Physics* **76**, 1092 (1994).
- ¹⁰ H. De-Hua, Z. Jian-Gang, J. H. Judy, et al., *Journal of Applied Physics* **81**, 340 (1997).

Chapter 8 — Nanodot Controlled Roughness Study

In order to gain insight into the effects of substrate roughness, we desire to produce controllable, periodic roughness that will correlate with the type of roughness that has been modeled theoretically. As was shown in last chapter, etching can produce roughness with average height and wavelengths that do increase with etching time. We desire, however, a much more controllable system, particularly one in which we can achieve a wavelength comparable to the mean free path of the electrons in the multilayers. Etching with hydrofluoric acid did not allow sufficient control over the size of the longitudinal and vertical roughness parameters to provide either long range order or the length scale desired.

To this end, we explored the use of metal nanodots to produce a periodic pattern of roughness in the GMR multilayers. The general idea is illustrated in Figure 8.1. In this study, GMR multilayers were deposited on a pattern of pre-deposited gold nanodots with varying widths and separations. When a multilayer is deposited onto these dots, roughness is induced in the multilayer as illustrated in Figure 8.1.

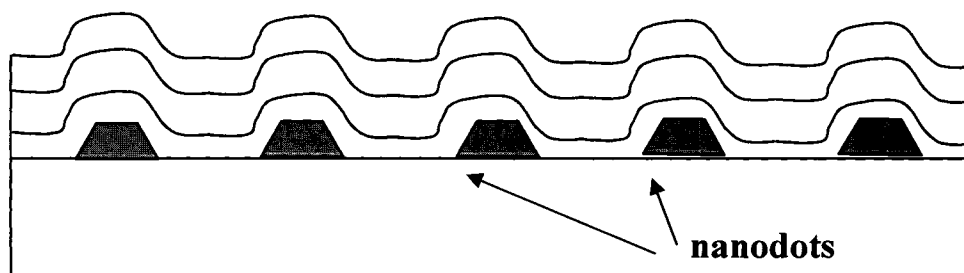


Figure 8.1: Cartoon illustrating the use of nanodots to produce roughness in the thin film multilayers.

This chapter presents an initial study of GMR in multi-period multilayers and exchange biased spin valve films in the both current-in-plane and current-perpendicular-to-the-plane geometries. The CPP geometry is explored because GMR depends on a different length scale than CIP and may be affected differently by the roughness. In the current-perpendicular-to-the-plane geometry, the finite spin diffusion length has greater importance than the mean-free path in the limit where $t_N, t_F \ll l_{sf}$.^{1, 2} In this limit, the distance before a spin flips is the important length scale. Spin-dependent scattering along the interface does not dominate as the $\lambda_{mfp}/l_{sf} \ll 1$.

We find that the addition of substrate roughness for GMR thin films has a noticeable affect on CIP and CPP-GMR. For the CIP films, GMR was shown to decrease with increasing parallel state resistivity while the antiparallel state resistivity increased linearly (slope ~ 1) with increasing parallel resistivity. This suggests that substrate roughness has a significant effect on spin-independent scattering but less so on spin-dependent scattering. For the CPP films, a similar increase was observed in antiparallel resistance with increasing parallel resistance though resistivity measurements are not available. For both systems, the effect on GMR is not as large as might be expected due to the large scale of roughness. The CIP-GMR is observed to have a large decrease in GMR but with a recovery of 80% compared to the reference film which has no nanodots. Initially, the decrease in CPP-GMR with roughness is small but recovers to within 97% of the reference value for an exchange biased spin valve and 99% for a multilayer spin valve.

8.1 – Roughness from Nanodots

Metal nanodots were first deposited onto the silicon substrates using polystyrene spheres of various sizes. The procedure for the nanodot production was modeled after reports from Holloway's group.³⁻⁵ First, polystyrene spheres were spin-coated onto the silicon wafers, forming ideally a single layer. Approximately 15 nm of metal is then evaporated onto the spheres. The metal deposits in between the spheres, and when the spheres are washed away, a pattern of nanodots is left behind, as shown in Figure 8.2.

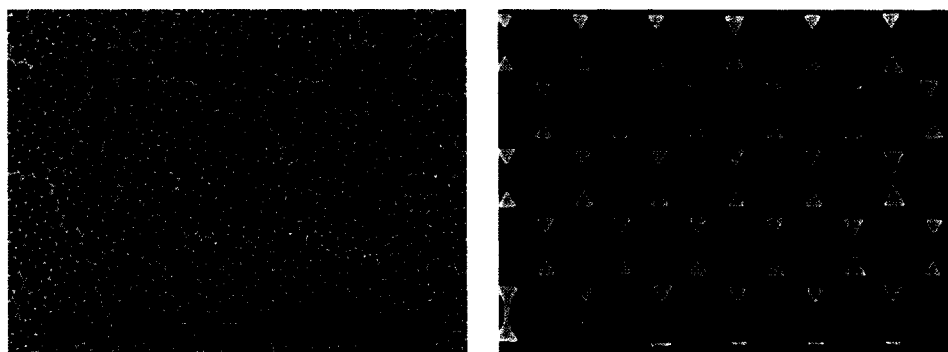


Figure 8.2: Left: SEM image of nanospheres spin-coated onto silicon. Right: Pattern of metal nanodots left behind after evaporation and removal of nanospheres. Images courtesy of Mingyao Zhu.

For this thesis work, polystyrene spheres from Bang Laboratories were used in diameters of 20, 50, 160, 190, 250, 320, 460 and 560 nm and were spin-coated onto 2" silicon wafers with a rotational rate of approximately 3000-5500 rpms. The wafers were shipped to Lebow Company for evaporation of 15 nm of Au. Upon their return to W&M, each wafer was sonicated in dichloromethane for removal of the polyspheres. Considering the geometry of a single-layer of packed spheres, the separation between the deposited metal dots and their diameter can be estimated. The average separation, d_T , is given by $d_T = D/\sqrt{3} \sim 0.577D$ while the length of the edge of a dot is $\phi_T \sim 0.23D$,

where D is the diameter of the dots.³ Table 8.1 summarizes the theoretical values for d_T , and ϕ_T , as well as average measurements from SEM photos taken after deposition of the nanodots (data taken by Kevin Smith).

Sphere diameter D	d_T (calculated)	d_T (measured)	ϕ_T (calculated)	ϕ_T (measured)
20	12	-	5	-
50	29	-	12	-
160	93	90 ± 11	37	27 ± 3
190	110	103 ± 7	44	38 ± 10
250	145	179 ± 20	58	45 ± 1
320	186	175 ± 17	74	61 ± 17
460	267	228 ± 20	106	68 ± 16
560	325	515 ± 8	129	222 ± 25

Table 8.1: Calculated and average measured separations, d_T , and sizes, ϕ_T of nanodots deposited using polystyrene spheres. Data courtesy of Kevin Smith. All dimensions are in nm. For two dot sizes, the sizes could not be resolved.

As the height of the nanodots should be uniform (15 nm of material was evaporated), the Table shows that using the nanodots allows us to control in general the wavelength of the roughness (determined by the distance between dots, d_T). The measured separation between dots does match the calculated values within error except for the largest dots (could not be measured for smallest dot patterns).

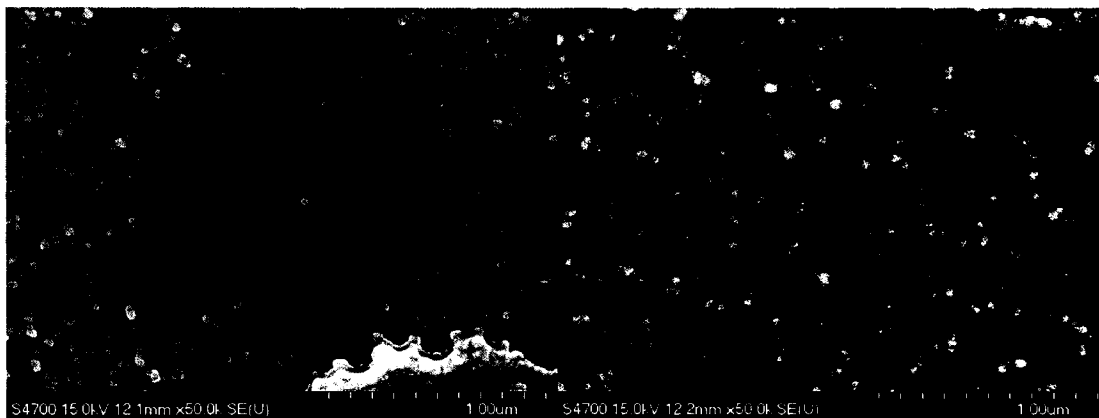


Figure 8.3: SEM scans of nanodots. Left: Au deposited onto 190 diameter nanospheres. Right: Au deposited onto 320 diameter nanospheres. The degree of uniformity over the surface was inconsistent from film to film. Courtesy of Kevin Smith.

8.2 - CIP and CPP Multilayers on Nanodot Patterns

Multilayers were deposited onto the nanodot patterns using the magnetron sputtering chamber at Michigan State University with the aid of Dr. Reza Loloee. The MSU chamber was used because it was equipped to produce exchange-biased spin valves as well as samples in the CPP geometry with Nb superconducting contacts.

For the CIP samples, an exchange biased spin valve of form Nb 30Å/Cu 50Å/Co 40Å/Cu 40Å/Co 40Å/FeMn 100Å/Cu 30Å/Nb 20Å was used, as well as a multilayer of the form Nb 30Å/[Cu 50Å/Co 40Å]₁₀/Cu 30Å/Nb 20Å. At MSU, each wafer with the nanodot pattern was sonicated in toluene to insure complete removal of the polyspheres. Each coated wafer, along with an uncoated wafer, was diced into ~ ½" x ½" substrates and then sonicated in acetone and 2-propanol before deposition. Three substrates from each wafer were randomly loaded into the sample holder tray which was then loaded into the deposition chamber. The number of substrates required two separate runs to deposit all films. Prior to sealing the system, two pieces of copper were compressed together on the end of the sample holder rod to provide good thermal contact allowing for sufficient

heat transfer to cool the entire substrate holder. The chamber was sealed and pumped overnight with a cryopump to a base pressure of 4×10^{-8} Torr. A cold trap was cooled to ~ -190 °C with liquid nitrogen, producing an ultimate base pressure of 3×10^{-8} Torr. Additionally, pure (99.99%) nitrogen gas was released into the system via a capillary tube, quickly pressurizing and cooling the nitrogen. The pressurized nitrogen was used to cool the sample holder tray to ~ -20 °C and maintain a temperature reading between -30 °C and 30 °C during deposition. In this temperature range, island formation is minimized due to lack of atom mobility along the surface. Then, the cryopump was isolated from the deposition chamber by a gate valve and pure (99.99%) Ar was released into the chamber. The pressure was allowed to rise by gradually opening the gate valve until the deposition chamber reached $\sim 2.5 \times 10^{-3}$ Torr. The magnetron sources and filaments were turned on and the filaments' voltages and currents were increased slowly. The films deposited in this experiment were grown with sputtering rates: Nb at 4.9 \AA/s , Co at 5.3 \AA/s , Cu at 7.1 \AA/s and FeMn at 5.3 \AA/s . At this point, deposition rates were monitored through a Labview program designed by Dr. Loloee. This program determines the deposition time for each layer, opens and closes shutters, as well as aligning individual substrates over each target.

For the CPP samples, the nanodot patterns had to be produced at MSU on top of the first superconducting Nb contact used for measurement of the CPP. If the $\sim 2 \text{ \mu m}$ thick contact had been deposited on top of the nanodots instead of the other way around, the roughness would have been averaged over and would have no affect on the GMR multilayers. First, the bottom Nb contacts were deposited onto bare silicon wafers, in conditions similar to those for the CIP samples. The Nb contacts were coated with 10 \AA

of Au to prevent oxidation. Then, the substrates were removed from the deposition chamber and polystyrene spheres of four sizes (20, 50, 99 and 130 nm) were spin-coated onto the silicon and Nb with a rate of ~ 5000 rpm. Then, Au was evaporated onto the spheres with a thickness of ~ 150 Å. The spheres were then washed off, the substrates cleaned in the procedure outlined above, and then placed back into the deposition chamber where the GMR spin valves and multilayers (described above) were grown onto the nanodots, as well as the top Nb superconducting contacts.

Initially, sixteen substrates were prepared, but only eleven films were actually grown. Three were misaligned during sputtering and resulted in an improper overlap of the masks. The last two films were not deposited as a result of a malfunction with the mask rotation. Of the eleven remaining films, three were reference films; no additional substrate roughness was added.

Note that while initial conditions for all depositions, both CPP- and CIP-GMR, were similar, they were not exact due to the number of prepared substrates and the need to return to atmosphere to load and unload new substrates.

For both the CIP and CPP films, Magneto-Optical Kerr Effect (MOKE) was used to measure the magnetization of the $[\text{Cu}/\text{Co}]_{10}$ multilayer films. The magnetization of the EBSV films was measured using a BH Looper at NIST. CIP-GMR was measured by the four-point probe method, with a constant current source and voltage measurements provided by a multimeter. CPP-GMR was measured at MSU using the SQUID design described in chapter 4. Film roughness, for all films, was characterized by atomic force microscopy (AFM - Digital Instruments Nanoscope IV) at the Applied Research Center

located at the Jefferson Lab. A scanning electron microscope (SEM - Hitachi), located at W&M, was used to measure the surface morphology.

8.3 - CIP Results and Discussion

The CIP films were analyzed at William and Mary by Dimitar Vlassarev and were the basis for his senior thesis.⁶ To summarize Dimitar's findings, he found for the multi-period GMR multilayers a general decrease in GMR with increasing nanodot size which he attributed to a decrease in RKKY coupling. For the EBSVs, he found that there was significant ferromagnetic layer coupling that seemed to follow the dependence on nanodot separation (or wavelength) expected from orange peel coupling (see Equations 2.31 and 2.32). The GMR did not show a trend with increasing nanodot size. The AP and P state resistivity were greater for the films with nanodots versus a reference film without nanodots, and the GMR was always much less than the 6.0% value measured for the reference film. The data are summarized in Table 8.2. With increasing nanodot size, the GMR (%) decreases by almost 80% to a minimum of 1.2%, but also obtains values to within 75% of the control sample value.

Nanosphere size (nm)	$\Delta R/R$ (%)	ρ_P ($\mu\Omega\text{cm}$)	ρ_{AP} ($\mu\Omega\text{cm}$)	$\Delta\rho$ ($\mu\Omega\text{cm}$)
Reference	6.0116	5.985	6.3448	0.35976
50	2.3295	13.864	14.184	0.32017
99	2.2773	16.714	17.096	0.38259
160	2.1381	19.27	19.682	0.41178
190	1.8277	14.318	14.579	0.26079
250	3.4077	9.8973	10.234	0.33716
320	1.1771	18.15	18.362	0.21283
460	4.3341	7.7223	8.0561	0.33376
560	4.4752	8.3776	8.7504	0.37278

Table 8.2: Nanosphere size, P and AP resistivity and GMR percent of CIP data. No obvious direct correlation between nanosphere diameter and GMR or film resistivity. Data and analysis by Dimitar Vlassarev.

Although there was no consistent increase or decrease with nanodot size, Dimitar did find that the GMR (%) did decrease in general with increasing parallel state resistivity. This data is summarized in Figure 8.3. This seems to correspond to what was seen for the series of PSV discussed in the previous chapter. What this implies is that the increasing wavelength roughness only increases the spin-independent scattering and does not greatly affect the spin-dependent scattering.

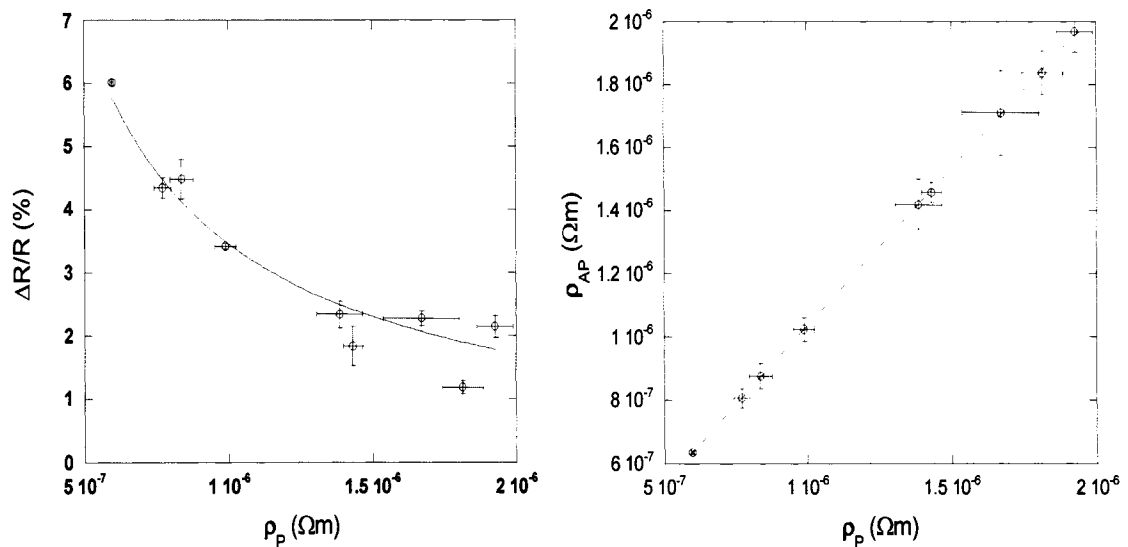


Figure 8.4: Left: CIP-GMR (%) on nanodot patterns as dependent on parallel state resistivity. Fit shows the ρ_p^{-1} dependence expected if only spin-independent scattering were increasing. Right: Plot of Measured ρ_{AP} versus ρ_p , with a fit to a linear dependence. Data courtesy of Dimitar Vlassarev.

Figure 8.4 shows that the antiparallel state resistivity, ρ_{AP} , increases with the same rate as ρ_p . Using the simplified model of CIP-GMR presented in Chapter 2 (see Equations 2.13 and 2.14), we argue that such a linear increase with slope of ~ 1 indicates that only spin-independent scattering is being increased by the roughness, and spin-dependent scattering is not being greatly affected.

8.4 - CPP Results and Discussion

Exchange Biased Spin Valves

AFM measurements before deposition of Au nanodots show varying success at achieving uniform wafer coverage with the spin-coating technique. Nanosphere diameters greater than 300 nm produced better uniformity than smaller diameters. However, the long range order for the spin-coatings degraded above 1 μm for all diameters, resulting in non-uniformity over the substrate area covered by the thin films. The AFM scans of Figure 8.5 illustrate the change in coating uniformity with area size. Root-mean-square roughness and peak-to-peak measurements were taken on the AFM and SEM to provide some correlation between substrate roughness and magnetic thin film properties.



Figure 8.5: AFM scans in Tapping Mode of SiO_2 wafer spin-coated with 320 nm diameter polymer spheres. a) Scan size is 1 μm x 1 μm . b) Scan size is 10 μm x 10 μm . Long range order decreases above 1 μm .

Figure 8.6 shows representative GMR curves for a CPP-EBSV without and with a nanodot pattern. Giant magnetoresistance curves for all films exhibit moderately sharp rises in resistances when the films switch from parallel to antiparallel states. Saturation

loops do not overlay when cycling from high field to low field and vice versa. The curve has a lower resistance when going to high negative field and a higher resistance on the return loop. When cycling to high positive field, this pattern is reversed and occurs for the film without nanodots as well as those with nanodots. This could be explained by a lower resistive state existing between 0° and 90° . The resistance difference between the outgoing and ingoing saturation loops is approximately $0.1 \text{ n}\Omega$ for both high negative and high positive fields. The measurement was repeated one day later without any change. Repeating the loop several times during the same measurement cycle also produced no change in the curves. This was the case for all of the measured films.

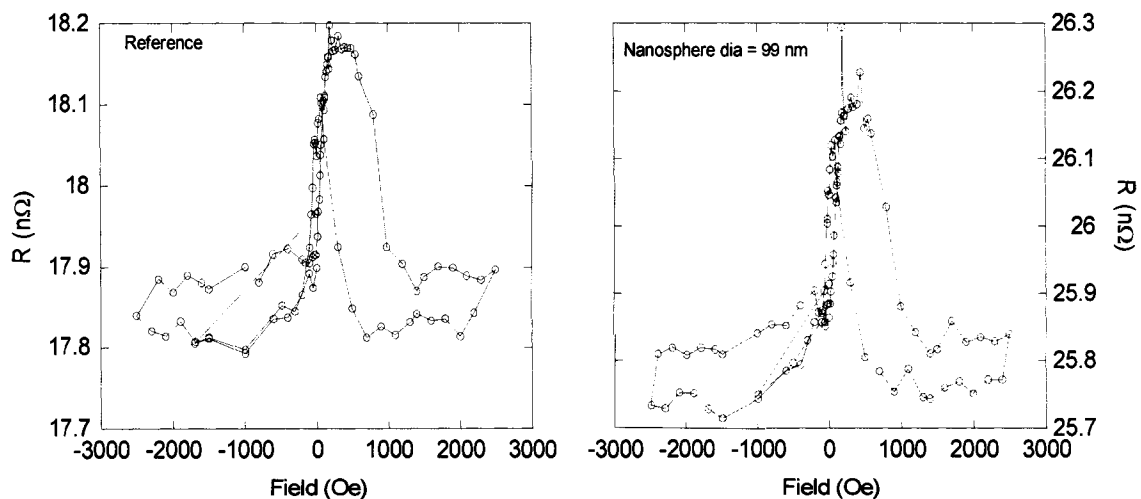


Figure 8.6: GMR curve of EBSV with no nanodots and with nanodots deposited on 99 diameter polyspheres. Outgoing and ingoing saturation loops do not overlap suggesting a low resistance state between 0° and 90° .

Comparatively, thin film magnetic properties, shown in Table 8.3, are somewhat ambiguous. In this table, the exchange bias field, the coercive field of the minor loop (the free layer), the coupling field, and the GMR values are given. For the films with nanodots, there is an increase in the exchange bias with increasing nanodot diameter.

The exchange bias remained within 20% of the reference film value. Still, the exchange bias varied randomly from sample to sample with a minimum corresponding to the reference film and a maximum for films deposited on the 20 nm nanodots. The remaining values show no clear increase or decrease in value with increasing diameter. Nor do the coercivities show a definitive pattern. The coercive fields, except for the film grown on 20 nm, were within ~10% of the reference of 78.75 Oe. The coercivities do not appear to change significantly from film to film and none of the loops exhibit definitive square loops, suggesting that some switching is taking place before the AP state. The saturation loops would seem to support this somewhat by the significant gap between the outgoing and incoming scans. There is evidence of orange peel coupling in the films with nanodots. The coupling does not appear significant relative to the exchange bias field and does not show a definitive increase or decrease with nanosphere size, coercivity, or exchange bias field.

Diam (nm)	H_c (Oe)	H_{ex} (Oe)	H_{coupl} (Oe)	R_P (nΩ)	R_{AP}	ΔR	GMR (%)
Reference	78.75	533	0	17.85	18.17	0.32	1.79
20	43.75	633	44.4	30.48	30.98	0.51	1.66
50	74.166	600	26.7	23.00	23.30	0.30	1.3
99	78.75	550	30.6	25.80	26.18	0.38	1.45
130	70.14	558	53.3	20.25	20.60	0.35	1.73

Table 8.3: EBSV films with and without Au nanodots. The coercivity, exchange field, coupling field, P and AP resistivity and GMR (%) vary without displaying any particular trend with nanodot diameter.

All of the films with nanodot roughness exhibited an increase in both parallel and antiparallel specific resistance compared to the reference film. This may be explained by the increased roughness introduced at the interface through the substrate. At first glance, the changes in both the parallel and antiparallel resistances, listed in Table 8.3, do not

appear to increase or decrease with interfacial roughness but seems somewhat random. Moreover, the change in resistance, ΔR , varies similarly. Interestingly, the GMR (%) decreases and then increases with the polysphere diameter as though passing through a local minimum. The maximum decrease in GMR compared to the reference sample is 27%, but for the larger nanodot pattern, the GMR recovers to within 97% of the reference value.

Figure 8.7 shows the variation of coercivity and exchange bias field as a function of nanosphere size. As can be seen, there is no general increasing or decreasing trend, although for the smallest nanosphere (nanodot) size, there is both a dramatic decrease in coercivity as well as an increase in H_{eb} .

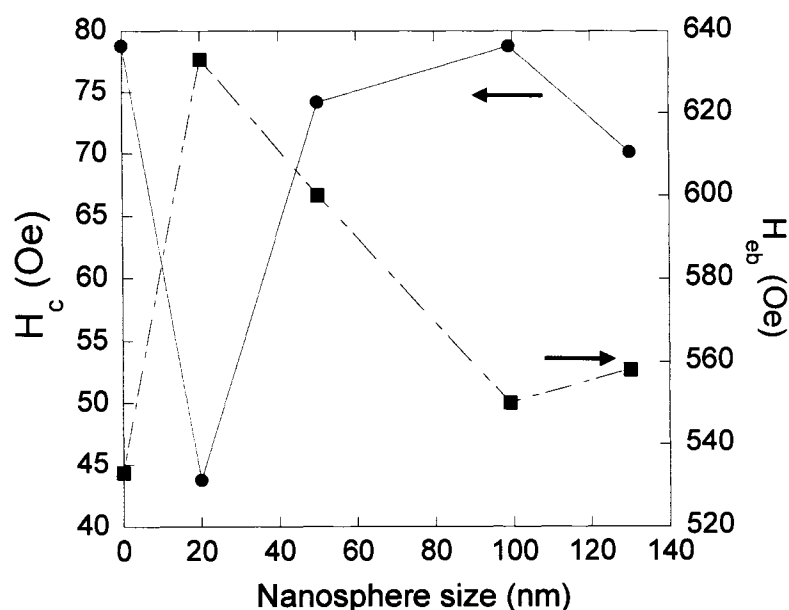


Figure 8.7: Coercivity (red, closed circles) and exchange bias field (blue, closed squares) for CPP-EBSV as a function of nanosphere size used to produce the nanodots. “0” indicates no nanospheres. Lines are guide to eye.

Figure 8.8 (left) shows the relationship between the GMR (%) and the nanosphere size. As mentioned, it seems like the GMR goes through a minimum and then recovers close to its original value. Figure 8.8 (right) shows the antiparallel state resistance (R_{AP}) versus parallel resistance (R_P). Actual film resistances are shown here, since the contact resistance is zero (superconducting contacts). The values can be directly converted to resistivities since the area and length of the sample is known. Surprisingly, the relationship is exactly linear, again with a slope of 1.0, like the CIP data shown in Figure 8.4. Again, this indicates that the only effect the large-scale roughness is having is increasing the spin-independent resistivities, since R_{AP} and R_P are increasing with the same rate.

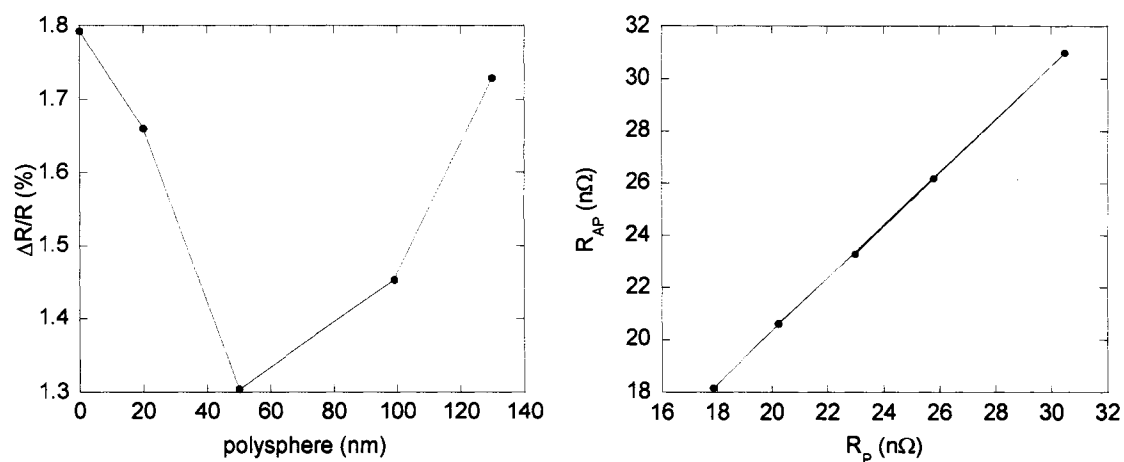


Figure 8.8: Left: GMR (%) for CPP-EBSV as a function of nanosphere size used to produce the nanodots. Line is guide to eye. Right: antiparallel state resistance (R_{AP}) versus parallel resistance (R_P). Line is a linear fit, with slope of 1.0.

Multilayers: [Cu 50Å/Co 40Å]₁₀

The same coating technique was used to prepare substrates for the [Cu/Co]₁₀ multilayer films. As discussed above, scans of the substrate surface prior to deposition show a non-uniform coverage above 1 μm that increases with smaller diameter spheres. We observe a significant increase in the film with 20 nm nanospheres followed by a

decrease in resistance for the 71 nm spheres, as summarized in Table 8.4. This parallels the change in resistance observed in the EBSV where the film with 20 nm spheres exhibits a significant increase in resistance when compared to all other films. If R_{AP} is plotted as a function of R_P , these three points do fall on a line with slope ~ 1 , again similar to the EBSV data. However, since this is only three points, this data is not shown. It should be pointed out that the GMR (%) value for the 71 nm nanosphere sample is 99% of the reference value.

Diameter (nm)	R_P (n Ω)	R_{AP} (n Ω)	ΔR (n Ω)	$\Delta R/R_P$
Reference	19.00	20.81	1.81	0.0952
20	37.55	39.03	1.48	0.0395
71	20.15	22.05	1.90	0.0943

Table 8.4: Multilayer thin films, [Cu 50Å/Co 40Å], with and without Au nanodots. Resistances are listed for parallel and antiparallel states.

8.5 Summary

This work was a preliminary study showing the promise of using nanodots deposited using polystyrene nanospheres to produce controllable, large-scale roughness. Producing uniform roughness over a 2" wafer was a challenge, believed to be due to the difficulties in spin-coating a uniform, single-layer film of nanospheres. Primarily, the difficulty lay in determining an initial speed which produce uniform coverage followed by a sharp increase in speed at which the spheres would coat the wafer (within a 12 mm sq. area) without leaving gaps or without producing multilayers. As a secondary issue, the spheres were diluted to decrease conglomeration without reducing the number of spheres per mole too greatly to hinder uniform coverage. In order to spin-coat layers of various sizes, we experimented with different solutions for each polysphere diameter and

various speeds for each solution. AFM measurements were taken after spin-coating to determine the coating uniformity and adjustments were made either in the dilution step or the coating speed and then scanned again with the AFM. Removal of the polymer nanospheres after evaporation of Au nanodots on the wafer was also a concern. It was not immediately clear that the removal had been completely successful. Consequently, various solvents were experimented with to insure removal of the spheres followed by AFM measurements of the surface when possible. It was discovered that some non-uniformity existed in the form of gaps and multilayers over the wafer surfaces.

However, analysis of these films shows that viable GMR films can be produced on these roughened surfaces. Again, the only detriment appears to be an increase in spin-independent scattering, with little or no change in the spin-dependent scattering which is the critical mechanism for GMR. The CPP films appeared to suffer less loss to GMR than the CIP films, reaching nearly the reference sample values for larger nanosphere (nanodot) sizes. This could be due to the dependence of CPP on spin flip length, which is longer than mean free path. It could also be due to the CPP current flowing through less resistive pathways through the stack of layers, which means that roughness would have less of an effect in this geometry. Consideration of CIP and CPP theory to explain these effects in detailed are being undertaken.

8.6 References

- ¹ J. Bass and W. P. Pratt, Jr., *Physica B* **321**, 1 (2002).
- ² T. Valet and A. Fert, *Phys. Rev. B* **48**, 7099 (1993).
- ³ J. Wang, M. Zhu, Z. Xin, et al., in *International Vacuum Microelectronics Conference*, edited by M. Taki, Y. Gotoh and J. Ishikawa (Japan Soc. Promotion of Sci., Japan, 2003), p. 157.
- ⁴ A. J. Haes, J. Zhao, S. Zou, et al., *J Phys Chem B* **109**, 11158 (2005).
- ⁵ X. Zhang, E. M. Hicks, J. Zhao, et al., *Nano Lett* **0**, A (2005).
- ⁶ D. Vlassarev, "Effects of Large Scale Interfacial Roughness on Giant Magnetoresistance in Exchange Biased Spin Valves and Co/Cu Multilayers", Senior Thesis, Physics Department. College of William & Mary (2005).

Chapter 9 — Carbon Nitride Based Thin Films

This thesis work has explored the use of non-traditional buffer layers and intentionally roughened substrates for GMR multilayers. One class of materials which is important to explore are carbon-based materials, because of their beneficial qualities. Incorporation of carbon-based materials in magnetic multilayers may enhance their properties and behavior. This chapter presents a study of the effects on magnetization of magnetic films deposited on hard and elastic carbon nitride. Analysis of the films is compared with similar films deposited on traditional buffer materials.

Carbon nitride (CN_x , $0.1 < x < 0.3$) has generated interest because of its unique combination of hardness and compliance. Its physical properties: high hardness, low friction coefficient, good chemical inertness, thermal stability and low wear rates make it a suitable choice for many applications.¹⁻³ Depending on the desired properties, carbon thin films can be tailored as graphitic or fullerene-like. Carbon forms four bonds with its s and p orbitals that can be sp , sp^2 , or sp^3 hybridized. Further, cross-linking between sp^3 orbitals causes buckling of the graphitic planes, which is responsible for the high hardness of carbon-based materials. These variations in atomic hybridization allow for a spectrum of physical properties based on growth conditions, from the “soft” amorphous-like material to a “hard” diamond-like or fullerene-like structure.^{4, 5}

Amorphous carbon nitride describes the lack of long-range-order (LRO) of the carbon film. The short-range-order, however, may be graphitic and dominated by sp^2 hybridization of the orbitals or a fullerene-like CN structure with cross-linked sp^2 orbitals as well as sp^3 hybridization. Amorphous CN_x strongly bonds to ordinary Si <100> wafers forming a hard coating,⁴ which, along with its band gap structure, might make amorphous carbon nitride (a- CN_x) useful in electronic and computer applications.⁴ Currently, some hard drive media use a- CN_x as a protective coating but coating applications have not been extensively studied.^{4,6} Nonetheless, a-CN has been shown to have a wear rate lower than that of diamond-like-carbon (DLC), currently, the industry standard for magnetic media coating. As it has a lower wear rate, a thin layer of a-CN could replace the thicker DLC leading to a reduction in the read head-to-hard drive distance.

Both a- CN_x and fullerene-like carbon nitride (FL- CN_x) may also be useful when incorporated directly into ferromagnetic multilayer structures (such as those displaying giant or tunneling magnetoresistance) as a buffer, capping or active electronic layer. Its properties may enhance the robustness of the ferromagnetic structure and prevent deterioration due to chemical corrosion or thermal annealing. In addition, its excellent thermal properties and varying impedance (based on growth conditions) make it useful for microelectronic devices.

Before incorporation into magnetic thin film devices, researchers must determine how CN_x will affect magnetic properties of devices utilizing giant magnetoresistive structures. This chapter discusses the effects of substrate roughness on the magnetic

properties of magnetic thin films and the implications for giant magnetoresistive thin films.

In this chapter, we show that both a-CN_x and FL-CN_x buffer layers have comparable smoothness to traditional buffers. While, a-CN_x has a detrimental effect on magnetic properties, films deposited on FL- CN_x show minimal or no degradation of magnetic mechanisms.

9.1 - Preparation of Magnetic Thin Films

Esteban Broitman at W&M prepared amorphous carbon nitride as a buffer material prior to the deposition of magnetic thin films. The a-CN_x films were deposited in a high-vacuum dc magnetron sputtering system after reaching a base pressure of 2×10^{-7} torr. Pure nitrogen (99.998%) was released into the vacuum chamber through a mass flow controller which, combined with turbo pump throttling, maintained a constant chamber pressure of 8 mTorr during deposition. Carbon was sputtered from a high-purity (99.99%) graphite target, 2" in diameter, positioned 10 cm from the substrate holder. The films were deposited onto grounded 4" diameter single-crystal <100> Si substrate wafers heated to 300 °C. The wafers were cleaned in a sonic bath of acetone followed by isopropanol prior to loading into the chamber. The magnetron typical discharge current and voltage were 0.3 A and ~ 615 V, respectively. The deposition rate of CN_x was determined to be 9-10 nm/min, as measured by surface profilometry. The thicknesses ranged from 180 to 220 nm across the wafer. Prior to the NiFe deposition, ½ cm by ½ cm square cuts were made from the center of the CN_x coated wafer. Center cuts were taken in order to obtain more graphitic CN_x instead of fullerene-like CN_x that begins to form more than one inch from the center.

Characterization of the CN_x films was conducted by the same collaborator to determine properties of the films before depositing the magnetic thin films. High-resolution transmission electron microscopy (HRTEM) has shown that the films were amorphous and not crystalline. Nanoindentation experiments carried out with a Triboscope (Hysitron Inc.), using a cube corner diamond tip with an indentation load of 40 μ N, have shown a hardness of ~ 8 GPa and an elastic recovery of 60%.

After characterization of the a- CN_x films, in a separate 2-gun sputtering chamber, NiFe was deposited at room temperature onto the CN_x film by dc magnetron sputtering. The CN_x films were placed in the sputtering chamber two days after their growth and were not pre-treated in any way. The chamber base pressure (roughing and cryo-pumped) was 5×10^{-8} Torr. Pure argon (99.998%) was introduced into the chamber through a mass-flow controller maintaining a sputtering pressure of 2 mTorr. Substrate-to-target distance was 6" along the center line at angle $\theta = 17.5^\circ$ from each gun. NiFe layers with thicknesses of 1, 2, 3, 5, and 10 nm were sputtered from a target of 81% Ni and 19% Fe at a deposition rate of 1.0 $\text{\AA}/\text{s}$. As reference samples, NiFe films with 10 nm Cu and Ta buffer layers (at 1.0 $\text{\AA}/\text{s}$) were also deposited under the same vacuum conditions. Capping layers were not deposited on any of the samples. After depositing each Si/buffer/NiFe film, the ten films, two for each thickness, were divided into two groups. One group was annealed for four hours in an argon environment at approximately 200 $^\circ\text{C}$ in a controlled ambient oven. The oven was evacuated followed by an argon purge to minimize contamination to atmospheric gases during annealing. For consistency, each set of Si/x/NiFe films was annealed the day after deposition.

Unannealed films were kept in vacuum desiccators to hinder oxidation and water absorption.

For comparison purposes, single Co films deposited at MSU, on fullerene-like CN_x substrates prepared by contributors in Sweden, will be discussed in this chapter as well. Growth parameters of the FL- CN_x films included a substrate temperature of 450 °C with a substrate bias of – 40V. One film was deposited in a 50-50% N_2 /Ar mixture discharge gas while the other was grown in 100% N_2 . Growth of FL- CN_x was facilitated by dc reactive sputtering using unbalanced magnetron sources.³ After achieving a base pressure of 1×10^{-7} torr, deposition of the single Co thin films was carried out at 1.2×10^{-2} torr in an environment of pure (99.99%) Ar. A thickness of 100 Å was deposited on each substrate at a rate of 4.0 Å/s. Following the initial surface and magnetic characterizations, both films were annealed four hours at 300 °C at a pressure of 4×10^{-8} Torr without a carrier gas. The annealing process was conducted by resistive heating of a tungsten (W) box covered to prevent contamination from gases desorbed off the chamber walls. The films were isolated from the box by ceramic discs placed underneath to prevent the diffusion of W into the Si.

The prepared films were characterized for roughness and magnetic properties. Surface topography was characterized by Atomic Force Microscopy in order to correlate roughness with magnetic properties for all films. Magnetic properties of the a- CN_x were characterized with a SQUID at NC A&T by Jamil Woods. A Vibrating Sample Magnetometer (VSM – Lake Shore Cryotronics, Inc) at NASA-Langley characterized films deposited on FL- CN_x buffers.

9.2 - Results on: a-CN_x

Figure 9.1 shows AFM scans of a 3-nm NiFe film on a-CN_x buffer layer, before (1a) and after (1b) annealing. The surface for both films is observed to be smooth. Whereas, it was difficult to resolve the grains of the NiFe films on the Ta or Cu, the larger grain pattern of the NiFe on the a-CN_x is obvious. As seen in Figure 9.1, the grain structure of the a-CN_x/NiFe does not appear to be significantly altered upon annealing.

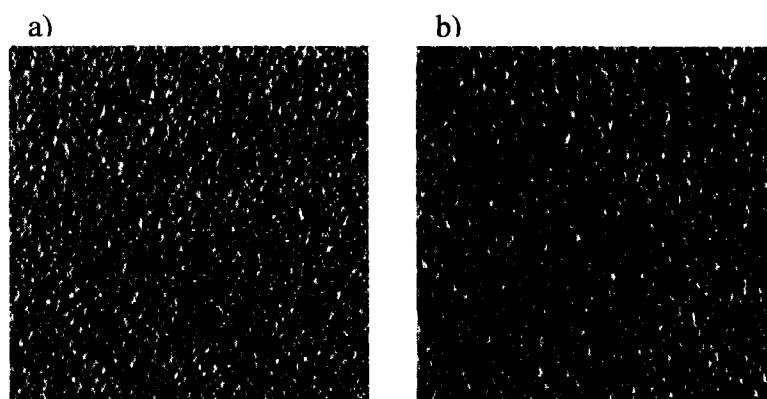


Figure 9.1: AFM scans in Tapping Mode, 2.5 μm x 2.5 μm a) AFM scan of unannealed a-CN_x/NiFe 30Å film. b) AFM scan of annealed a-CN_x/NiFe 30Å film. There are no changes in surface features.

Table 9.1 compares AFM roughness measurements taken prior to and post-annealing. It was found that, before annealing, the NiFe films deposited on the CN_x are only slightly rougher with larger peak heights than those on the Ta but less rough than those on the Cu buffer layers. After annealing, the roughness of the CN_x/NiFe actually decreases unlike the Cu and Ta buffer layers, where the roughness increases.

Substrate	Ra (nm)	σ_{rms} (nm)	Z (nm)
Unannealed			
Ta	1.9 ± 0.6	2.4 ± 0.6	21.7 ± 6.8
Cu	2.4 ± 1.4	2.9 ± 1.8	20.9 ± 15.2
a-CN _x	2.2 ± 0.5	2.8 ± 0.6	24.8 ± 4.4
Annealed			
Ta	4.4 ± 3.4	5.9 ± 4.2	104.7 ± 30.7
Cu	4.5 ± 2.7	3.8 ± 2.4	28.9 ± 17.8
a-CN _x	1.4 ± 0.06	1.8 ± 0.07	14.2 ± 1.7

Table 9.1: AFM measured average roughness, root-mean-square roughness, and peak height for unannealed and annealed films.

Figure 9.2 shows the magnetization of a 10 nm NiFe film on both a Ta and a-CN_x buffer layer. The coercivity for the Ta buffer layer is ~ 4 Oe and is thickness-independent within ± 1 Oe. As seen in Figure 9.2, annealing at 200 °C for 4 hours has little change on the hysteresis loop of the NiFe on the Ta buffer layers. Similar results were seen with Cu. In contrast, the NiFe film on the a-CN_x initially has a larger, thickness-dependent coercivity ($H_c = 36$ Oe for 10 nm of NiFe). Upon annealing, both the saturation magnetization and the coercivity of the NiFe film decrease dramatically ($H_c = 11$ Oe for 10 nm of NiFe).

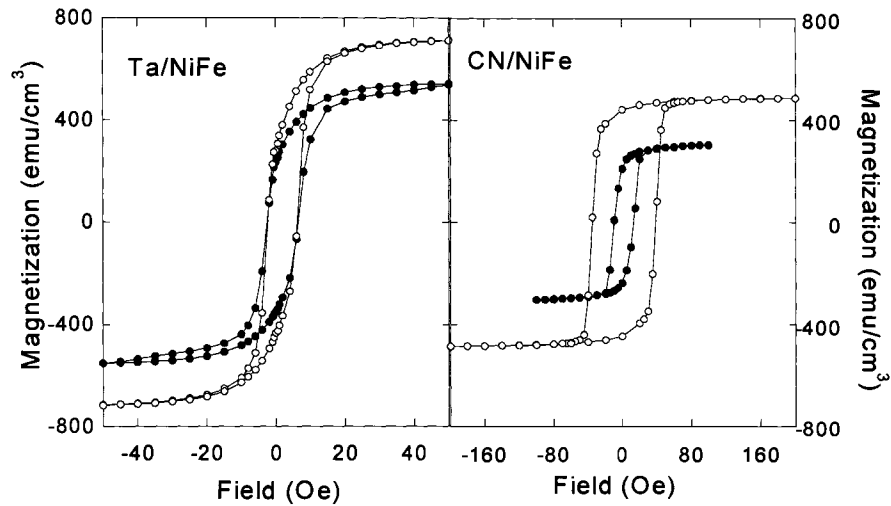


Figure 9.2: Comparison of Ta/NiFe annealed and unannealed films with a-CN_x/NiFe annealed and unannealed films. The unannealed films are represented by open circles, the annealed films by closed circles.

Figure 9.3 shows the saturation magnetization of the NiFe films on the various buffer layers as a function of NiFe film thickness. As the film thickness decreases, the magnetization decreases until it becomes negative. This negative value represents a layer of no magnetic contribution or a “dead” layer. From this data, the thickness of the dead layer can be estimated. The bulk magnetization is measured from the hysteresis curves for each sample. The total film and dead layer thicknesses are represented by t_{total} and t_{dead} , respectively.

$$M = M_{bulk} * (t_{total} - t_{dead}) \quad (9.1)$$

For the unannealed NiFe films on Ta and Cu, a dead layer of ~ 1 nm is estimated, which is slightly larger but comparable to that seen with other Ta/NiFe systems.⁷ Films with a NiFe thickness of 1 nm on Ta or Cu showed no evidence of hysteresis loops, but

only a diamagnetic response. Upon annealing at 200 °C for 4 hours, the dead layer does not increase for these buffer layers, indicating that significant interfacial mixing is not occurring. For the a-CN_x buffer layer, the unannealed films showed a larger “dead” layer of at least 2 nm. Upon annealing, it is clear that the total magnetization is decreasing, but we do not have enough data points to determine if this is due to an increase in the dead layer. For the NiFe films on a-CN_x, the unannealed and annealed films with thickness 2 nm and less were diamagnetic.

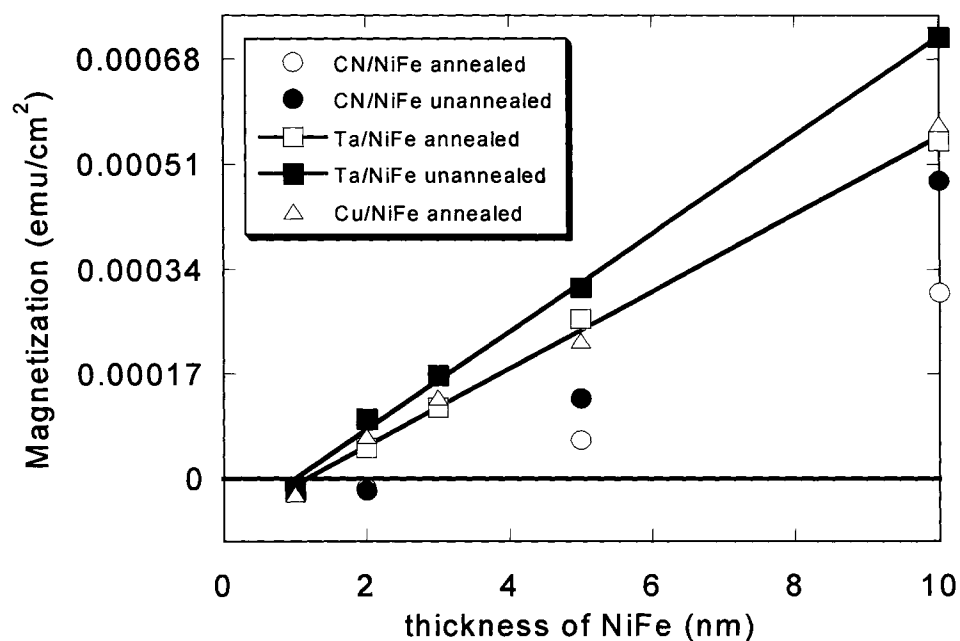


Figure 9.3: A comparison of film magnetization with film thickness. Magnetization decreased with NiFe thickness for both annealed and unannealed films. Magnetization is negative for a Cu/NiFe 10Å and Ta/NiFe 10Å and a-CN_x/NiFe 20Å suggesting a diamagnetic film for these thicknesses. The lines are fits to $M = M_{\text{bulk}} * (t - t_{\text{dead}})$.

The bulk saturation magnetization of the NiFe, calculated from linear fits in Figure 9.3, is highest on the unannealed Ta buffer layer ($M_{\text{bulk}} = 796 \text{ emu/cm}^3$) and decreases with annealing ($M_{\text{bulk}} = 628 \text{ emu/cm}^3$). The magnetization of the NiFe films on the a-CN_x can be estimated from a linear fit (not shown) if a 2 nm dead layer is assumed.

From this, we find $M_{\text{bulk}} = 593 \text{ emu/cm}^3$ for the unannealed a-CN_x/NiFe films and $M_{\text{bulk}} = 371 \text{ emu/cm}^3$ for the annealed films. With an accepted value of $M_{\text{bulk}} = 800 \text{ emu/cm}^3$ for bulk NiFe, the a-CN_x/NiFe film displays the lowest saturation value. Some of the decrease in magnetization can be attributed to oxidation of the surface of the NiFe, since the films were uncapped. However, it is obvious that the a-CN_x buffer layer is causing a further decrease in the NiFe magnetization that worsens upon annealing.

Preliminary x-ray diffraction measurements show a strong fcc <111> ordering for the 10 nm NiFe films on the Ta buffer layers. The 10 nm NiFe film on the a-CN_x however, showed no strong ordering peaks. TEM measurements indicate an amorphous structure for this film in contrast to the film on a Ta buffer. The electron diffraction analysis scan in Figure 9.4 exhibits a wide diffuse ring pattern. The width of the ring indicates either very small grain sizes or no grains at all. Very small grains would denote some crystallinity but no long range order.

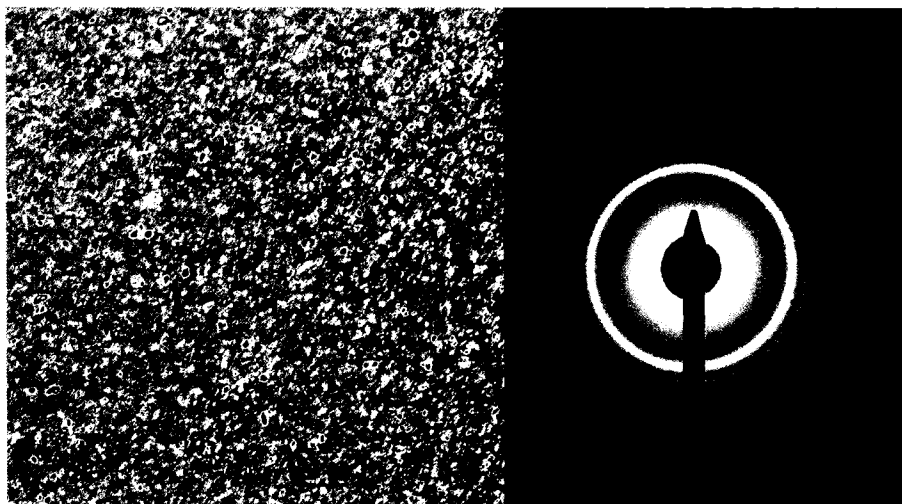


Figure 9.4: TEM scan of a-CN_x/NiFe 100Å shows NiFe islands (dark spots) growing on the a-CN matrix. Electron diffraction analysis of the film showed no strong ordering peaks and suggests an amorphous structure.

The decrease in magnetization and change in coercivity for the a-CN_x buffer layer are undesirable results for producing a stable magnetic multilayer structure. One possible cause is that the a-CN_x structure is not stable upon annealing; however, studies have shown that a-CN_x is stable at this annealing temperature since it is below the growth temperature.⁸ Results from AFM and TEM appear to confirm that no structure change is occurring. Instead, annealing the NiFe film could cause interdiffusion into the a-CN_x layer, forming a granular structure. In this case, an increase in coercivity may be expected. Another possibility is a combination of intermixing or the formation of nitrides or carbides at the interface. Studies of Ni/C and Fe/C multilayers (where C is amorphous carbon) have shown the formation of Ni₃C and Fe₃C at the interface (Ni₃C decomposes upon heating while Fe₃C is formed with heating).⁹ Recent NMR studies¹⁰ of a-CN_x have shown that these films are hydrophilic and that the water is released upon annealing at 150 °C. Given this, a reaction could be occurring in the NiFe film from the released water, which reduces the magnetization. Preliminary data on a-CN_x/NiFe films has shown that the magnetic properties improve and become more stable when the a-CN_x is grown at higher temperatures. This could be due to the higher temperature films having less nitrogen content and being less hydrophilic, or the interface bonding may be more stable.

9.3 - Results on FL-CN_x

For the purposes of the experiment, CN1 refers to the FL-CN_x grown in the 50-50% mixture while CN2 refers to that grown in 100% N₂ and refers to the entire film after deposition of the Co layer. AFM scans of CN1 and CN2, prior to and post-annealing, are shown in Figure 9.4. CN1 has numerous large granular features on its

surface before and after annealing at 300 °C. However, the feature size appears slightly smaller with an increase in the number and size of the clusters visible after annealing. No features are observed on CN2 either before or after annealing.

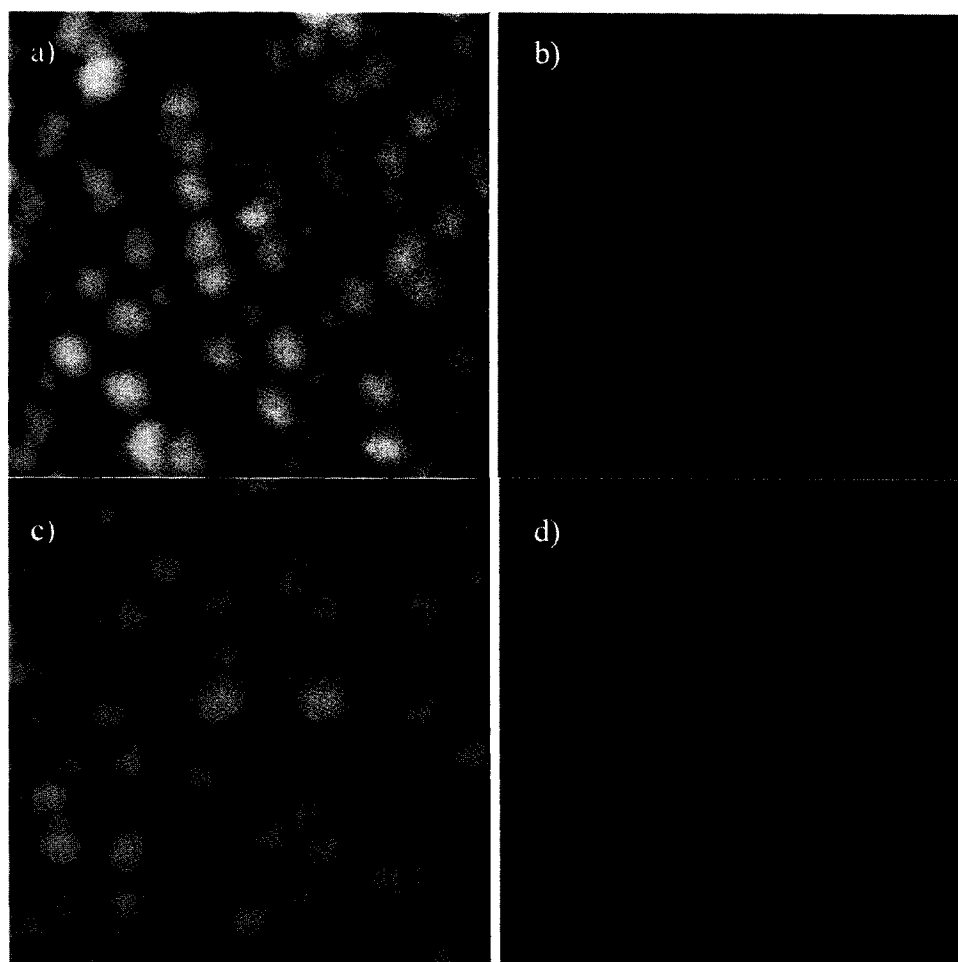


Figure 9.5: a) CN1 unannealed film. b) CN2 unannealed film. c) CN1 annealed film. d) CN2 annealed film. Co100 Å was deposited on CN buffers. AFM scan in Tapping Mode, 1 μm x 1 μm .

Table 9.2 displays the roughness and magnetic properties of both films as measured by AFM and VSM. Roughness values for CN1 are larger than those for CN2. More significantly, CN2 has a smoother topography exhibiting no large features. In

contrast, CN1 has features of significant size both in height and length. Post annealing, CN2 remains smooth showing no apparent grain or feature growth. While a small increase in σ_{rms} roughness, Ra roughness, and peak height (Z) are observed, the increase is slight and suggests that annealing of the film did not produce a significant structural change in the film. The small changes in features length and height further support this observation. In comparison, the coercivity and saturation magnetization display minor changes for both films. A decrease in the coercivity for CN1 corresponds to an increase in the film susceptibility, while the opposite is observed for CN2. There is a significant decrease in roughness for CN2.

Film	R _a (nm)	σ_{rms}	Z	L	h	H _c (Oe)	M _s (emu/cm ³)
Unannealed							
CN1	8.5 ± 2.9	10.9 ± 2.4	64.1 ± 1.4	130 ± 15	39.1 ± 6.7	48.9	1383 ± 8
CN2	5.9 ± 0.2	6.8 ± 0.2	31.5 ± 0.4	NA	NA	15.9	1367 ± 8
Annealed							
CN1	9.2 ± 1.7	11.6 ± 1.2	67.3 ± 8.7	110 ± 26	39.6 ± 11.6	45.7	1395 ± 8
CN2	0.8 ± 0.2	1.2 ± 0.3	17.8 ± 6.5	NA	NA	18.3	1350 ± 8

Table 9.2: Comparison of surface and magnetic properties for films prior to and post-annealing. Both films were deposited at 450 °C with a substrate bias of -40V. CN1 was grown in 50-50% N₂/Ar. CN2 was grown in 100 N₂.

The magnetic properties as compared to the roughness measurements are listed in Table 9.2 and illustrated in Figure 9.6 where open circles represent CN1 and closed circles represent CN2. The data in the table again shows a contrast between the two films on the FL-CN_x. CN1 slightly increases in saturation magnetization corresponding to a small decrease in coercivity post annealing, possibly indicating a minor increase in film magnetization. The data for CN2 displays the opposite relationship where an increase in

the coercivity coincides with a decrease in film magnetization. Further, CN2 has a saturation magnetization similar to that of CN1 but coercivity one third the value measured for CN1. Also, the shapes of the hystereses are markedly different between films but maintain their shape for the same film before and after annealing. The steeper slope for CN2 can be correlated to the smoothness of the film providing an easy switching layer contrasted by the much rougher film surface of CN1. Both films exhibit saturation magnetizations near the accepted value of 1422 emu/cm^3 for bulk Co.

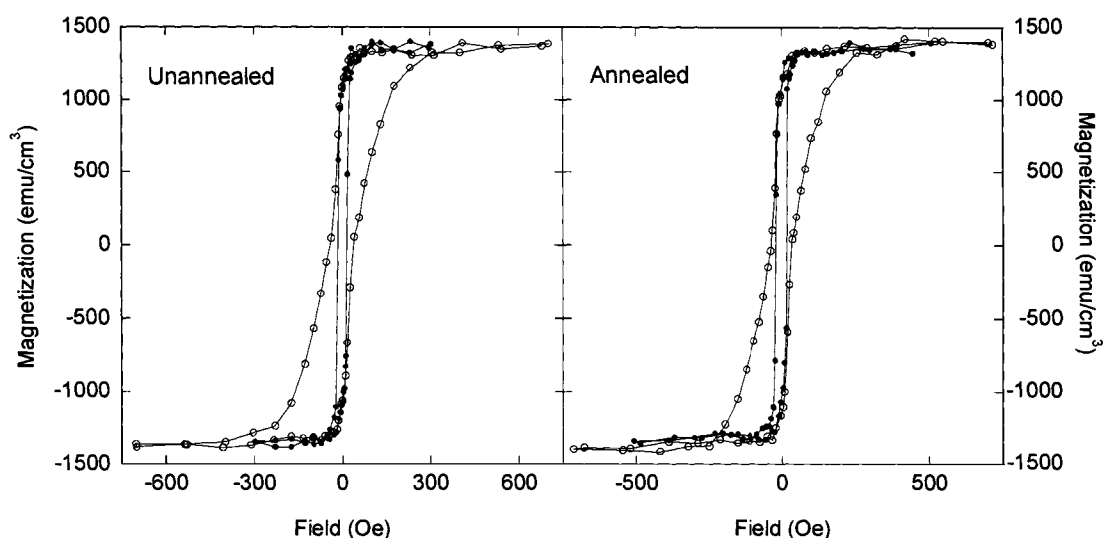


Figure 9.6: Comparison of normalized hysteresis loops for prior to and post annealing. No significant change in saturation magnetization or coercivity is observed. Open circles represent CN1. Closed circles represent CN2.

When comparing roughness measurements from both experiments as in Table 9.3, the films deposited onto FL-CN_x substrates have the largest roughness prior to annealing. Interestingly, CN2 measurements are the smoothest of all four films post-annealing and within one standard deviation, are equivalent to the measurements of the NiFe film on a-

CN_x. Though, CN1 increases in roughness with annealing, the change is significantly less than that of CN2, well within one standard deviation of the unannealed root-mean-square value. This further supports previous research on the effect that growth conditions of carbon-like materials have on film properties. Equally significant are the differing results of single films deposited on a-CN_x as compared to FL-CN_x. While films on a-CN_x substrates exhibited obvious degradations in magnetic properties with annealing, films on FL-CN_x displayed no significant changes.

Substrate	Ra (nm)	σ_{rms} (nm)	Z (nm)
Unannealed			
Ta	1.9 ± 0.6	2.4 ± 0.6	21.7 ± 6.8
Cu	2.4 ± 1.4	2.9 ± 1.8	20.9 ± 15.2
a-CN _x	2.2 ± 0.5	2.8 ± 0.6	24.8 ± 4.4
FL-CN1	8.5 ± 2.9	10.9 ± 2.4	64.1 ± 1.4
FL-CN2	5.9 ± 0.2	6.8 ± 0.2	31.5 ± 0.4
Annealed			
Ta	4.4 ± 3.4	5.9 ± 4.2	104.7 ± 30.7
Cu	4.5 ± 2.7	3.8 ± 2.4	28.9 ± 17.8
a-CN _x	1.4 ± 0.06	1.8 ± 0.07	14.2 ± 1.7
FL-CN1	9.2 ± 1.7	11.6 ± 1.2	67.3 ± 8.7
FL-CN2	0.8 ± 0.2	1.2 ± 0.3	17.8 ± 6.5

Table 9.3: A comparison of roughness measurement for films deposited on four different substrates. Films on both fullerene-like CN_x substrates exhibit the largest roughness prior to annealing. Post-annealing, CN1 has the roughest surface while CN2 has the smoothest surface of all four films.

9.4 - Conclusions

Surface roughness of films deposited on a-CN_x buffer layers is comparable to films on Ta or Cu buffers and is stable with annealing up to 200 °C. However, amorphous CN_x has a detrimental effect on the magnetization and coercivity of the NiFe films. This may be due to chemical reactions at the interface or interdiffusion creating

diamagnetic impurities or a thin diamagnetic layer. In contrast, Co films grown on hard CN_x showed no degradation in their magnetic properties up to an annealing temperature of 300 °C while the root-mean-square roughness, average roughness, and peak height remained comparable to roughness of films deposited onto traditional buffers. In fact, a Co film grown on FL- CN_x displayed a significant decrease in roughness while exhibiting no significant change in magnetic properties. It was expected that the FL- CN_x substrate would be stable in structure below its growth temperature. However, the substrate exposure to atmosphere does not appear to have had a noticeable effect on the magnetic film deposited on top. Atmospheric contaminants, such as water, should have been present at the FL-CN/Co interface. Contrary to the a-CN/NiFe films, annealing did not appear to drive these contaminants into the magnetic thin film due the cross-linking of the sp^2 orbitals, which actually benefits the FL- CN_x film.¹¹

In conclusion, this chapter explored the effect of a- CN_x and FL- CN_x buffers on magnetic thin films. While the smoothness of films grown on a- CN_x is comparable to films on traditional buffers, there is a detrimental effect on the magnetic properties of the films. In contrast, films on FL- CN_x have a larger roughness before annealing but are noticeably smoother post-annealing with no significant loss in magnetization or coercivity. Both carbon-like materials may useful in applications involving magnetic thin films.

9.5 - References

- ¹ L. Zhang, J. Wang, and H. Gong, *J. Phys.: Condens. Matter* **14**, 1697–1708 (2002).
- ² R. Prioli, S. I. Zanette, A. O. Caride, et al., *Dia. Rel. Mater.* **8**, 993 (1999).
- ³ J. Neidhardt, Z. Czigany, I. F. Brunell, et al., *J. Appl. Phys.* **93**, 3002 (2003).
- ⁴ A. Bousetta, M. Lu, and A. Bensaoula, *J. Vac. Sci. Tech. A* **13**, 1639 (1995).
- ⁵ E. Broitman, N. Hellgren, O. Wanstrand, et al., *Wear* **248**, 55 (2001).
- ⁶ A. Khurshudov, K. Kato, and S. Daisuke, *J. Vac. Sci. Tech. A* **14**, 2935 (1996).
- ⁷ Q. Leng, H. Han, M. Mao, et al., *J. Appl. Phys.* **87**, 6621 (2000).
- ⁸ J. N. Zhou, J. Du, A. F. Khapikov, et al., *J. Appl. Phys.* **87**, 5624 (2000).
- ⁹ R. Krishnan, H. O. Gupta, C. Sella, et al., *J. Magn. Magn. Mater.* **93**, 174 (1991).
- ¹⁰ W. J. Gammon, G. L. Hoatson, B. C. Holloway, et al., *Physical Review B-Condensed Matter* **68**, 195401 (2003).
- ¹¹ S. J. Bull, *Dia. Rel. Mater.* **4**, 827 (1995).

Chapter 10 — Summary

10.1 Summary

The primary focus of this research was to investigate the impact of large scale roughness on giant magnetoresistive (GMR) thin films. Secondary studies investigated the viability of depositing GMR on polymeric substrates and the inclusion of carbon nitride buffers in thin films. For all of these investigations, DC magnetron sputtering was the primary deposition process used to fabricate GMR and single thin films. For the controlled roughness study, current-perpendicular-to-the-plane (CPP) and current-in-plane (CIP) GMR thin films were deposited at Michigan State University using triode sputtering. Polymer nanospheres were used to introduce controlled roughness onto silicon oxide substrates¹. After removal of the polymer spheres, gold nanodots remained on the silicon surface. For the etched substrate study, current-in-plane films were deposited at William & Mary and the National Institute of Standards and Technology (NIST) on etched boroaluminasilicate glass. Glass substrates were prepared by etching with hydrofluoric (HF) acid for various lengths of time, again introducing roughness at the substrate but in a less controllable fashion. For the secondary studies, thin films were deposited on as-prepared polymeric substrates provided by the International Technology Center (ITC) and CN buffers were provided by Esteban Broitman and contributors in Sweden at Linkoping University.

From the data in chapters 7 and 8, a correlation between parallel state (minimum) film resistance and antiparallel state (maximum) film resistance has shown a linear relationship with a slope of ~ 1 . This indicates an increase in spin-independent scattering that may be connected to increases in roughness, which influence grains and grain boundaries. For the CIP films deposited at MSU, it was found that GMR decreased with minimum film resistivity. Substrate roughness appears to have a significant effect on spin-independent scattering but less so on spin-dependent scattering which is the dominant factor in determination of the GMR value of thin films. In both of these studies, the increase in antiparallel resistivity is matched by an increase in parallel resistivity. However, the long length scale appears not have a large detrimental on the GMR as theorized by Alicea and Hershfield.² The preliminary research conducted in chapter 8 has demonstrated the potential for further study of systems of controlled roughness using polymer nanospheres.

Results for chapter 6 demonstrate that GMR thin films can be deposited onto polymeric substrates and achieve GMR values comparable to those measured on silicon substrates. A comparison of GMR values for thin films deposited on polymers produced GMR equal to or slightly higher than the values measured on silicon. In chapter 9, the inclusion of CN thin films as buffer layers was explored. Significant decreases in magnetic response and coercivity were observed in amorphous-carbon nitride ($a\text{-CN}_x$) with annealing, while film root-mean-square roughness decreased. Data for fullerene-like carbon nitride showed small changes in magnetic response and coercivity and a similar decrease in root-mean-square roughness.

In summary, series of studies exploring the impact of roughness introduced through the substrate has demonstrated that long length scale roughness does not necessarily produce a large degradation of GMR behavior. For these systems, a decrease in GMR can be correlated with an increase in parallel state resistivity. Further, the antiparallel state resistivity increases linearly (slope ~ 1) with parallel state resistivity suggesting that spin-independent scattering is significantly affected by the increase in roughness while spin-dependent scattering is less effected. In addition, the potential of novel materials as substrates and buffers was illustrated in separate studies.

10.2 Future Work

There are several considerations for future work. This research has demonstrated some of the difficulty in introducing controlled uniform roughness over wafer-sized substrates. In regards to the nanodot deposition, researchers at Northwestern^{3, 4} have achieved a monolayer of coverage with good uniformity over smaller areas using a chemical stabilizer (hexadecanethiol) to prevent nanosphere aggregation. Using a drop-coat method, they are able to achieve monolayer coverage. Incorporation of a smaller substrate size with the chemical stabilizer used by the researchers at Northwestern could produce more favorable uniformity. Alternatively, depositing thin films directly onto a uniform multilayer of polymer nanospheres is another technique. Again, spin or drop-coating a small substrate $\sim 1\text{mm}^2$ may produce better results than attempting to coat an entire wafer. A third technique involving holographic gratings can also be explored. Pre-fabricated gratings with uniform spacing and height can be obtained from ThorLabs, for example. As substrates, these would provide uniform controllable roughness at the substrate.

Continued investigation of large scale roughness effects on GMR thin films would benefit from a more comprehensive characterization of the films. A cross-sectional analysis of the multilayer, such as that achieved with focused ion beam (FIB) characterization, would allow us to quantify the interfacial roughness directly and not simply from AFM surface scans. It would be possible to observe and measure the change in roughness from layer to layer. This may be possible with low angle x-ray diffraction (LAXRD) where the grazing angle would provide information about the film structure. Because it is a comprehensive measurement, depositing a series of films where the multilayer is deposited one layer at a time would allow for the quantification of the interfacial roughness.

10.3 References

- ¹ J. Wang, M. Zhu, Z. Xin, et al., in *International Vacuum Microelectronics Conference*, edited by M. Taki, Y. Gotoh and J. Ishikawa (Japan Soc. Promotion of Sci., Japan, 2003), p. 157.
- ² J. Alicea and S. Hershfield, *J. Magn. Magn. Mater.* **268**, 388 (2004).
- ³ A. J. Haes, J. Zhao, S. Zou, et al., *J Phys Chem B* **109**, 11158 (2005).
- ⁴ X. Zhang, E. M. Hicks, J. Zhao, et al., *Nano Lett* **0**, A (2005).

VITA

Shannon Moore Watson

Shannon Moore Watson was born in Columbia, South Carolina on June 11, 1977. She graduated from Brookland-Cayce High School in May 1995. Shannon Watson received her B.S. in Physics from Furman University in 1999.

Shannon Watson enrolled in the Physics graduate program at the College of William and Mary in 1999. She received her M.S. degree in Physics in 2001. In 2005, she successfully completed her graduate program and received a Ph.D. in Physics from the College of William and Mary.